



THE MINISTRY OF NATIONAL  
INFRASTRUCTURES  
GEOLOGICAL SURVEY OF ISRAEL

# **EVALUATION OF ROCKFALL HAZARD TO QIRYAT SHEMONA – POSSIBLE CORRELATION TO EARTHQUAKES**

**MOR KANARI**

This work was submitted as M.Sc. Thesis to the Department of Geophysics and Planetary Sciences, Tel Aviv University

The study was carried out under the supervision of:

Dr. Shmulik Marco, Department of Geophysics and Planetary Sciences, Tel Aviv University

Dr. Oded Katz, Geological Survey of Israel

Dr. Ram Weinberger, Geological Survey of Israel

# Abstract

---

**T**his study estimates rockfall hazard for the town of Qiryat-Shemona, situated within the Dead Sea Transform fault system, at the foot of the Ramim cliff. The 40-m-thick Ein-El-Assad Formation limestone outcrops provide the source material for rock blocks. Aerial photos from 1946–1951 show boulders of volumes of  $1 \text{ m}^3$  to  $150 \text{ m}^3$  situated within the now built town premises. This study examines: (a) what are the properties of the source rock and what is the triggering mechanism? (b) which are the feasible downhill trajectories of the blocks and where do blocks stop? (c) what is the rockfall hazard, and what may be recommended as a mitigation design for Qiryat-Shemona?

To answer these questions hundreds of rock-blocks were mapped on the slopes above Qiryat-Shemona using both field surveys and aerial photos and their volume and spatial distributions are analyzed; burial ages of soil samples from beneath large fallen blocks were determined by OSL; rockfall trajectories were simulated using a commercial program (CRSP v4). Hazard evaluation maps for Qiryat-Shemona were compiled from the results of rockfall simulations. Simulated analyses of block velocity and kinetic energy may be used as parameters for the design of mitigation of rockfall damage for Qiryat-Shemona. Rockfall hazard estimation is derived from: a. rockfall recurrence time based on OSL age determinations; b. block size probability derived from block volume distribution.

Results show that the block volume distribution follows an exponential function of the form  $ax^b$  with  $b$  value  $-1.17$ , in agreement with worldwide rockfall inventories. OSL dating of 8 soil samples demonstrate clustering around dates that coincide with known earthquakes, historic and prehistoric. It is concluded that earthquakes of large magnitudes ( $M_w \geq 7$ ) are the triggering mechanism of rockfalls, yet apparently the rock-mass has to be weakened by joints and fractures to facilitate rockfalls. Maps of maximal downhill block travel distances combined with slope morphological analysis were used to suggest possible trajectories of downhill historical rockfalls. The simulation program variables are calibrated and later used to simulate possible downhill rockfall block trajectories towards the town premises. Simulation results are used to compile the rockfall hazard maps. It is concluded that at the south-westernmost part of town, life and property are at rockfall hazard in particular areas. Rockfall recurrence interval and probability of block volumes determined from the volume distribution yield hazard evaluation for the area of Qiryat-Shemona. OSL age analysis of rockfall events (850 years recurrence time and assuming that the last rockfall triggered by the 1202 AD earthquake) lead to a 6.5% probability for the next rockfall to occur within the next 50 years, and a 57% probability within the next 475 years. Evaluated rockfall hazard probability for 50 years is 0.044–0.065, and for 475 years 0.385–

0.575, for block sizes or smaller than 10–125 m<sup>3</sup> respectively. Simulated results of block velocity and kinetic energy at specific impact locations on town yield block velocities of 10–15 m/s and kinetic energy of 18,000–45,000 kJ (98% confidence) for block volume of 125 m<sup>3</sup>. The recommendation for environmental friendly rockfall damage mitigation design is forestation of the slope. ❖

# Table of Contents

---

<b>Chapter 1 Introduction</b>	<b>1</b>
<b>1.1 Preface</b>	<b>1</b>
1.1.1 Goals and Research Questions	2
1.1.2 General Methods	3
<b>1.2 The Study Area</b>	<b>3</b>
1.2.1 Geological and Seismic Settings for Rockfall	3
1.2.1.1 Geographic Setting	3
1.2.1.2 Geological Setting	4
1.2.1.3 Naftali Mountains South to Margaliot Fault	6
1.2.1.4 Naftali Mountains North to Margaliot Fault	10
1.2.2 Earthquakes in the Study Area	12
1.2.3 Rockfalls in the Study Area	12
<b>1.3 Rockfall Related Literature Review</b>	<b>15</b>
1.3.1 Landslides	15
1.3.2 Rockfalls	16
1.3.3 Rockfall Initiation Mechanisms (Triggers)	17
1.3.4 Rockfall Path Profile	19
1.3.5 Rockfall Mechanics	20
1.3.5.1 Modes of Motion of Rocks	21
1.3.5.2 Freefall of Rocks	22
1.3.5.3 Bouncing and Rolling of Rocks	22
1.3.5.4 Stopping of Moving Rocks	22
1.3.6 Rockfall Volume Statistics	23
1.3.7 Comparison of Rockfall Models	26
1.3.7.1 Empirical Models	26
1.3.7.2 GIS-Based Models	26
1.3.7.3 Process-Based Models	27
1.3.8 Rockfall Simulation Programs	29
<b>Chapter 2 Methods</b>	<b>31</b>
<b>2.1 Block Data Acquisition</b>	<b>31</b>
2.1.1 Outline of the Mapping Area	31
2.1.2 Block Mapping	32
2.1.3 Block Volume Measurements	33
2.1.4 Diameter Estimation of Non-Mappable Blocks	33
<b>2.2 OSL Age Determination</b>	<b>35</b>

2.2.1	What is OSL Dating?.....	35
2.2.6	Field OSL Sample Collection.....	35
<b>2.3</b>	<b>Colorado Rockfall Simulation Program .....</b>	<b>36</b>
2.3.1	Rockfall Trajectory Analysis.....	36
2.3.2	Rockfall Behavior and CRSP Input Parameters .....	37
2.3.2.1	Slope Geometry .....	37
2.3.2.2	Slope Material Properties.....	38
2.3.2.3	Rock Geometry .....	39
2.3.2.4	Rock Material Properties.....	40
2.3.2.5	Starting Zone and Starting Velocity .....	40
2.3.2.6	Analysis Points.....	40
2.3.3	CRSP Program Assumptions .....	40
2.3.4	CRSP Algorithm for Rockfall Simulation .....	41
<b>Chapter 3</b>	<b>Results .....</b>	<b>43</b>
<b>3.1</b>	<b>Source, Blocks and Triggering Mechanism Properties .....</b>	<b>43</b>
3.1.1	Source Rock Joint Sets.....	43
3.1.2	Rockfall Origin Locations .....	45
3.1.3	Block Volume Probability Density Function (PDF) .....	46
3.1.4	Block Volume Distribution.....	47
3.1.5	Block Estimated Diameters .....	48
3.1.6	Triggering Mechanism of Rockfalls .....	51
3.1.6.1	Type of Failure .....	51
3.1.6.2	OSL Dating Results .....	51
<b>3.2</b>	<b>Rockfall Trajectories and Affected Area .....</b>	<b>53</b>
3.2.1	Data Collection for this Study .....	53
3.2.1.1	Feasible Trajectories of Falling Rock-Blocks .....	53
3.2.1.2	Slope Profiles.....	54
3.2.1.3	Rockfall Trajectories for Calibration .....	55
3.2.1.4	Surface Roughness (S) .....	55
3.2.2	CRSP Calibration for this Study .....	58
3.2.2.1	The Delta Max Distance Index.....	59
3.2.2.2	Preliminary Calibration Stage .....	60
3.2.2.3	Sensitivity Analysis to Initial Velocity .....	60
3.2.2.4	Rock Shape Sensitivity Analysis.....	61
3.2.2.5	Calibration Results.....	62
3.2.2.6	Calibration Conclusion.....	63
3.2.3	CRSP Simulation Travel Distances .....	64
3.2.4	Rockfall Hazard Area Map .....	64
3.2.4.1	Travel Distance vs. Block Volume .....	66

3.2.4.2	Hazard Map of the Distance Distribution of Block Travel.....	67
3.2.4.3	Stop Location and Slope Angle .....	71
3.2.4.4	Minimum Shadow Angle .....	72
<b>3.3</b>	<b>Rockfall Impact Hazard .....</b>	<b>72</b>
3.3.1	Velocity and Kinetic Energy Analysis .....	72
3.3.2	Town Border Impact Hazard Map .....	75
<b>Chapter 4 Discussion .....</b>		<b>77</b>
<b>4.1</b>	<b>Triggering Mechanism of Rockfalls .....</b>	<b>77</b>
4.1.1	Nature of the Rockfall Triggering Mechanism .....	77
4.1.2	OSL Results and Past Earthquakes .....	78
4.1.3	Clustering of OSL Ages .....	80
4.1.4	Statistical Validation of OSL Age Clustering .....	82
4.1.5	Rockfall Triggering by Earthquakes .....	84
4.1.6	Other Possible Triggering Mechanisms .....	86
4.1.7	Conclusion – Rockfall Triggering .....	86
4.1.8	Suggestion for Further Study .....	87
4.1.9	Seismic Topographic Amplification .....	88
4.1.10	Magnitude of Triggering Earthquakes .....	88
4.1.11	Rockfall Recurrence Interval .....	89
<b>4.2</b>	<b>Rockfall Trajectories and Affected Area .....</b>	<b>89</b>
4.2.1	Characteristics of Block Stop Locations .....	89
4.2.1.1	Implications for Rockfall Hazard Mitigation Design .....	91
4.2.1.2	Mis-fit of Small Blocks Simulated Travel Distances .....	91
<b>4.3</b>	<b>Hazard from Future Rockfalls .....</b>	<b>93</b>
4.3.1	Rockfall Hazard Area Map .....	93
4.3.2	Town Border Impact Hazard Map .....	94
4.3.3	Frequency of Stopping Blocks and Analysis Location Map .....	94
4.3.4	Rockfall Hazard Evaluation for Qiryat-Shemona .....	95
4.3.5	Rockfall Block Size Probability.....	95
4.3.6	Rockfall Recurrence Time Probability .....	95
4.3.7	Rockfall Hazard Evaluation for Given Time and Block Size .....	96
<b>4.4</b>	<b>Rockfall Impact Mitigation Design .....</b>	<b>97</b>
4.4.1	Possible Design for Mitigation of Rockfall Damage .....	97
4.4.2	Mitigation by Forests .....	97
<b>Chapter 5 Conclusion.....</b>		<b>99</b>
<b>References .....</b>		<b>101</b>
<b>Appendices.....</b>		<b>107</b>

# List of Figures

---

Figure 1-1 View from the Ramim Cliff east toward Qiryat-Shemona .....	2
Figure 1-2 Topographic setting of the study area, view northwest .....	4
Figure 1-3 Location map of Qiryat-Shemona .....	5
Figure 1-4 Geological map of the study area .....	6
Figure 1-5 Main faults of the Hula Valley, Mt Hermon and Southern Lebanon .....	8
Figure 1-6 The stratigraphy of the study area .....	9
Figure 1-7 Geological cross sections showing local and regional structures .....	11
Figure 1-8 Earthquake historical record of the study area .....	13
Figure 1-9 Israeli standard building code 413 PGA map .....	13
Figure 1-10 Aerial photo from 1951 – blocks at now built town premises .....	14
Figure 1-11 Total number of landslides and earthquake magnitude .....	16
Figure 1-12 A block and its originating cliff behind .....	17
Figure 1-13 Percentage of slope movements for the Yosemite Valley .....	18
Figure 1-14 Types of triggering mechanisms for slope movements .....	18
Figure 1-15 Distances of rockfalls from the epicenters of earthquakes .....	19
Figure 1-16 Schematic diagram of a typical rockfall path profile .....	20
Figure 1-17 Ritchie's theoretical considerations of rock trajectory .....	21
Figure 1-18 General modes of motion of rocks on slopes .....	22
Figure 1-19 Frequency density of Yosemite rockfalls and rockslides .....	24
Figure 1-20 Frequency density and volume of rockfall .....	25
Figure 1-21 Fahrböschung and minimum shadow angle of a talus slope .....	26
Figure 1-22 Actual vs. projected rockfall path .....	28
Figure 1-23 Rockfall paths resulting from 3D simulation (Apennines site) .....	30
Figure 2-1 Block mapping area .....	32
Figure 2-2 View east towards Qiryat-Shemona .....	32
Figure 2-3 Correlating maximal GIS dimension to measured block volume .....	34
Figure 2-4 Soil samples collection for OSL dating .....	36
Figure 2-5 Measuring surface roughness .....	38
Figure 2-6 Rock movement analysis .....	38
Figure 3-1 Location of scan lines at top of the Ein-El-Assad Formation .....	43
Figure 3-2 Schematic map of joint sets of the Ein-El-Assad Formation .....	44
Figure 3-3 Overview of the study area facing west .....	45
Figure 3-4 Location of traversing faults .....	46
Figure 3-5 Probability density function (PDF) of mapped blocks .....	47
Figure 3-6 Cumulative probability for given block diameter .....	48

Figure 3-7 Maximal GIS dimension of mapped field block volumes .....	49
Figure 3-8 Correlating maximal GIS dimension with block diameter .....	49
Figure 3-9 Estimated diameters of non-mappable blocks .....	50
Figure 3-10 Anti-slope dips at the base of the source cliff .....	51
Figure 3-11 All 25 rockfall trajectory simulation profiles used with CRSP .....	54
Figure 3-12 Measured surface roughness .....	55
Figure 3-13 Slope with abundant blocks .....	57
Figure 3-14 Slope with scarce blocks .....	57
Figure 3-15 Dependence of Surface roughness on the block diameter .....	58
Figure 3-16 CRSP Calibration profiles .....	59
Figure 3-17 Measuring observed maximal distance .....	60
Figure 3-18 Sensitivity analysis for initial velocity .....	61
Figure 3-19 Sensitivity analysis for rock shape input .....	62
Figure 3-20 Simulated vs. Observed maximal travel distances .....	63
Figure 3-21 Rockfall hazard map of Qiryat-Shemona .....	65
Figure 3-22 Maximal travel distances of simulated block diameters .....	66
Figure 3-23 Cumulative frequency of block stop distances – N section .....	69
Figure 3-24 Cumulative frequency of block stop distances – S section .....	70
Figure 3-25 Rockfall impact hazard at town border line .....	76
Figure 4-1 Grain supported blocks of various sizes at the talus .....	78
Figure 4-2 Talus blocks vary in size from small fragments to large blocks .....	78
Figure 4-3 OSL age results and candidate triggering earthquakes .....	80
Figure 4-4 Calculated paleo-rainfall amount during the last 7000 years .....	82
Figure 4-5 Clustering of OSL ages around historical earthquakes .....	83
Figure 4-6 Correlation of cave seismites with lacustrine seismites .....	85
Figure 4-7 Qiryat-Shemona OSL ages and suggested rockfall triggers .....	87
Figure 4-8 Slope angle at 50% and 100% of blocks stop .....	90
Figure 4-9 Observed blocks vs. CRSP simulated travel distances .....	93
Figure 4-10 Maximum energy dissipated by different tree species .....	98



# List of Tables

---

Table 1-1 Mean recurrence interval for DST earthquakes of $M > 6$ .....	12
Table 1-2 Types of landslides .....	15
Table 1-3 Characteristics of some computer rockfall simulation programs .....	29
Table 2-1 Suggested tangential coefficient input values .....	39
Table 2-2 Suggested normal coefficient input values .....	39
Table 3-1 Scan-line joint spacing .....	44
Table 3-2 Block volume (diameter) distribution at mapping area .....	47
Table 3-3 Lab results for OSL ages of Qiryat-Shemona samples .....	52
Table 3-4 Simulation block sizes .....	53
Table 3-5 Surface roughness field measurements for different rock radii.....	56
Table 3-6 Surface roughness for different block sizes .....	58
Table 3-7 Calibration results for CRSP input parameters .....	64
Table 3-8 Travel distance overshoot .....	67
Table 3-9 CRSP simulation travel distances .....	68
Table 3-10 CRSP simulation stop slope angles and swaths .....	71
Table 3-11 Shadow angle for talus profiles .....	72
Table 3-12 Calculated velocity and kinetic energy at stop line .....	73
Table 3-13 Predicted velocity and kinetic energy at town impact line .....	74
Table 3-14 Analysis point locations vs. stop line and impact line .....	74
Table 3-15 Predicted velocity and kinetic energy means .....	74
Table 4-1 Rockfall triggering candidate large scale historical earthquakes .....	79
Table 4-2 Rockfall triggering candidate events and evidence type .....	86
Table 4-3 Slope angle where 50% and 100% of blocks stop .....	90
Table 4-4 Rockfall block stop location characterization .....	91
Table 4-5 Cumulative probabilities of selected block diameters .....	95
Table 4-6 Rockfall hazard evaluation for 50 and 475 years .....	96

## Chapter 1

---

### Introduction

**R**ockfalls, down-slope movements of rock blocks, are typical in mountainous areas where they pose a hazard to humans and property all over the world (Crosta and Agliardi, 2004). Fallen rocks on the slopes range in size from cm-size to gigantic boulders hundreds of cubic meters in size. Rockfalls can be triggered by a variety of factors including earthquakes, rainfall, freeze and thaw cycles or progressive chemical weathering of rock and discontinuities (Crosta and Agliardi, 2004). During rockfall events, which are characterized by high energy and mobility, rock blocks move at velocities up to tens of meters per second. Because of potentially short spatial and temporal recurrence interval of rockfalls, they are extremely dangerous for people or property which encounter on their fall track (Crosta and Agliardi, 2004). Thus, rockfall hazard assessment should be considered for ensuring safety in mountainous areas.

#### 1.1 Preface

The town of Qiryat-Shemona (*Figure 1-1*) lies in the northern Hula Valley (*Figure 1-2*). This valley is part of a series of extensional basins that formed along the *Dead Sea Transform* active fault system (*Figure 1-3*). The town is located at the foot of the fault-controlled Naftali mountain ridge (Ramim cliff), which rises to its west. New quarters of the town are being planned and built below the ridge crawling up the slopes. These slopes are spotted with large, scattered, cliff-derived boulders, which have apparently traveled there by rockfall and landslide mechanisms. These could have been the results of either one or two processes: one is slow protracted weathering of the cliff and the other is catastrophic, such as earthquakes or extreme climatic events like heavy rainstorms or freeze-thaw cycles. Earthquakes are common in the study area, situated on the western fault branches of the Hula Valley (Heimann and Ron, 1987). The natural surroundings of the western part of Qiryat-Shemona are prone to rockfall hazard.



**Figure 1-1.** View from the Ramim Cliff east toward Qiryat-Shemona. The town lies at the foot of the cliff, on the western border fault branch of the Hula Valley (at the background).

### 1.1.1 Goals and Research Questions

This study aims to evaluate rockfall hazard for Qiryat-Shemona by identifying the rockfall triggering conditions, modeling the down-slope rockfall trajectories and estimating the expected kinetic energy of the blocks when reaching town borders. This site serves an example to an evaluation of rockfall hazard to a settlement lying at the foot of a cliff.

Derived from above are the following required actions:

- Rockfall hazard evaluation for the Ramim cliff slopes.
- Rockfall hazard evaluation for Qiryat-Shemona.
- Suggested design measures for mitigation of rockfall damage to Qiryat-Shemona.

These tasks are addressed by answering the following questions, categorized by rockfall aspects.

#### Source and Triggering Mechanism

- a. What are the geological and seismic settings of the study area?
- b. What are the possible triggers for the rockfalls in the Naftali Mountains?
- c. Is there a possible correlation of these rockfalls to earthquakes?
- d. When have these rockfalls occurred?
- e. What is the recurrence interval of rockfalls?

#### Rockfall Trajectories

- f. What are the feasible trajectories of falling rock blocks down the slope?
- g. Where do falling rock-blocks stop? Can it be characterized?

**Rockfall Hazard**

- h. What is the area subject to probable hazard from future rockfalls on the slopes under the Ramim cliff?
- i. Where are town premises subject to rockfall impact?
- j. What may be the rock block size and its possible velocity at the impact point of buildings or infrastructure of Qiryat-Shemona?
- k. What is the hazard to specific properties of Qiryat-Shemona (buildings, roads etc.)?

**Rockfall Impact Mitigation Design**

- l. What are the possible mitigation design measures for rockfall damage?
- m. What might be the recommended mitigation design for Qiryat-Shemona?

**1.1.2 General Methods**

To answer these questions hundreds of rock-blocks were mapped on the slopes above Qiryat-Shemona using both field surveys and aerial photos and their volume and spatial distributions were analyzed; burial ages of soil samples from beneath large fallen blocks were determined by OSL (*Optically Stimulated Luminescence*) method in order to date the time of the rockfalls; rockfall trajectories were simulated using a commercial rockfall simulation program (CRSP v4). Hazard evaluation maps for Qiryat-Shemona were compiled from the rockfall simulations results. Simulated analyses of block velocity and kinetic energy along the slope suggest the design for mitigation of rockfall damage for Qiryat-Shemona. Rockfall hazard was derived from: a. rockfall recurrence time (from OSL age results); b. block size probability (from block volume statistics).

**1.2 The Study Area****1.2.1 Geological and Seismic Settings for Rockfall**

Prior to any discussion of the geological and seismic settings converged at the study area, which may result in rockfall, one simple fact must be faced – rockfalls from the cliff of Ein-El-Assad Formation *have* occurred in the past. The physical conditions which had matured to result in these rockfalls have been found in this work to be as follows.

**1.2.1.1 Geographic Setting**

The town of Qiryat-Shemona is situated at the base of the Naftali mountain ridge, on the northern part of Israel (*Figure 1-3*). While the town lies at the north-western border of the Hula Valley, the slope rises west to 800 m above the valley and 880 m above sea-level (Sneh and Weinberger, 2003). The outcrops of Ein-El-Assad Formation, the source rocks for rockfall boulders, are located about 350 m above town. These outcrops create a steep 40 m cliff and a

debris slope below it, which reaches town border (**Figure 1-2**). This slope is covered with hundreds of scattered boulders that appear to have been detached from the cliff that rises above the town and driven there by landslide and/or rockfall mechanisms. The boulders vary in size from tens of cubic centimeters to tens of cubic meters. Here data collection has been performed in order to evaluate the rockfall hazard for Qiryat-Shemona. Coordinates of the corners of the study area are (Israel's New Grid): SW corner 25200/78600; NE corner 25380/79050.



**Figure 1-2.** Topographic setting of the study area, view northwest. Top of the Ein-El-Assad Formation is marked with a red hazard triangle.

### 1.2.1.2 Geological Setting

The geological background described hereafter is based mostly on the Metulla quadrangle 1:50,000 scale geological map (Sneh and Weinberger, 2003) partly presented in **Figure 1-4**. Qiryat-Shemona resides where the western-border fault of the Hula Valley, a pull apart basin formed along the Dead Sea Transform since early Pliocene (Freund et al., 1970; Garfunkel, 1981), branches into a few faults towards the north (**Figure 1-5**). The main fault among the latter is the Qiryat-Shemona fault, which continues northward where it is called the Yammuneh fault (trending north-northeast). The Yammuneh crosses Lebanon and Syria and continues up to Turkey (Kafri, 1991; Sneh and Weinberger, 2003). Another branch, the Roum fault trends north-northwest in Lebanon. The Hula eastern border fault runs along the eastern margins of the Hula Valley until it reaches Mt. Hermon, where it curves northeastward along the Si'on stream towards Rashiya. Regional stratigraphy (**Figure 1-6**) is of mid-Jurassic to Holocene, missing outcrops of late Eocene to mid-Miocene (Sneh and Weinberger, 2003).

The Metulla quadrangle covers an area divided into 7 geological blocks (Sneh and Weinberger, 2003): 1. Naftali Mountains south to Margaliot fault; 2. Naftali Mountains north to Margaliot



fault to Qiryat-Shemona fault and further to the Yammuneh fault; 3. from Qiryat-Shemona to the western foot of Mt. Hermon; 4. western Hermon to Si'on fault; 5. eastern Hermon; 6. the Golan Heights; 7. the Hula Valley. Detailed hereafter are the relevant Naftali Mountains from each side of the Margaliot fault (blocks 1 and 2 above).

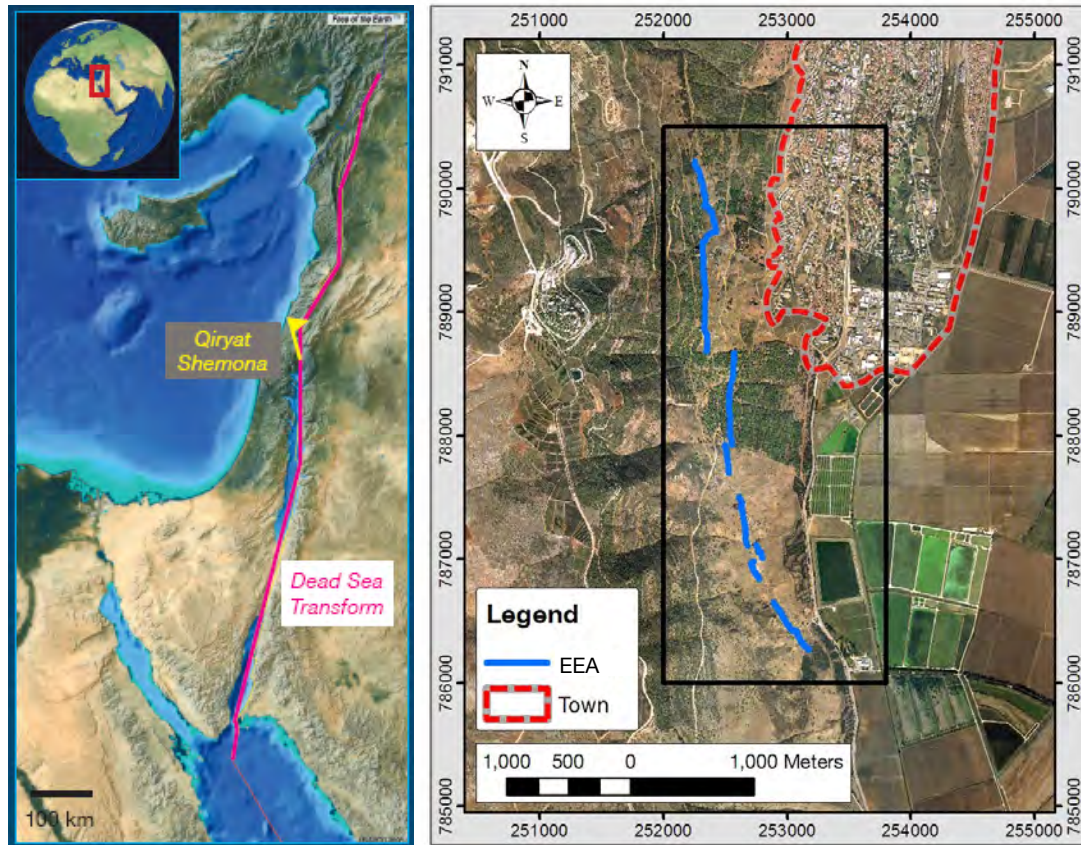


**Figure 1-3.** Left: Location map of Qiryat-Shemona. Right: Map of the study area in black rectangle. Ein-El-Assad Formation (EEA) is marked by blue line; town area in red dashed line.

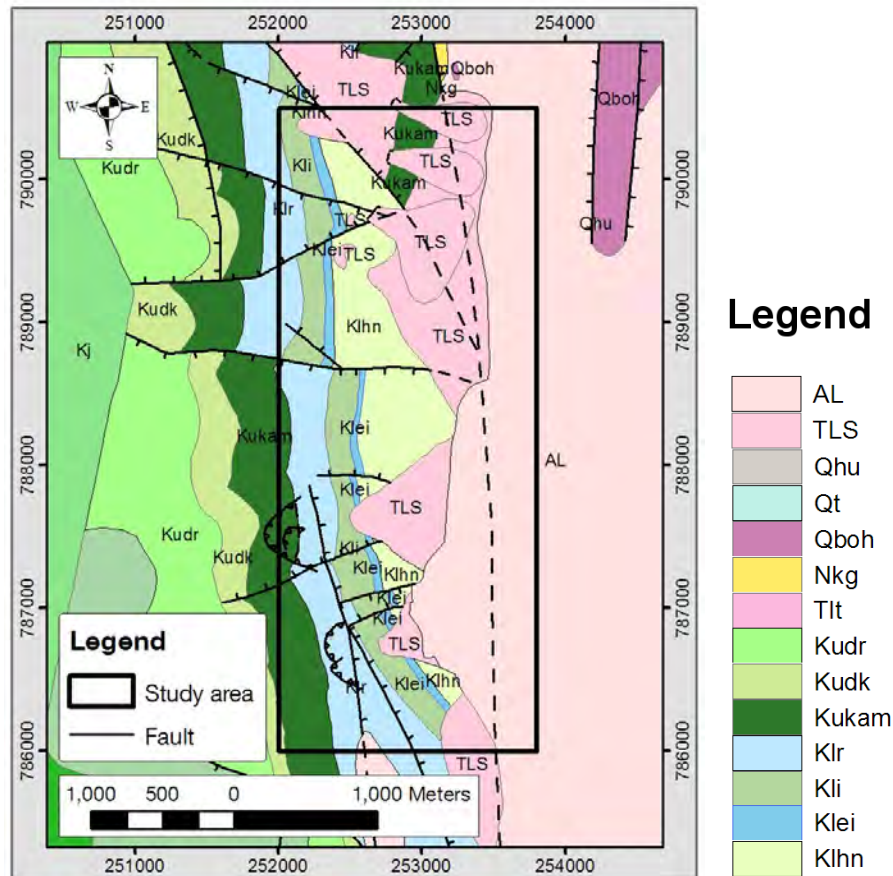


**Figure 1-4.** Geological map of the study area. Study area is marked by a black rectangle; faults are marked by solid black lines; concealed faults in dashed lines. Klei – Ein-El-Assad Formation which is the source of the studied blocks; TLS – rockfall debris and talus. Digital map data from Geological Survey of Israel (Sneh and Weinberger, 2003).

### 1.2.1.3 Naftali Mountains South to Margaliot Fault

#### Stratigraphy

The slope rising west 800 m above Qiryat-Shemona outcrops these formations (bottom to top): Hatira, Nebi Sa'id, Ein-El-Assad, Hidra, Rama, Kamon and Deir Hanna. Outcrops of the following formations are found further south: Sakhnin, Bina, Menuha, Mishash, Ghareb and Taqiye, see **Figure 1-6**.

The Hatira and Nebi Sa'id formations comprise the studied slope, and their boundary isn't conspicuous so they are mapped as a single unit with a 78 m thickness. The mostly sandstone Hatira Fm. outcrops at its top 50 m, covered by the alternating sandstone, limestone and marl of the Nebi Sa'id Fm. At the slope base, outcrops are fully covered by recent deposits. The Ein-El-Assad Fm. is mostly a 42 m thick biomicrite limestone. It outcrops on large parts of southern Lebanon, where it is dubbed *Muraille de Blanche*. The Ein-El-Assad Fm. is conformably overlain by the Hidra Fm. which due to a change in coastline location is comprised of alternating biomicrite, clay-limestone, sandstone and marl (Sneh and Weinberger, 2002). The Hidra Fm. forms the upper boundary of the study area.

Alluvial deposits originating from slope movements were described in the vicinity of Qiryat-Shemona (Sneh and Weinberger, 2002) and at the foot of the Naftali Mountains southbound toward the Kadesh stream. These are apparently recent, inferring from morphological phase of scarps. Some landslide taluses were spotted south to Qiryat-Shemona.

### **Tectonic Structure**

The Naftali Mountains are bound in the east by the Hula western border fault. The Cretaceous units of the riding eastern-block dip slightly west towards the synclinal axis of Wadi Dubah. The mountain-ridge is traversed by faults trending east-west, with only several tens of meters throw. Two parallel faults trending north-south 500 and 1000 m west to Hula Valley form two morphological ledges elevated 70 and 300 m respectively above the valley floor.

Recent tectonics is inferred from the locations of faults and fresh scarps, and rock and debris flows. Shtober-Zisu (2006) concluded that the slope is stable for at least 1.1 Ma. Hence, since that time, only small-scale tectonic movements (several meters) have occurred on the border faults, and the basin drainage level is similar to the current. She suggested that since the end of the early Pleistocene, stream slopes have maintained their morphology and most activity included deposition and removal of sediments along slope.



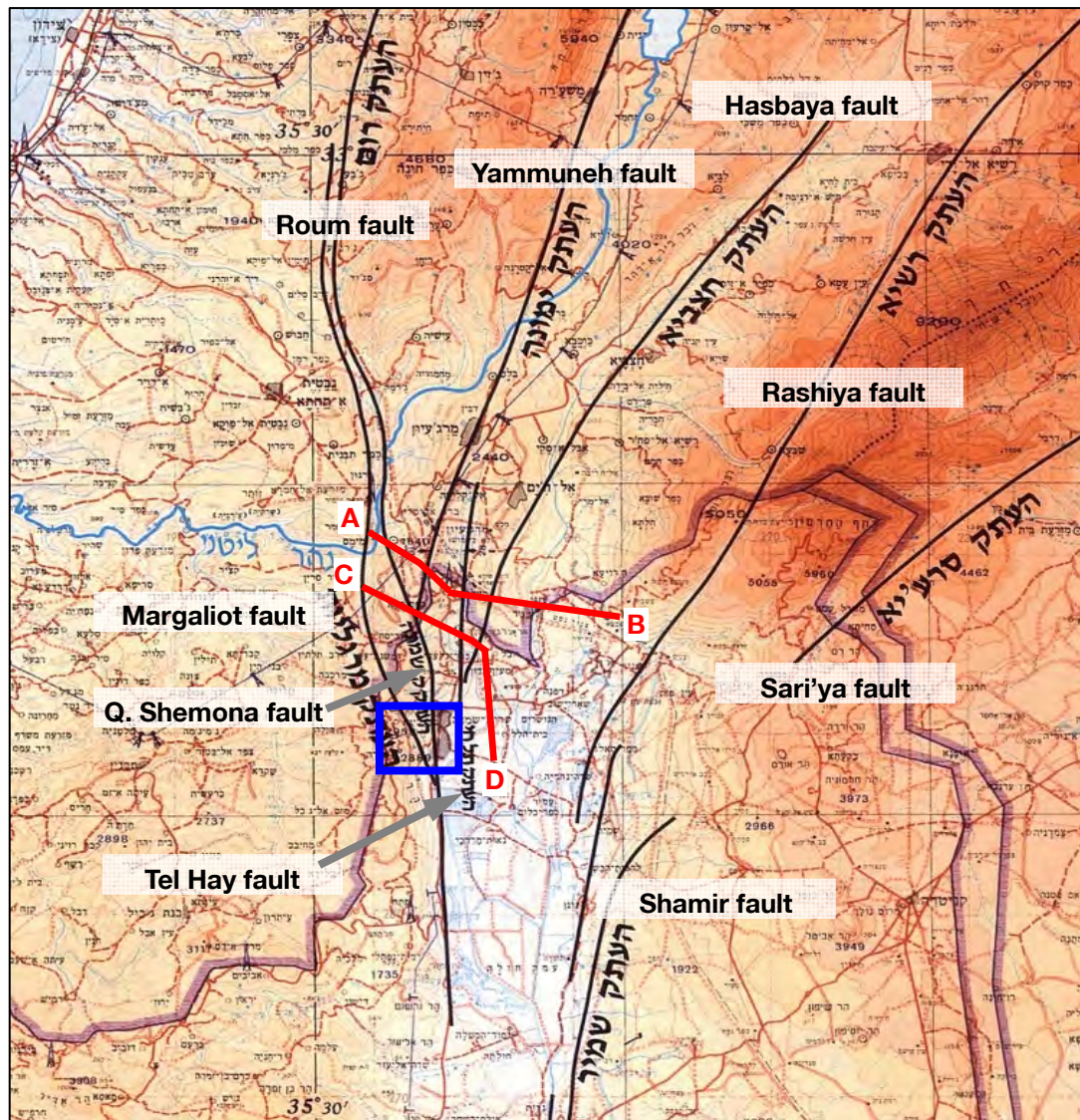


**Figure 1-5.** Main faults of the Hula Valley, Mt Hermon and Southern Lebanon. Red lines outline the geological cross sections A-B and C-D (see text for details); blue rectangle outlines the study area; gray arrows refer to locations of specified faults; map modified after Sneh and Weinberger (2003).

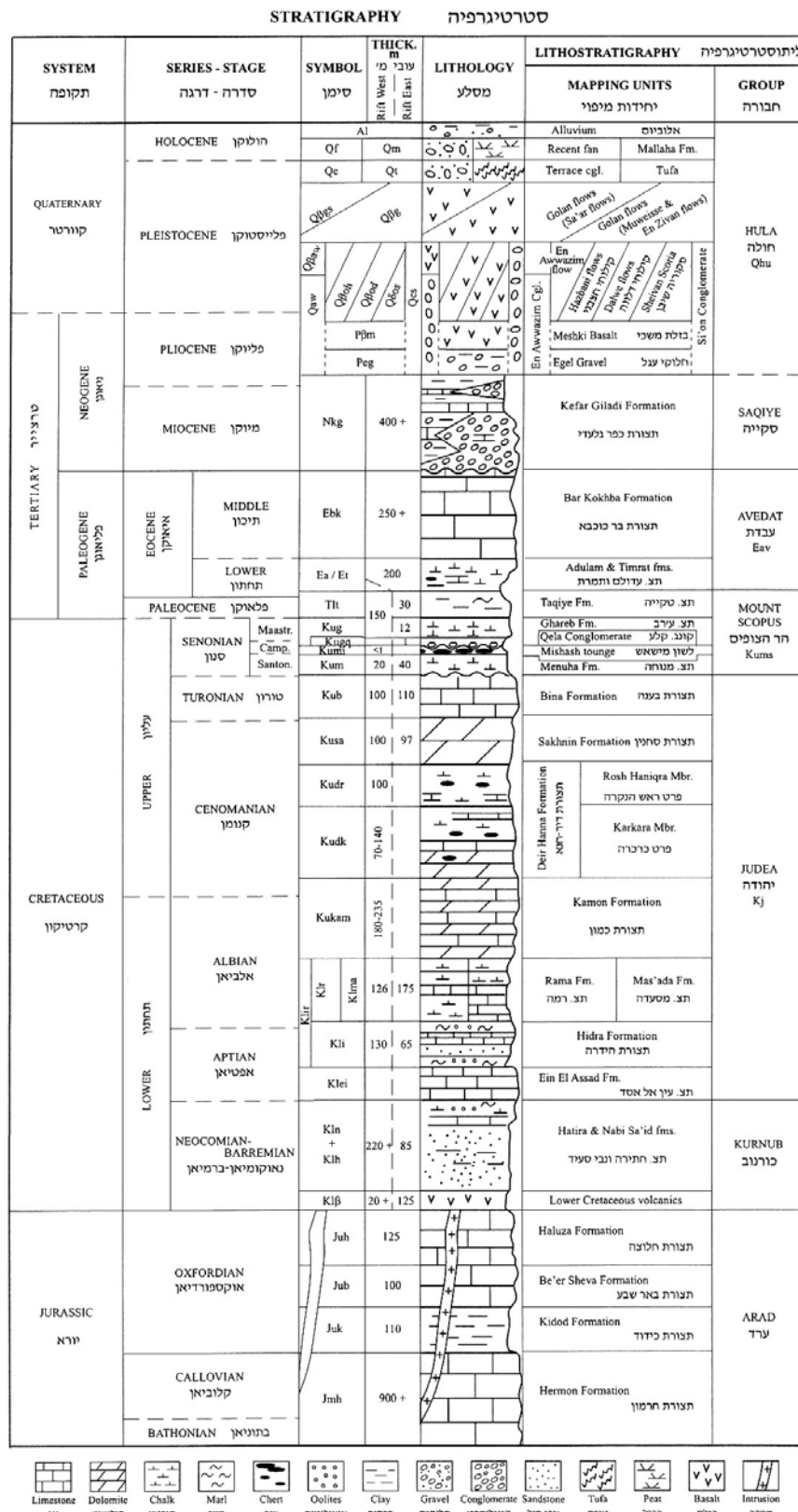


Figure 1-6. The stratigraphy of the study area (after Sneh and Weinberger, 2003).

#### 1.2.1.4 Naftali Mountains North to Margaliot Fault

##### Stratigraphy

The Kurnub and early Judea groups are detailed above. Sneh and Weinberger (2003) add a few notes (see **Figure 1-6**): *Rama*, *Kamon* and *Deir Hana* formations are similar on both sides of the fault. Several other units outcrop here: *Avedat group* (*Timrat* and *Bar Kokhva* formations), *Kefar Giladi formation*, *Egel Gravel*, *Hula group* (recent rock units, mainly Quaternary, mostly covered by alluvium), *Tufa unit* and *Si'on Conglomerate*.

##### Tectonic Structure

The main faults dictating the tectonic structure of the region are: a. Qiryat-Shemona fault branching towards the north to Yammuneh and Roum faults; b. Margaliot fault; c. Tel Hay fault; d. Shehumit fault and its unclear continuation as Hasbaya fault. The eastern border fault of the Hula valley continues north at Mt. Hermon as Si'on fault (Rashiya fault in Lebanon). These divide the northern margin of the Hula Valley into several tectonic structures (**Figure 1-5**):

1. Misgav-Am – Litani block: between Margaliot fault and Qiryat-Shemona fault (cont. to Roum fault).
2. Jabel Niha (Lebanon) block: between Roum and Yammuneh faults.
3. Metulla block: between Qiryat-Shemona fault (cont. to Yammuneh) and Tel Hay fault.
4. El Hiyam block: between Tel Hay and Hasbaya faults.
5. Western Hermon block: between Hasbaya and Rashiya faults

Rock bedding of the first 3 blocks above were found intensively folded and faulted by a number of authors (Glikson, 1966; Kafri, 1989; Picard, 1952; Ron et al., 1997; Weinberger and Sneh, 2004).

Two geological cross sections perpendicular to the above structures were compiled by Sneh and Weinberger (2003). They are outlined in **Figure 1-5** (A-B and C-D) and detailed in **Figure 1-7**.

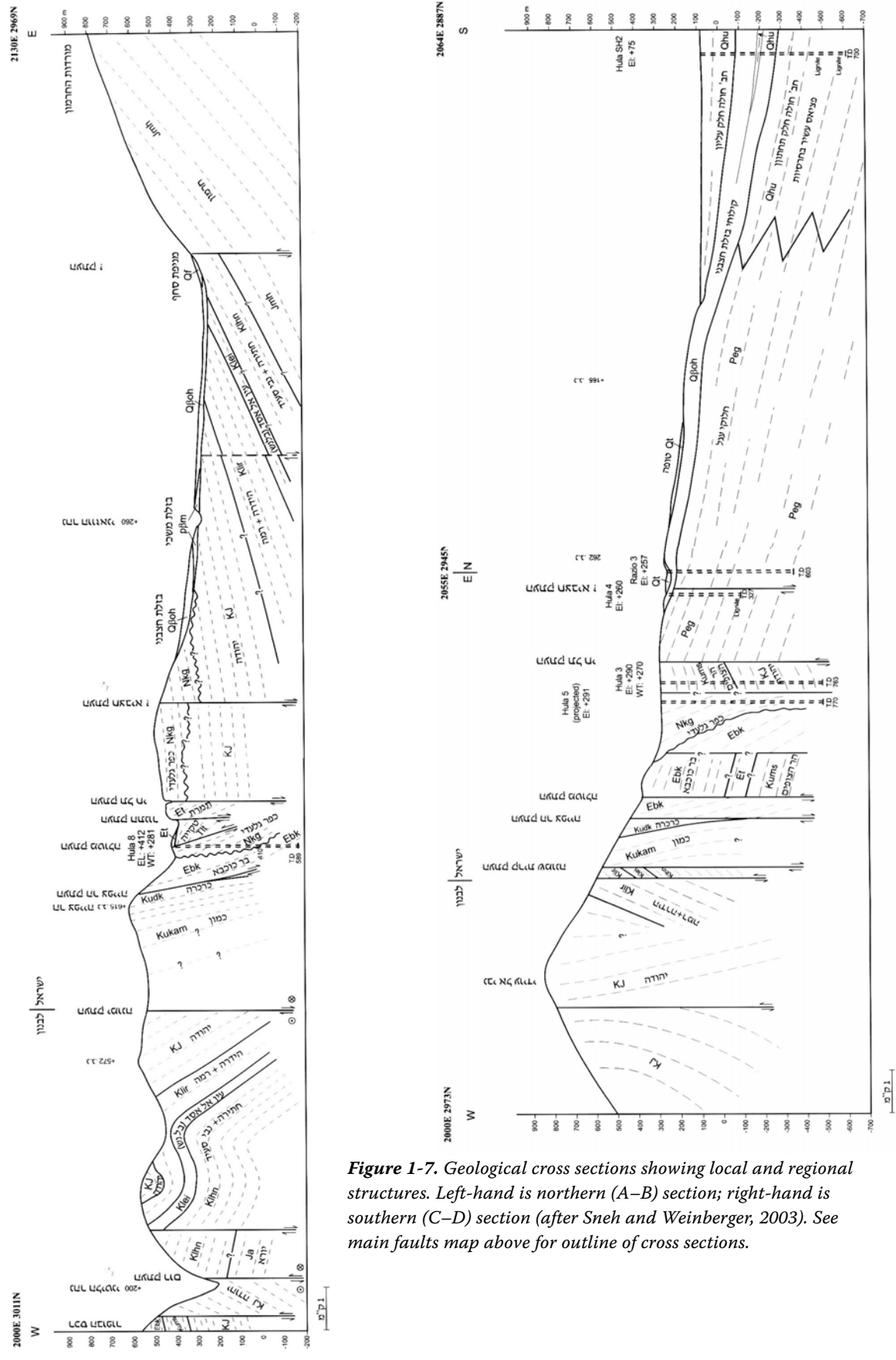


**Figure 1-7.** Geological cross sections showing local and regional structures. Left-hand is northern (A–B) section; right-hand is southern (C–D) section (after Sneh and Weinberger, 2003). See main faults map above for outline of cross sections.

### 1.2.2 Earthquakes in the Study Area

Situated along the Dead Sea Transform active fault system, the study area is subject to earthquakes. More than a hundred earthquakes with  $3.5 < M_L < 6$  (local magnitude) were recorded in the vicinity of the study area in the past 100 years (**Figure 1-8**). According to Israeli standard building code 413 peak ground acceleration (PGA) on rock, which has 10% probability to be exceeded at least once during 50 years (average recurrence interval of 475 years), for the Qiryat-Shemona Mountains is 0.26 g (Geophysical Institute of Israel; <http://www.gii.co.il>). The PGA map is detailed in **Figure 1-9**. Seismic topographic amplification effect at the Ramim cliff is discussed in **section 4.1.9**.

#### Earthquake Recurrence Interval

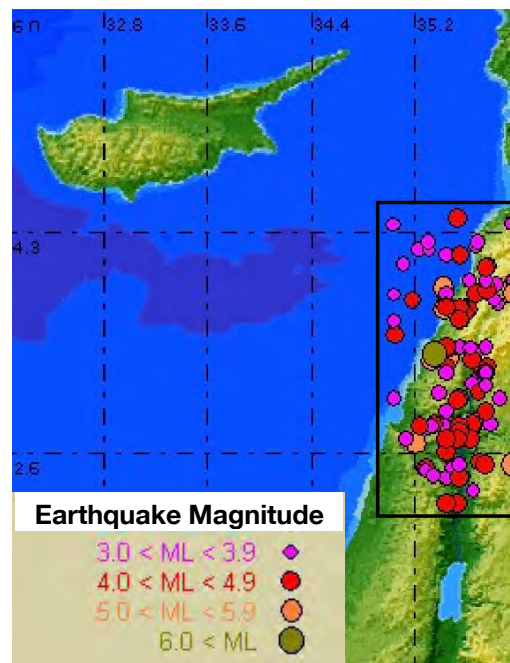
The recurrence interval of large ( $M > 6$ ) earthquakes along the DST was analyzed by Begin (2005) as detailed in **Table 1-1**. These intervals are referred to later when discussing recurrence intervals of rockfall for hazard evaluation.

TABLE 1-1 Mean Recurrence Interval for DST Earthquakes of $M > 6$ (after Begin, 2005)		
Mw	M <sub>L</sub>	Years
6.2	6.2	400
6.5	6.5	800
7.0	6.8	3,000
7.5	7.0	10,000

### 1.2.3 Rockfalls in the Study Area

There is no historical record of rockfalls in the study area. However, rockfalls from the Ein-El-Assad Formation are observed in the field, while aerial photos dating 1946 and 1951 show rock blocks of volumes  $1 \text{ m}^3$  to  $125 \text{ m}^3$  situated within the now built town premises (**Figure 1-10**). Rockfall talus is located on the slope west of Qiryat-Shemona, featuring abundant blocks that have traveled further beyond the talus margin. These observations are the basis for the evaluation of the rockfall hazard for Qiryat-Shemona.





**Figure 1-8.** Earthquake historical record of the study area. 115 events of local magnitude ( $M_L$ ) > 3.5 for the years 1905-2008 occurred within in the area outlined in black. Data and figure from the Geophysical Institute of Israel (<http://www.gii.co.il>).

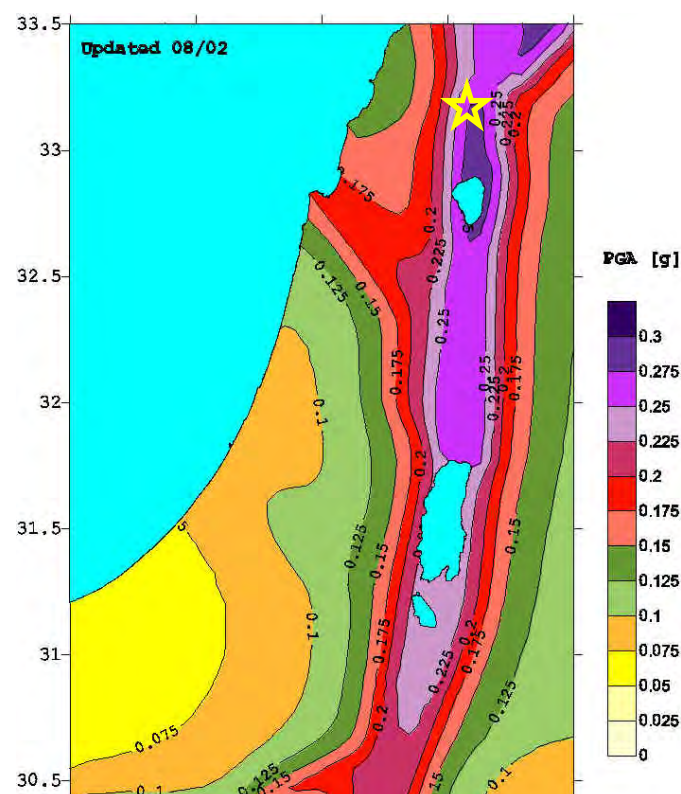


**Figure 1-9.** Israeli standard building code 413 PGA map (Peak Ground Acceleration) for rock. Qiryat-Shemona is marked in a yellow star (Geophysical Institute of Israel; <http://www.gii.co.il>).



**Figure 1-10.** Aerial photo from 1951 showing blocks where built town premises of Qiryat-Shemona are located today. Photo area marked with black rectangle in inset map; blocks located on aerial photo using a stereoscope marked in blue.

## 1.3 Rockfall Related Literature Review

### 1.3.1 Landslides

Rockfall is one sub-type of the phenomena related to as *landslides*. The term '*landslide*' includes a wide variety of earth materials movements, such as slumps, soil slips, mud flows, debris flows, rockfalls etc. (Jibson, 1996).

Landslides classification is frequently based on the type of material involved (soil or rock) and on the type of movement: falls, topples, slides, slumps, flows, or spreads (Jibson, 1996). Keefer (2002) studied 40 worldwide historical landslides induced by earthquakes and found rockfalls to be the most abundant of all landslide types, along with disrupted soil slides and rockslides (These landslides comprised about 80% of all reported earthquake induced landslides: Rockfalls – 35%; disrupted soil slides – 26%; rockslides – 20% (Keefer, 1984; Keefer, 2002). Keefer (2002) also showed that landslides were responsible for significant numbers and proportions of casualties and levels of economic damage in various earthquakes. At least 90% of the deaths in the 40 earthquakes studied were caused by rockfalls, rock avalanches and rapid soil flows. Keefer suggests that the high hazard from rockfalls derives from both their transport of rock material at high velocities and of their abundance.

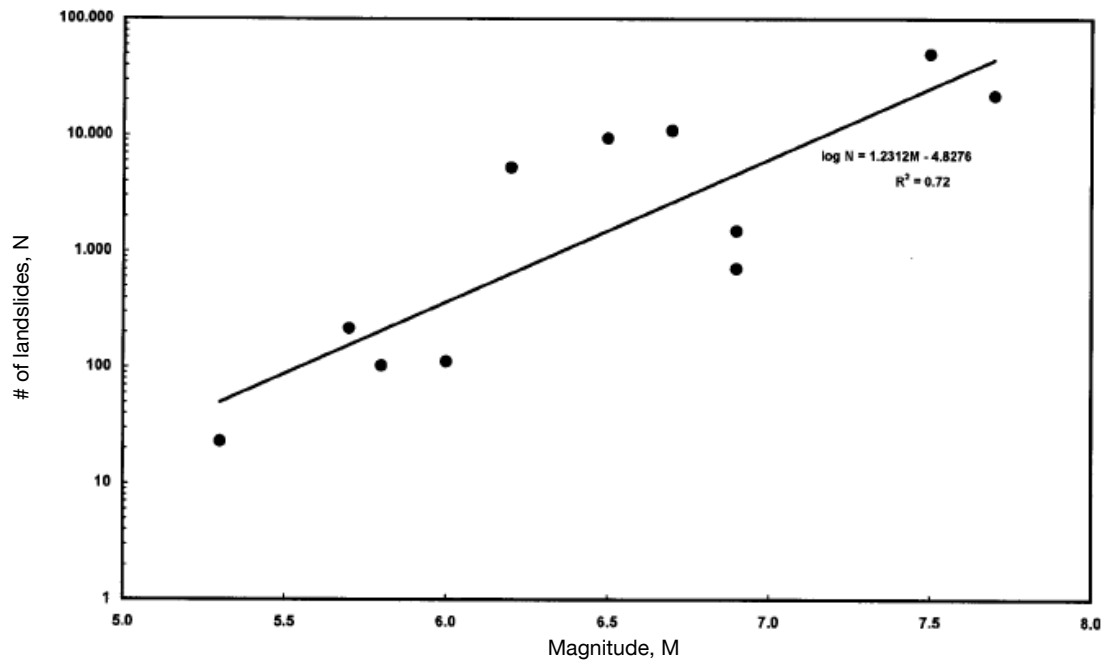
Varnes (1978) categorized landslides as detailed below in **Table 1-2**.

TABLE 1-2 <b>Types of Landslides (revised after Varnes, 1978)</b>				
TYPE OF MOVEMENT		TYPE OF MATERIAL		
		BEDROCK	ENGINEERING SOILS	
			Predominantly coarse	Predominantly fine
FALLS		Rock fall	Debris fall	Earth fall
TOPPLES		Rock topple	Debris topple	Earth topple
SLIDES	ROTATIONAL	Rock slide	Debris slide	Earth slide
	TRANSLATIONAL			
LATERAL SPREADS		Rock spread	Debris spread	Earth spread
FLOWS		Rock flow	Debris flow	Earth flow
		(deep creep)	(soil creep)	
COMPLEX		Combination of two or more principal types of movement		

Regarding the landslide trigger, summarizing landslide inventories from 1957 to 1999, Keefer (2002) shows that even moderate-sized earthquakes can produce large numbers of landslides, and that the number of landslides increases with earthquake magnitude (**Figure 1-11**).

To summarize, landslides, many times triggered by earthquakes, pose a major natural hazard.





**Figure 1-11.** Relation between total number of landslides and earthquake magnitude. Data are for worldwide earthquakes between 1957 and 1999 with comprehensive inventories of landslides. The solid line is the least-squares linear regression (Keefer, 2002).

### 1.3.2 Rockfalls

'Rockfall' is a slope process involving the detachment of rock fragments and their fall and subsequent bouncing, rolling, sliding, and deposition (Varnes, 1978). In some cases 'rockfall' refers to a quantitative measure – describing small phenomena – from block falls of a few  $\text{m}^3$  up to  $10,000 \text{ m}^3$  events, while 'rockslides' is used to describe more than  $100,000 \text{ m}^3$  and 'rock avalanches' can reach several million  $\text{m}^3$  (Dussauge-Peisser et al., 2002). Distinct evidence of rockfall are talus slope deposits at the foot of steep cliff faces, while such evidence is less distinct on slopes covered with vegetation.

Rockfall occurs periodically when one or more blocks fall, bounce and roll down a slope. In case of a talus slope, a block may move further beyond the talus margin, stopping at some distance from the slope base (**Figure 1-12**). These blocks pose the greatest hazard in the vicinity of talus slopes, and the uncertainty of their behavior is a major difficulty in rockfall hazard assessment (Evans and Hungr, 1993).



**Figure 1-12.** A block and its originating cliff behind. The large block has traveled beyond the talus margin. Photo from the study area: Ramim Cliff, Qiryat-Shemona.

### 1.3.3 Rockfall Initiation Mechanisms (Triggers)

Rockfall starts with the detachment of rocks from bedrock slopes (mostly a cliff face). Since all rock outcrops are subject to various degrees of weathering, fracturing leads to jointing and promotion of rockfall (Dorren, 2003). Apart from weathering, trigger mechanisms also determine the occurrence of rockfall. Several of triggering mechanisms have been described in the literature, such as earthquakes (Kobayashi et al., 1990; Vidrih et al., 2001), rainfall and freeze-and-thaw cycles (Matsuoka and Sakai, 1999).

In their study in the Yosemite valley regarding triggering mechanisms and depositional rates, Wieczorek and Jäger (1996) reported rockfall caused by different factors such as earthquakes, rain storms, rapid snow melts, freeze-thaw cycles, root penetration and wedging, or stress relief following deglaciation. Considering precipitation, the highest frequency of slope movements occurred during the colder and wetter part of the season from November through April (**Figure 1-13**) and point out the influence of climatic triggering of rockfall.

As for the distribution of triggering mechanisms of slope movements (including rockfalls) – of the recognized triggering events, rain storms (27%) and rapid snowmelt (8%) triggered more numerous slope movements than earthquakes (5%); however, earthquakes were responsible for a greater cumulative volume (12%) than these other two individual triggers (**Figure 1-14**). Freeze-thaw conditions accounted for only a very small proportion of volume (0.2%) of deposits from documented triggers (Wieczorek and Jäger, 1996).

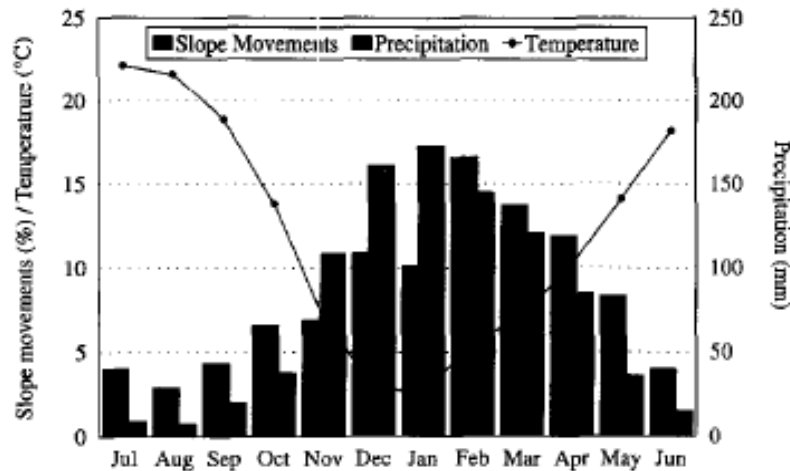


**Figure 1-13.** Monthly temperature, precipitation and percentage of slope movements for the Yosemite Valley. Monthly average temperature (°C) in dotted line; monthly average precipitation (mm) in black (right-hand columns); monthly percentages of slope movements exclude those triggered by earthquakes and those not attributable to any specific month in black left-hand columns of each pair. (after Wieczorek and Jäger, 1996).

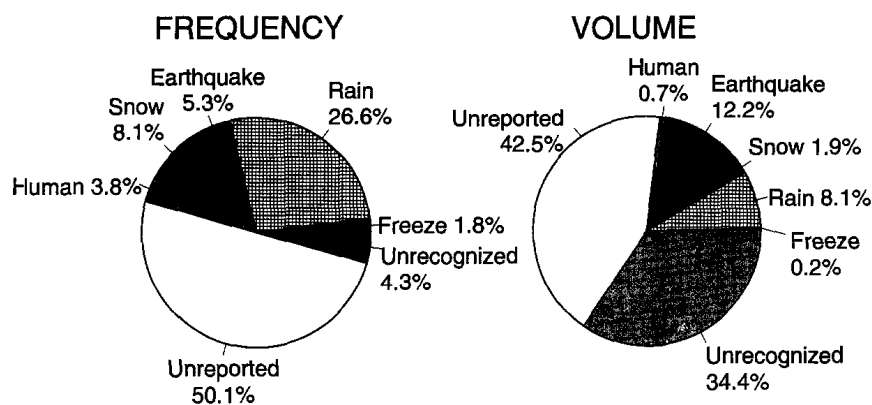


**Figure 1-14.** Types of triggering mechanisms for slope movements. Frequency of occurrence percentage on the left-hand side; percentage of proportion of cumulative total volume of all slope-movement deposits on the right-hand side (after Wieczorek and Jäger, 1996).

To examine the effect of earthquake magnitude and distance on triggering slope movements in Yosemite, Wieczorek and Jäger used the procedure of Keefer (1984), who developed curves representing the upper bound of the maximum distance to different types of landslides in historic worldwide earthquakes of different magnitudes. The solid curve on the plot of earthquake magnitude versus distance (**Figure 1-15**) is Keefer's historical upper limit for disrupted slides or falls based on data from 40 worldwide earthquakes. The Yosemite Valley data falls in agreement with Keefer's upper bound curve.

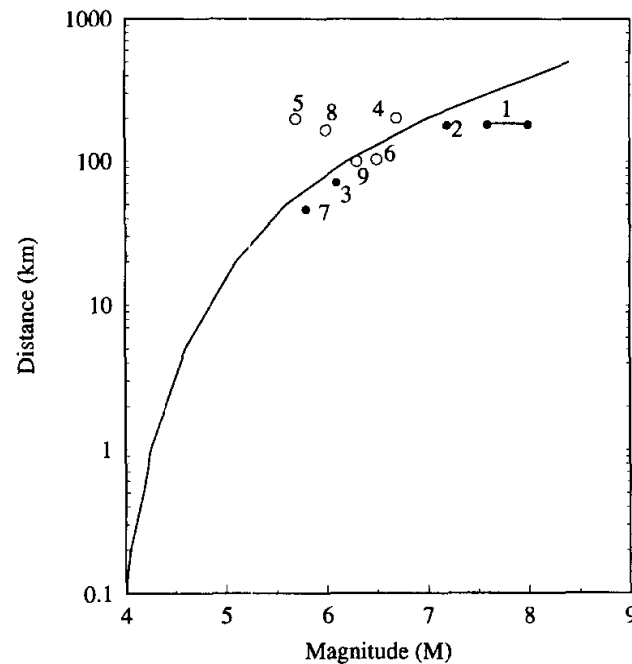


**Figure 1-15.** Distances of rockfalls from the epicenters of earthquakes. Distance to the farthest rockslides or falls triggered in Yosemite Valley (dots); distance to the center of Yosemite Valley for earthquakes felt in Yosemite Valley that did not trigger slides or falls there (circles). Numbers refer to earthquakes listed in a table presented in Wieczorek and Jäger (1996). Solid curve is Keefer's (1984) upper bound from 40 historical worldwide earthquakes that triggered slides or falls (after Wieczorek and Jäger, 1996).

In the Yosemite compilation, few reports suggest freeze-thaw as probable triggering events; However, Wieczorek and Jäger (1996) suggest that the freeze-thaw process may weaken sites for subsequent failure by other triggering events, such as rain storms or earthquakes. They conclude that when triggering events were identified, more slope movements were triggered by large winter rain storms, rapid snowmelt, and earthquakes than by freeze-thaw conditions or human activities. Earthquakes accounted for the greatest cumulative volume of slope-movement deposits from events. Large regional winter storms, with characteristically high daily rainfall and storm total, have the potential for triggering abundant slope movements.

To conclude, rockfalls may be induced by numerous triggering mechanisms, most of them of climatic or seismic nature.

### 1.3.4 Rockfall Path Profile

According to Evans and Hungr (1993), a rockfall-dominated talus slope exhibits a typical profile as the one seen in **Figure 1-16** to which the following description refers. Finer talus fragments accumulate below the apex (point A). The lowermost part of the talus deposit contains the largest fragment sizes, as shown between points B and C. Point C is the base of the talus deposit. Beyond this point the slope is no longer completely covered by talus fragments. The average talus angle is  $\alpha_1$ . The surface to the right of point C consists of material and landforms predating the talus deposits. The part covered discontinuously by scattered large boulders that have rolled or bounced beyond the base of the talus (C-D) is referred as the 'rockfall shadow'. The 'shadow

*angle'* is defined as the angle between the outer margin of the shadow and the apex of the talus slope ( $\beta_2$ ) (Evans and Hungr, 1993).

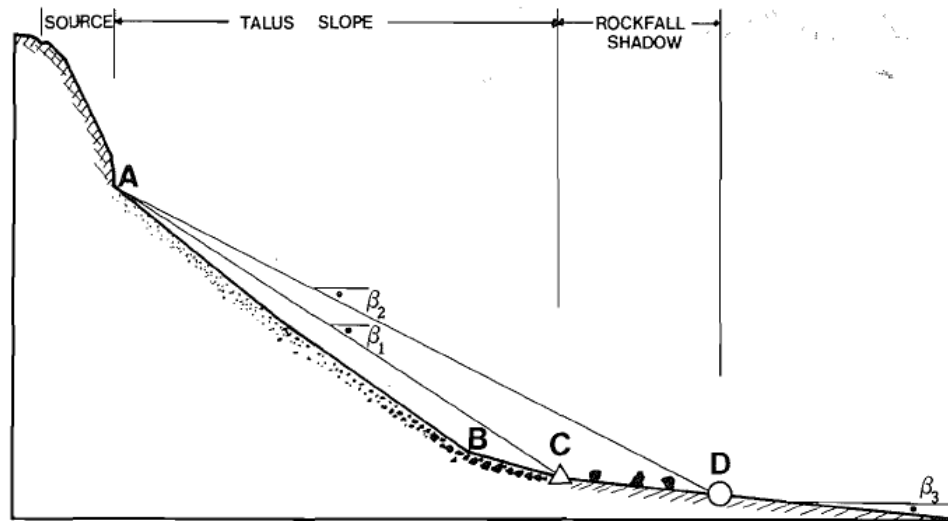


**Figure 1-16.** Schematic diagram of a typical rockfall path profile. A-C is the talus slope with mean angle  $\beta_1$ . C-D is the rockfall shadow with a shadow angle  $\beta_2$  (A-D).  $\beta_3$  is the substrate angle (after Evans and Hungr, 1993).

### 1.3.5 Rockfall Mechanics

Ritchie (1963) presented design criteria describing relationships among variables of cliffs, angle of slopes, depth of ditches, and width of fallout areas. The mechanics of rockfall from cliffs and talus slopes were dealt with in order to suggest various solutions involving ditches and fences to contain the rockfall. Regarding talus slopes, Ritchie (1963) observed that the larger the rock is, the further it gets down slope away from the parent source, and noted that a falling rock spends most time in the air and would come to a stop when the slope gets flat enough and the irregularities of the slope are large enough to lodge the rock itself and diminish its velocity. He suggested a mechanical approach to describe rockfall trajectory, describing the rock's path as a series of parabolic paths, influenced by the impact angle which determines the velocities along and normal to the impact plane (**Figure 1-17**). Ritchie (1963) suggested that the size and shape of a rock have little bearing on its falling or rolling characteristics. He concluded that since a falling rock must obey certain natural laws of mass, energy, velocity, impact and restitution, while being influenced by friction, gravity and time, "it seems only reasonable that the behavior of falling stones would lie between certain limits, limits that can be used as a basis for design to contain them." (Ritchie, 1963).

Ritchie's mechanical considerations relate to a single rock in its movement (**Figure 1-17**) which is not influenced by neighboring rock fragments participating in the rockfall. Rockslides, where a large slope mass of numerous rock blocks moves collectively, are not the case discussed here. Such cases rely on dynamic velocity analyses and conceptual models of the center of gravity of the moving mass and several assumptions regarding its starting end ending points, along with considerations about the influence of particles (blocks) within the total moving rock-mass and

other factors (Erismann and Abele, 2001). The model used in this study predicts the down-slope movement of individual falling rock blocks.

The following sections detail the main aspects of rockfall mechanics which are introduced into rockfall models.

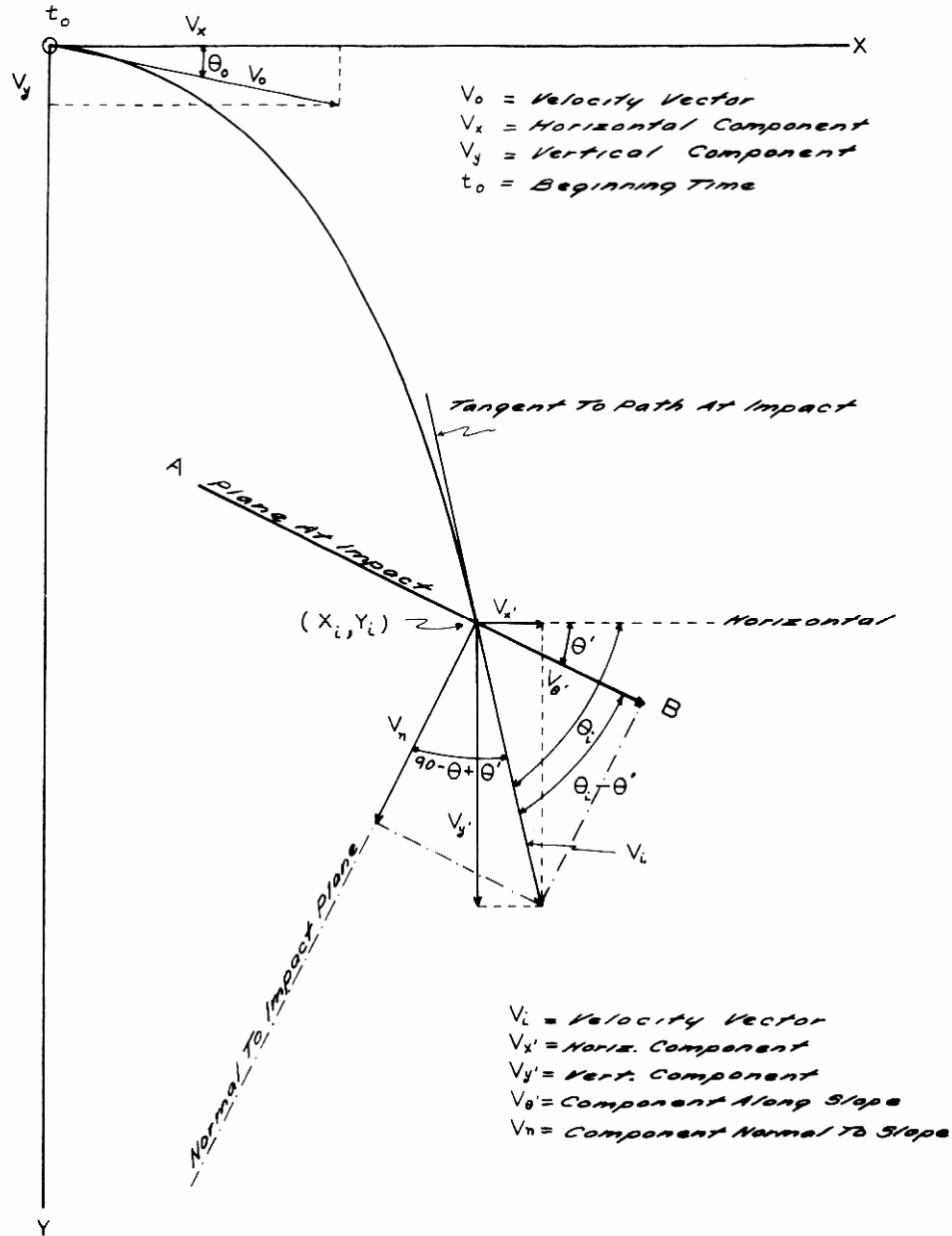


**Figure 1-17.** Ritchie's theoretical considerations of rock trajectory. Velocity components related to the moving block's path and plane of impact (after Ritchie, 1963).

### 1.3.5.1 Modes of Motion of Rocks

Once the rock has been detached and starts to move, it descends the slope in different modes of motion that strongly depend on the mean slope gradient (**Figure 1-18**). The three most important modes of motion are *freefall* through the air, *bouncing* on the slope surface and *rolling* over the slope surface. These modes of motion will be shortly detailed in the following sections.

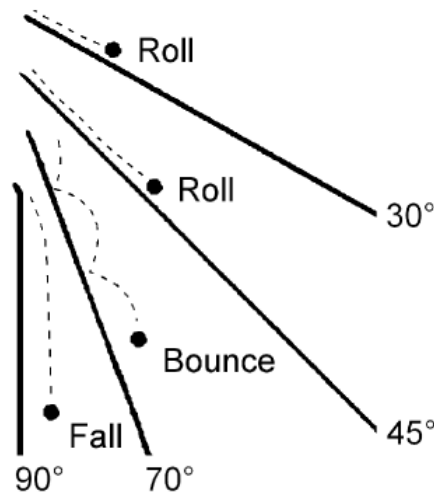


**Figure 1-18.** General modes of motion of rocks during their descent on slopes. Modes are related to the mean slope gradients (after Dorren, 2003).

#### 1.3.5.2 Freefall of Rocks

Freefall of rocks occurs on very steep slopes. According to Ritchie (1963) freefall occurs if the slope gradient below the potential falling rocks exceeds  $76^\circ$  but in different field situations this value varies. **Figure 1-18** indicates that around  $70^\circ$  the motion of the rock gradually transforms from bouncing to falling.

#### 1.3.5.3 Bouncing and Rolling of Rocks

When the mean slope gradient decreases in the down-slope section, a freefalling rock collides on the slope surface, which is defined as bouncing. During the first bounce rocks tend to break, especially heavily fractured rocks (Bozzolo and Pamini, 1986). Whether or not a rock breaks, about 80% of the kinetic energy gained in the initial fall is lost in that first impact (Dorren, 2003).

If the mean slope gradient is less than about  $45^\circ$ , a bouncing rock gradually transforms its motion to rolling because it gathers rotational momentum. During the transition between bouncing and rolling, the rock rotates very fast and only the edges with the largest radius maintain contact with the slope. Thus, the center of gravity moves along an almost straight path, which is an effective mode of motion with respect to energy loss. In fact, this combination of rolling and short bounces is one of the most economic displacement mechanisms (Erismann, 1986).

#### 1.3.5.4 Stopping of Moving Rocks

A moving rock's velocity (and therefore stopping of a falling rock) mainly depend on the mean slope gradient. Falling rocks generally accelerate on steeper slopes and decelerate on flatter slopes (Dorren, 2003). The velocity also depends on the size of the rock and on the material

covering the slope such as soil and vegetation. Small rocks slow down more easily than bigger rocks. First, because during a rockfall the total kinetic energy of small rocks is lower than that of bigger rocks; secondly large obstacles can more easily stop small rocks; thirdly, small rocks slow down more easily in depressions between larger rocks on talus slopes. Evans and Hungr (1993) point out the fact that has been observed by many authors: the biggest rocks are mostly found near the base of the talus slope.

The friction force of a moving rock is not only dependent on the rock shape, but also on the surface characteristics of the slope, which is related to the surface roughness (Chang, 1998; Dorren, 2003; Jones et al., 2000). Surface roughness can be defined as the variation in height perpendicular to the slope within a certain slope distance (Jones et al., 2000; Pfeiffer and Bowen, 1989). See *section 3.2.1.4* for detailed properties of surface roughness.

### 1.3.6 Rockfall Volume Statistics

Rockfall inventories are addressed in frequency-volume distributions, unlike other types of landslides which are usually given in terms of frequency-area statistics (Malamud et al., 2004). Cumulative frequency-volume statistics for rockfalls have been presented for the Grenoble area of the French Alps, the Yosemite Valley, USA and worldwide (Dussauge-Peisser et al., 2002; Dussauge et al., 2003). These authors correlate their frequency-volume data with power-laws of the form:

$$N(V) \sim V^{-b} \quad (1-1)$$

With  $V$  the rockfall volume,  $N(V)$  the number of events greater than  $V$  and  $b$  a parameter with a negative slope ranging between  $0.4 \pm 0.2$  in different worldwide inventories (Malamud et al., 2004). The equivalent negative slopes for the non-cumulative frequency-volume distributions are  $1.4 \pm 0.2$  (Malamud et al., 2004).

Rockfall frequency density function is defined as the number of rockfalls with volumes between  $V_R$  and  $V_R + \Delta V_R$ , divided by the width of that bin  $\Delta V_R$ :

$$f = \frac{\delta N_R}{\delta V_R} \quad (1-2)$$

with  $f$  frequency density as function of rockfall volume  $V_R$ ,  $N_R$  The number of rockfalls and  $\Delta V_R$  the volume bin width.

Guzzetti et al. (2003) examined rockfalls and rockslides in Yosemite Valley, USA and fit their data to a non-cumulative frequency density function with a negative power-law exponent ( $b$  value) of about -1.1 (*Figure 1-19*).



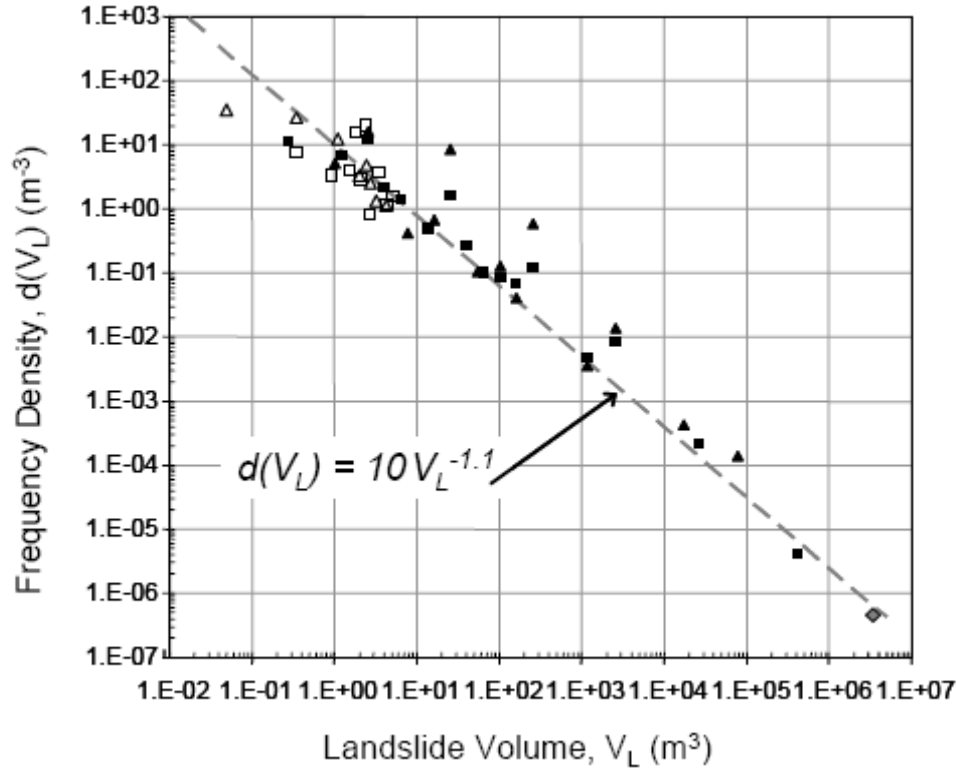


**Figure 1-19.** Frequency density of Yosemite rockfalls (squares) and of rockslides (triangles). Black symbols represent the entire catalogue (1867-2002); Open symbols the period 1980–2002, for which the catalogue is complete and reliable. The gray diamond represents 5 prehistoric rock avalanches. The dashed gray line is a power law fit with exponent,  $b = -1.1$  (after Guzzetti et al., 2003).

Malamud et al. (2004) reviewed rockfall inventories and presented the frequency density of rockfalls ( $f = N_R / V_R$ ) as a function of rockfall volume  $V_R$  for three inventories (two of them are mentioned above): a. 157 rockfalls and slides triggered by the Umbria–Marche earthquakes of September and October 1997 in Italy; b. 135 rockfalls and slides in the Yosemite region of California during the period 1980–2002 (Guzzetti et al., 2003; Wieczorek et al., 1998); c. 89 historical rockfalls in the Grenoble region of France, estimated to date from the period 1904–1996 (Dussauge et al., 2003; RTM, 1997). Also plotted on the same **Figure 1-20** is the power law frequency-volume distribution

$$\log f(V_R) = +1.07 \log V_R + 0.37 \quad (1-3)$$

with  $f$  in  $\text{km}^{-3}$  and  $V_R$  in  $\text{km}^3$ ;  $r^2 = 0.98$ . (Malamud et al., 2004).

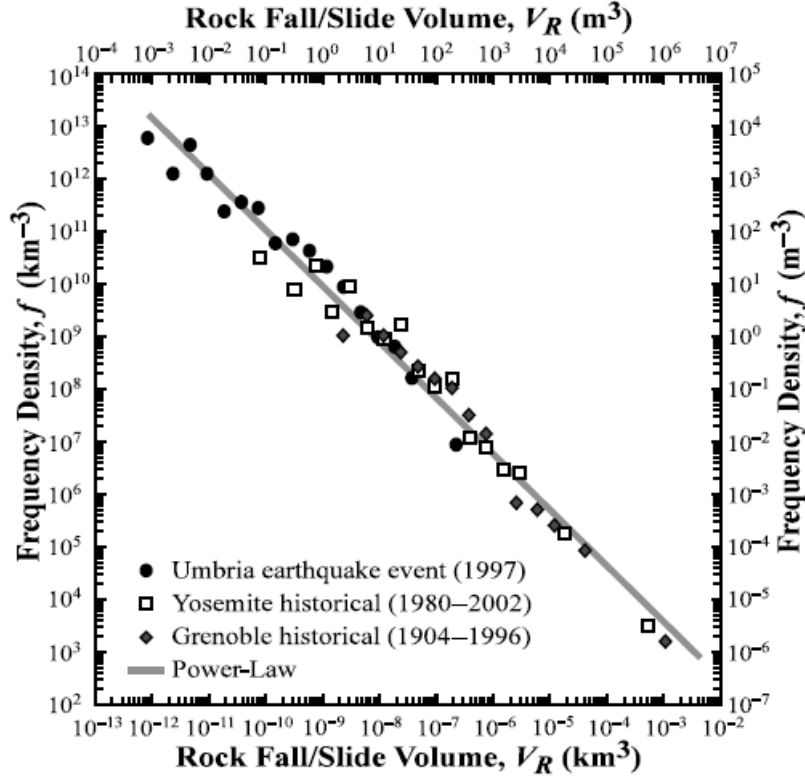


**Figure 1-20.** Dependence of the frequency density  $f$  on volume  $V_R$  for rockfall and rock-slide inventories, both on logarithmic axes. The straight line is the power-law regression given by  $\log f = -1.07 \log V_R + 0.37$  (after Malamud et al., 2004).

The landslide probability density ( $p$ ) given by Malamud et al. is

$$p = \frac{1}{N} \frac{\delta N_L}{\delta A_L} \quad (1-4)$$

where  $N$  is the total number of landslides in the inventory and  $N_L$  is the number of landslides with area between  $A_L$  and  $A_L + \delta A_L$ . Following that, Katz and Aharonov (2006) converted block surface area distributions resulted from a sandbox shaking experiment to volume distributions suggesting that rockfall volume probability distribution ( $p$ ) follows a power law

$$p = \frac{dN}{NdV} \sim V^\alpha \quad (1-5)$$

where  $\alpha$  equals  $-1.13$ , close to the slope measured for natural rockfall inventories, for which  $\alpha$  equals  $-1.07$  (Malamud et al., 2004).

To conclude, the probability density function for rockfall volume  $p$  follows a power law of the form

$$p = aV_R^\alpha \quad (1-6)$$

where  $a$  is a linear factor,  $V_R$  is the rockfall volume and  $\alpha$  equals about  $-1.1$ . This has proven to fit worldwide rockfall and rockslide inventories, implying a possible global correlation between rockfall volume and its probability density function, which provides the probability for a given rockfall volume in a given area.

### 1.3.7 Comparison of Rockfall Models

Most of the existing rockfall models for calculating runout zones of rockfall events can be categorized in 3 main groups: a. empirical models; b. process-based models; c. GIS-based models (Dorren, 2003). The basic principles of the empirical and GIS-based models are shortly described in the following sections, since they are not in use in this study, process-based models will be detailed more extensively.

#### 1.3.7.1 Empirical Models

Empirical rockfall models are generally based on relationships between topographical factors and the length of the runout zone of one or more rockfall events. Evans and Hungr (1993) suggest the *Fahrböschung* principle after Heim (1932) to predict runout zones of rockfall events. The *Fahrböschung* is the angle between a horizontal plane and a line from the top of a rockfall source scar to the stopping point for any given rockfall (**Figure 1-21**). An alternative principle suggested by Evans and Hungr (1993) is the *minimum shadow angle* after Lied (1977). This is the angle of a straight line between the highest point of the talus slope and the stopping point of the longest runout boulder for any given rockfall (**Figure 1-21**). Comparing the results of several studies, the minimum shadow angle lies between 22° and 30° (Dorren, 2003).

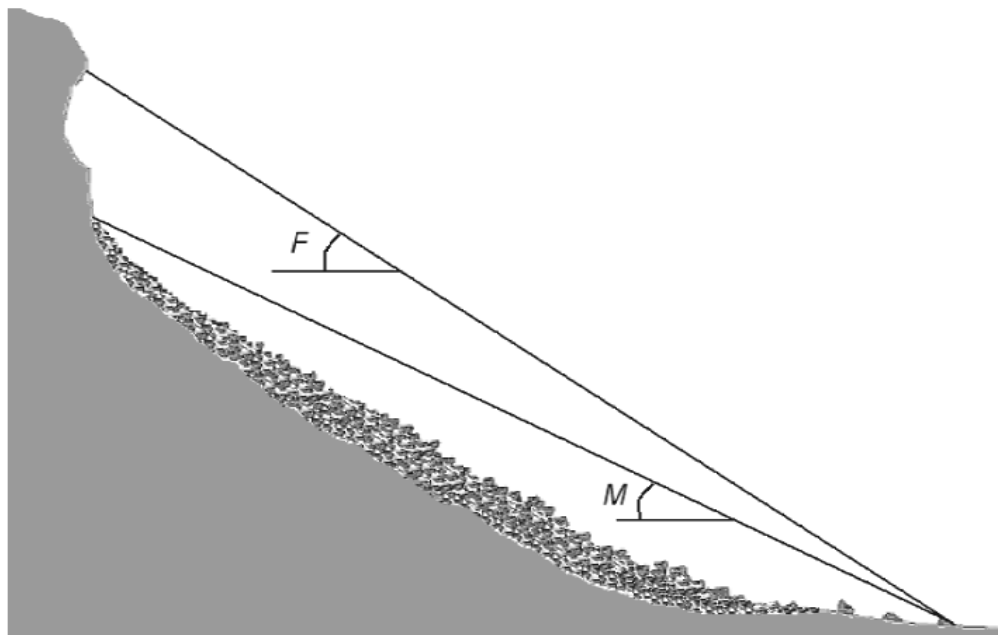


**Figure 1-21.** *Fahrböschung (F) and minimum shadow angle (M) of a talus slope (after Dorren, 2003).*

#### 1.3.7.2 GIS-Based Models

GIS-based models are those either running within a GIS environment or they are raster based models (a row-oriented representation of images where each pixel holds representative data e.g. elevation or slope angle) for which input data is provided by GIS analysis. GIS-based rockfall models usually consist of three procedures: a. identification of the rockfall source areas in the

region of interest; b. determination of the rockfall trajectory; c. calculation of the length of the runout zone (Dorren, 2003).

GIS-based models serve as a basis for computerized rockfall simulation programs, which in some cases use a three dimensional model to compute rockfall trajectories (Agliardi and Crosta, 2003b; Crosta and Agliardi, 2004; Guzzetti et al., 2002; Guzzetti et al., 2004). Such programs were not used in this study, due to unavailability and extensive high-resolution input requirements.

### 1.3.7.3 Process-Based Models

Process-based models describe or simulate the modes of motion of falling rocks over slope surfaces (Dorren, 2003). Kirkby and Statham (1975) developed a process-based rockfall model for transport of rocks over talus slopes, assuming that rocks only slide over a talus slope surface. Based on that model, Keylock and Domaas (1999) developed the *simple dynamics rockfall model*, which calculated rock block travel distance over the slope surface on the basis of the friction force and the acceleration due to gravity. They concluded that the *simple dynamics rockfall model* did not appear to hold a significant advantage over the empirical models tested in their study.

Another large group of rather similar process-based models (Azzoni et al., 1995; Bozzolo and Pamini, 1986; Evans and Hungr, 1993; Kobayashi et al., 1990; Pfeiffer and Bowen, 1989) share the following: a. models are two-dimensional slope-scale models that restrict falling boulders to move in a vertical plane (i.e. lateral movements are not simulated); b. the rockfall track is defined as a series of connected straight lines with a mean slope angle for each such segment of the rockfall track (**Figure 1-22**); c. motions are simulated as a series of flying and contact phases. The flying phase is simulated with a parabola equation based on the initial velocity in  $x$  and  $y$  directions and the acceleration due to gravity. The collision point of the rock on the slope surface is calculated with the intersection of the parabolic flying function and the straight slope segments. According to Dorren (2003) the major differences between these two dimensional models are: a. in the representation of the block mass - some represent the falling rock as a concentrated mass point (Evans and Hungr, 1993; Kobayashi et al., 1990; Pfeiffer and Bowen, 1989), while others consider the block as an ellipsoidal body (Azzoni et al., 1995; Bozzolo and Pamini, 1986); b. the modes of movement – some use detailed characterizations for bouncing, sliding and rolling (Azzoni et al., 1995; Bozzolo and Pamini, 1986; Evans and Hungr, 1993; Kobayashi et al., 1990), while others consider bouncing, rolling and sliding as identical movements that can be described by a series of bounces and impacts (Pfeiffer and Bowen, 1989).

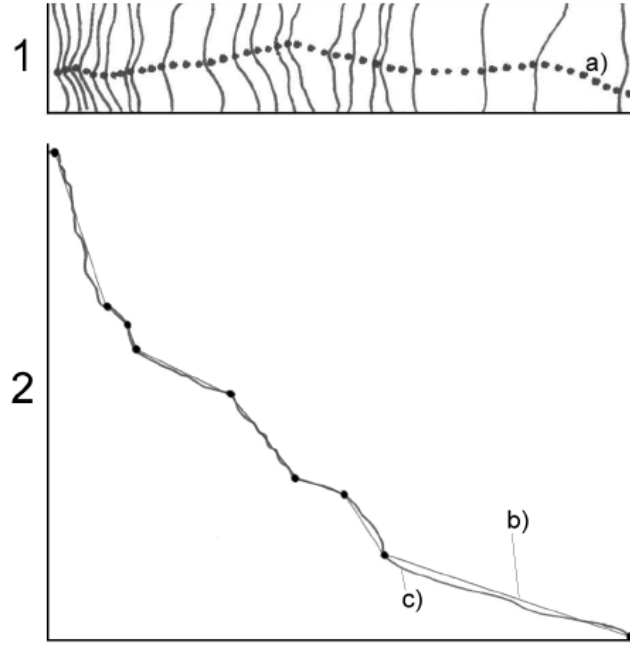


**Figure 1-22.** The upper figure (1) shows the actual rockfall path (a) projected on a height contour line map. The lower figure (2) shows the slope straight-line segments (b) used in two-dimensional rockfall models representing the actual slope of the rockfall path (c) (after Dorren, 2003).

Models applying specific algorithms for calculating rolling and sliding velocities mainly use Coulomb's law of friction

$$F_f = \mu_f * m * g * \cos \beta \quad (1-7)$$

where  $F_f$  is friction force tangential to the slope surface ( $\text{kg} \cdot \text{m} \cdot \text{s}^{-2}$ );  $\mu_f$  is coefficient of friction;  $m$  is mass of the rock (kg);  $g$  is acceleration due to gravity ( $9.81 \text{ m} \cdot \text{s}^{-2}$ );  $\beta$  is mean slope gradient in degrees (Dorren, 2003).

Kobayashi et al. (1990) developed a model, which used different characterization for bouncing and rolling, based on the coefficient for efficiency of collision. Their results were all within 30% range of the measured rockfall runout zones and bounce marks. Their main conclusion was that block shape is important in governing the modes of motion, but variations in topography control it (Dorren, 2003).

Pfeiffer and Bowen (1989) developed a model using tangential and normal coefficients of restitution, with a mass concentrated in one point. Velocity before each impact was resolved into tangential (parallel to slope) and normal (perpendicular to slope) velocities, which were both recalculated after impact according to the tangential and normal coefficients of restitution. The tangential coefficient was determined by vegetation cover and surface roughness, while the normal coefficient was determined by the elasticity of the surface material. Rolling was simulated as a series of impact and bouncing events (Dorren, 2003).

All the above-described process-based slope-scale models did not simulate multiple falling rocks and the complex interactions between them.

According to Dorren (2003), process-based models produce more accurate predictions of runout zones, and seem to be most suitable for application in areas other than the areas where they were developed and calibrated.

### 1.3.8 Rockfall Simulation Programs

Several computer programs have been developed and tested to simulate the fall of a boulder down a slope and to calculate rockfall trajectories (**Table 1-3**). Most of the programs implement either a lumped mass (a mass concentrated to a dimensionless point) or a rigid body approach. For the latter, a simple geometry for the boulder (e.g., a sphere, a disk, a cylinder) is assigned. Some programs (Azzoni et al., 1995; Bozzolo and Pamini, 1986; Jones et al., 2000; Pfeiffer and Bowen, 1989) used hybrid approaches, i.e., a lumped mass approach for simulating free fall and a rigid body approach for simulating rolling, impact and rebound. Most of the programs work along user-defined slope profiles, and require detailed information on the materials (soil, debris, rock) cropping out along the slope and the corresponding friction and energy restitution coefficients. Slope profiles are usually obtained from large-scale topographic maps or through topographic surveys. Lithological and land-use conditions along the slope are obtained from field surveys, geological, soil and land-use maps, and the interpretation of aerial photographs (Guzzetti et al., 2002).

**TABLE 1-3 Main Characteristics of Some Computer Rockfall Simulation Programs\***

Year	Author(s)	Program name	Dimensions	Approach	Probabilistic
1976	Piteau and Clayton	Computer Rockfall Model	2-D	Lumped mass	Partly
1982-86	Bozzolo and Pamini	SASS—MASSI	2-D	Hybrid	Yes
1985	Bassato et al.	Rotolamento Salto Massi	2-D	Lumped mass	No
1987	Descouedres and Zimmermann	Eboul	3-D	Rigid body	No
1989-91	Pfeiffer and Bowen	CRSP	2-D	Hybrid	Yes
	Pfeiffer et al.				
1990	Kobayashi et al.	—	2-D	Rigid body	No
1991-95	Azzoni et al.	CADMA	2-D	Hybrid	Yes
1991	Scioldo	Rotomap	3-D	Lumped mass	No
1998	Stevens	RocFall	2-D	Hybrid	Yes
1999	Paronuzzi and Artini	Mobyrock	2-D	Lumped mass	Yes
2000	Jones et al.	CRSP 4.0	2-D	Hybrid	Yes
2002	This work	STONE	3-D	Lumped mass	Yes

\* Table after Guzzetti et al. (Guzzetti et al., 2002). The program used in this study is CRSP v4.

Guzzetti et al. (2002) point out that most of these programs work reasonably well only in small areas for which detailed thematic information (including topography) is available.

Giani et al., (2004) evaluated two-dimensional and three-dimensional rockfall simulation models, with CRSP as the 2-D model. They studied Apennines and Alps cliffs (both in Italy) and pointed out some important conclusions, some of them are brought here:

- Block trajectories calculated by the 3-D model (**Figure 1-23**) show that the rockfall phenomenon is characterized by a predominant 2-D development; the rockfall paths form narrow bundles of mostly parallel trajectories, sub-perpendicular to the cliff strike. Hence the validity of two-dimensional models is intensified.

- The motion efficiency is higher for blocks having spherical shapes and smooth surfaces than for blocks having irregular surfaces and sections (pointing out a spherical rock shape as a ‘worst-case’ scenario, as described later in this study).
- The back analysis performed confirms that both on-site tests and numerical modeling results are valid instruments to understand this natural phenomenon and the design of rockfall protection systems.

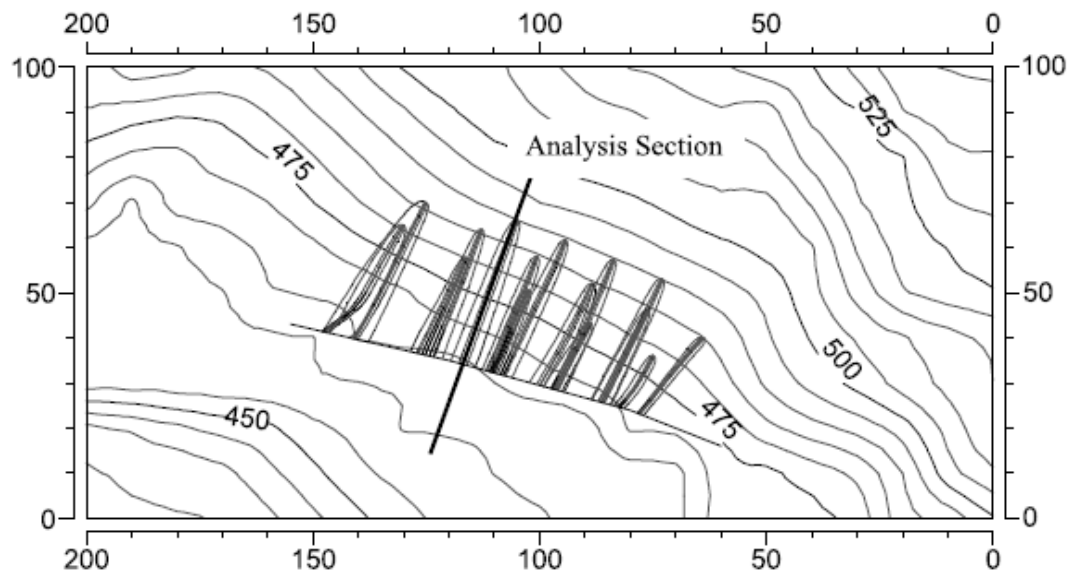


Figure 1-23. Rockfall paths resulting from the 3D simulation (Apennines site). Paths lead from cliff to highway. The dimensions and elevation contours are in meters. 3-D trajectory calculations show that the rockfall phenomenon is characterized by a predominant 2-D development; the rockfall paths form narrow bundles of mostly parallel trajectories, sub-perpendicular to the cliff strike (after Giani et al., 2004).



## Chapter 2

---

### Methods

**S**everal methods of data acquisition and processing used in this study are presented in this chapter: a. OSL method for determining the ages of rockfalls and helping to elucidate the triggering mechanism; b. Colorado Rockfall Simulation Program (CRSP v4) for calculating the trajectories of rockfalls and assessing their impact hazard; c. acquisition of block data from field and aerial photos used to calculate block size probabilities for rockfall hazard evaluation and mitigation design.

#### 2.1 Block Data Acquisition

Collection of block data was preformed in a part of the study area (detailed below), where blocks were mapped, marked and measured for volume. This data was later used to compile the block size distribution statistics required for hazard analysis.

##### 2.1.1 Outline of the Mapping Area

Block mapping area defined for field data collection is bounded by a number of topographic-morphologic entities (*Figure 2-1*). The total mapping area is 110,000 m<sup>2</sup> (on map). Boundaries of that area are as follows. West: the lower boundary of the rockfall talus (outlined in yellow); south: a stream running due from the escarpment edge to a road trending north-south, which also comprises the eastern boundary; north: a small wadi running from the fault at the cliff and east to the crossroad at the entry point to the geological park, where it meets the eastern boundary road. Mapping area boundaries are outlined in purple in *Figure 2-1*.

At first glance, the talus located up slope just below the escarpment holds a vastly larger quantity of rock blocks than the selected mapping area, so it seems a better candidate for collection of block volume distribution. But it is that same reason which disqualifies it as representative – its the blocks which have traveled beyond it, although more scarce, which represent a more feasible block volume distribution in future rockfalls – the lower part is where the blocks that travel the largest distances from the cliff have come to stop (which are still evident today), thus posing the greatest evident hazard to town (blocks at the eastern, lower parts of the slope have been masked by the construction of town). Block volume statistics were therefore based on the lowest part of the slope where blocks are still evident, as detailed below.



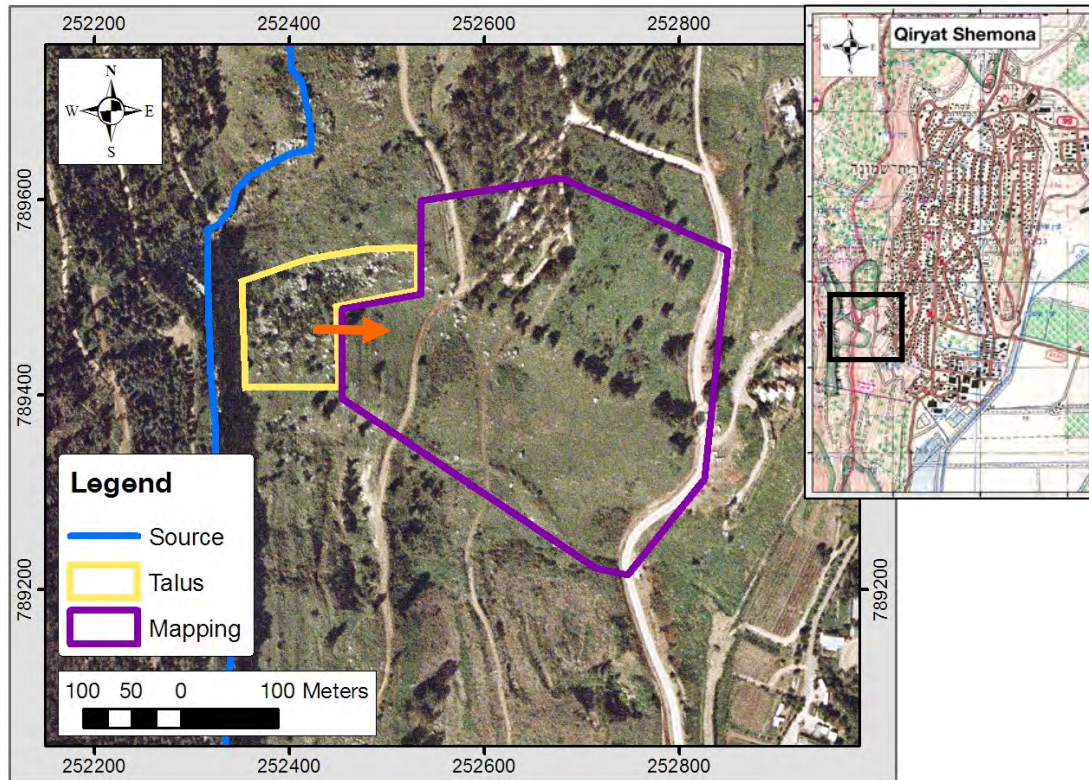


**Figure 2-1.** Block mapping area. Large blocks can be spotted. Orange arrow marks the point of view of the next figure below. Inset: black rectangle is map outline.



**Figure 2-2.** View over the Talus southern boundary east towards Qiryat-Shemona (point of view marked in the figure above). The yellow line marks the boundary between the talus (middle and left-hand side) and the mapping area below it.

### 2.1.2 Block Mapping

Rock blocks were located (GPS coordinates), measured for size (volume), photographed and marked for further reference. Practically every block larger than  $1.0 \text{ m}^3$  (and, in some cases, even smaller blocks) was accounted for. A catalog of block data was compiled for analysis, containing 97 blocks (47 other large blocks were documented within the talus area at an earlier stage of the study, but they were excluded later from the statistics, being situated off the

mapping area; some of them were used for the past block volume estimation process described below). Block volumes at the mapping area vary between  $0.1 \text{ m}^3$  and  $125.0 \text{ m}^3$ . Statistical analysis was applied only to the 76 blocks of volumes larger than  $1.0 \text{ m}^3$ . The smaller blocks are of negligible importance in terms of hazard assessment anyway.

### 2.1.3 Block Volume Measurements

Volumes of 144 blocks (97 in the mapping area + 47 in the talus area) were obtained using a measuring tape. For each block, dimensions in 3 axes were measured and multiplied to calculate block volume, which should be taken with a grain of salt since no block is really an orthogonal box shape. The accuracy of the tape is 1 cm and the error of the dimensions measurements is about  $\pm 10\text{cm}$ , which may yield a volume error of 15% ( $\sim 1.5 \text{ m}^3$ ) for small blocks ( $10 \text{ m}^3$ ), 10% ( $\sim 5 \text{ m}^3$ ) for medium sized blocks ( $50 \text{ m}^3$ ) and 5% ( $7 \text{ m}^3$ ) for the largest blocks ( $125 \text{ m}^3$ ). The full catalog of field observed blocks is presented in *Appendix B*.

### 2.1.4 Diameter Estimation of Non-Mappable Blocks

Since Qiryat-Shemona was constructed, blocks which traveled down-slope beyond the current town border are not available and are not mappable in the field. However, we have a record of these blocks on aerial photos from 1946 and 1951. Estimation of the size of these blocks (thus estimating block dimensions predicted to impact the town premises), was carried out in 3 stages:

1. Find a correlation between field measured volume of blocks (3D) and their maximal dimension (2D) measured on an orthophoto in GIS.
2. Measure maximal dimensions of non-mappable blocks on the 1946-1951 aerial photos using GIS.
3. Use the correlation found in stage 1 to assign volumes and estimated diameters for the blocks found in stage 2 (CRSP input size is diameter).

#### Stage One: Maximal GIS Dimension and Block Volume

58 blocks identified both on the aerials (1946-1951) and in the field were used to correlate maximal GIS measured dimension to block volume, having their volumes measured. These blocks were measured for maximal length dimension using the GIS distance measuring tool (0.1 m accuracy).

#### Stage Two: Maximal Dimensions of Past-Existent Blocks

Non-mappable blocks (already masked or hidden under vegetation) were identified on the aerial photos from 1946-1951 and measured for maximal dimension using the GIS distance measuring tool.

#### Stage Three: Estimated Diameters of Masked Blocks

Finding a correlation between measured GIS dimensions and estimated diameter:

- a. Set a table of block diameters of 0.5–7.0 m with 0.5 m intervals.

- b. Calculate block volume (spherical) for each diameter in that table.
- c. Calculate maximal dimension in GIS for each volume in (b) using the correlation found in *stage one* above.
- d. Find a correlation between the maximal GIS dimensions found in (c) and corresponding block diameter in (a) using a linear regression.

This correlation allows assigning an estimated spherical block diameter for every non-mappable block on the aerial photos from 1946–1951 by measuring its maximal dimension using GIS.

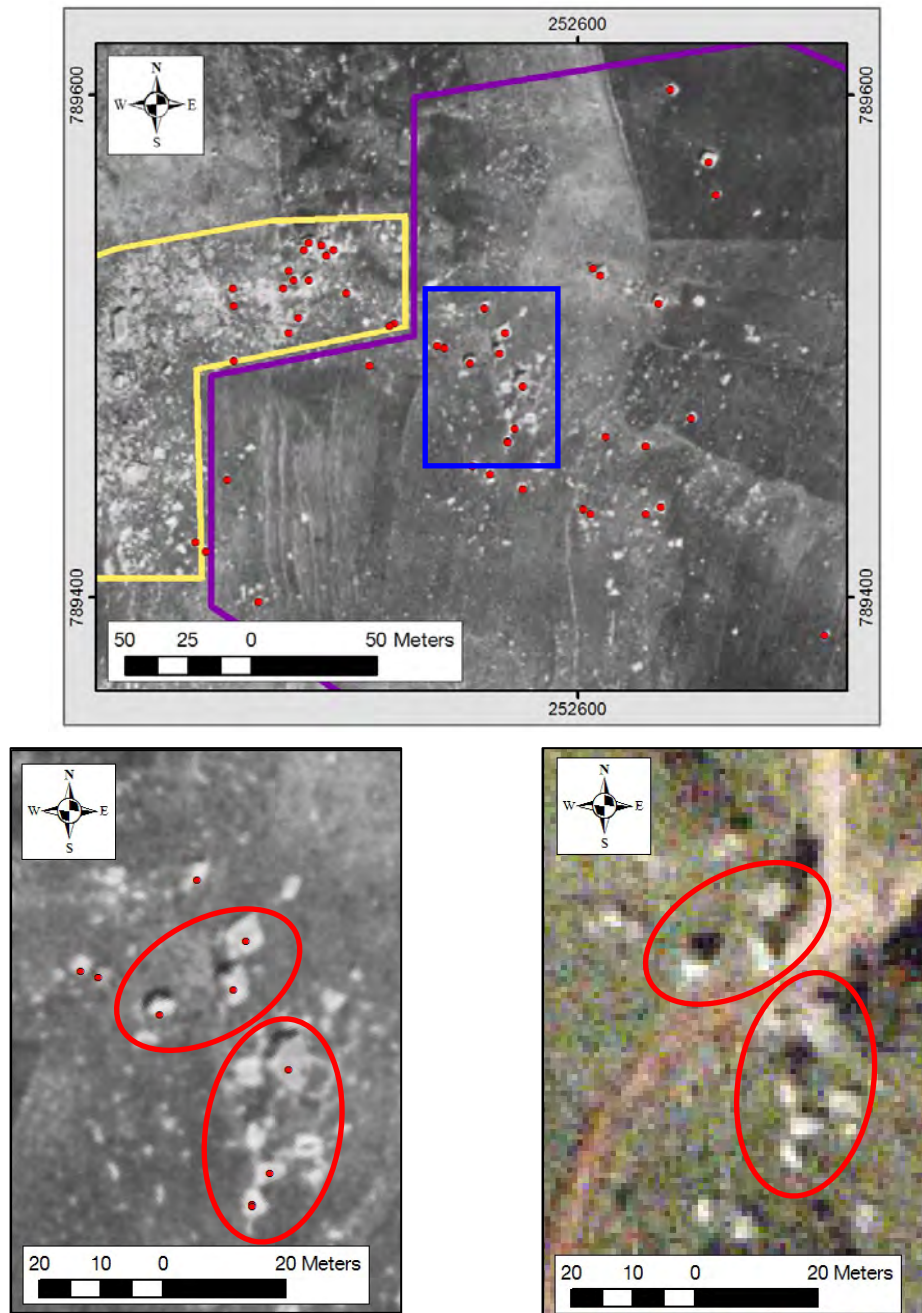


**Figure 2-3.** Correlating maximal GIS dimension to measured block volume. **Top:** blocks identified both on aerials and in field (red circles); mapping area perimeter in purple; talus perimeter in yellow; inset of bottom figures in blue. **Bottom:** blocks measured in GIS for maximal dimension. Notice the identification of blocks from 1946 (left) and 2007 (right) marked in red ellipses.



## 2.2 OSL Age Determination

### 2.2.1 What is OSL Dating?

OSL stands for *Optically Stimulated Luminescence* – a branch of *luminescence*, which refers to the light emitted by some materials in response to some external stimulus processes (Lian and Roberts, 2006). In the case of OSL, the stimulus is ionizing radiation by visible light. Occurrence of luminescence has been known for at least 450 years: first scientific description of the phenomena is related to Gesner (1555), the first experiments to Boyle (1664), and Aitken (1998) published relevant summaries of luminescence dating. Luminescence dating has been shown to work for samples as young as a few years, or as old as several hundreds of thousands of years, and it gives calendar ages directly. The upper theoretical age limit is thought to be a few million years (Lian and Roberts, 2006). For further detail of the osl dating method, see Lian and Roberts (2006).

### 2.2.2 Field OSL Sample Collection

Dating rockfalls using the soil at the interface beneath the block's bottom face was performed by Becker and Davenport (2003) by drilling from the top of a fallen block situated on the slope to the interface at its bottom and radiocarbon dating the soil sample.

In this study, a different method was used. We excavated a ditch beside the block to reach its interface with the soil, then manually excavated under the block in order to sample the soil at the interface below its center. Sampling of soil was performed in the dark under a thick wool blanket cover in order to prevent sunlight exposure from the soil samples (*Figure 2-4 a; b*).

Dating the rockfalls was based on these assumptions:

1. All sampled blocks did not move from their post-rockfall location. This is based on two considerations: a. only very large blocks, weighing hundreds of tons, were sampled; b. the blocks lay on a slope undisturbed by large-scale human activity, where no heavy mechanical machinery had been operated.
2. Soil samples from the interface between blocks and their underlain soil had been exposed at the surface during the time of impact of the block, and have been buried underneath that block ever since.
3. Dating the above soil interface means dating the last time it had been exposed to sunlight on the surface, which in this case is equal to the time of block impact.
4. The above date of block impact represents the time of the rockfall occurrence, assuming blocks travel to their post-rockfall location in a very short time span (tens of seconds). Whether or not the block has reached its current location not from the source cliff, but

in a secondary rockfall event is less important, because it anyway means a rockfall event had occurred at that time, which is the required fact in the first place.

OSL tests on quartz fractions from the soil samples, a slope debris component originated at the sandstone of the Hatira Formation (comprising the slope along which rockfall occurred) were performed in collaboration with Naomi Porat at the luminescence dating laboratory, Geological Survey of Israel.



**Figure 2-4.** Soil samples collection for OSL dating. *a.* ditch excavation beside the block using a tractor (left); *b.* manual excavation of soil sample from interface beneath the block, performed under a blanket cover to prevent exposure of the sample to sunlight (right).

## 2.3 Colorado Rockfall Simulation Program

*Colorado Rockfall Simulation Program (CRSP V4)* is a computer program which simulates rocks tumbling down a slope (Jones et al., 2000). The program development and algorithm are described in chapter 2 of the program's User Manual (Jones et al., 2000).

### 2.3.1 Rockfall Trajectory Analysis

The down-slope trajectory of a rock-block (or the energy lost by a block as it travels down slope) is affected by slope geometry, slope material properties, rock geometry and rock material properties (Agliardi and Crosta, 2003a; Ritchie, 1963). Parameters that quantify these factors are used to simulate rockfall behavior. The model input parameters are slope profile and its surface roughness, slope rebound and friction characteristics and block morphology. Model

output is a statistical distribution of velocity, kinetic energy and bounce height along the down slope trajectory, including stopping distances of the blocks.

Using CRSP provides information on two major aspects of rockfall hazard evaluation. First, the results of rockfall simulation along a given slope are used to outline areas subject to rockfall hazard. Second, the statistical distributions of travel velocities and kinetic energy serve as basis for both hazard analysis and rockfall mitigation considerations. The program needs to be calibrated for local study area to fit its unique geologic and morphologic surface conditions.

### 2.3.2 Rockfall Behavior and CRSP Input Parameters

The different parameters which control rockfall trajectories, along with short descriptions of their affect on rockfall behavior, are described below following the CRSP manual (Jones et al., 2000).

#### 2.3.2.1 Slope Geometry

Slope geometry is defined by slope angle, slope length, surface roughness and lateral variability. Slope angle defines the zones of acceleration and deceleration of the fall; Slope length determines the distances along which rocks accelerate or decelerate. The slope profile is introduced into CRSP by creating a 2D profile out of ‘cells’ that have beginning and end X-Y coordinates. Each ‘cell’ is a straight line segment which defines its slope angle ( $\Phi$ ). Cell boundaries are selected where the analyzed natural slope changes its angle or characteristics. Each profile cell is assigned the parameters defining slope properties, namely surface roughness, tangential and normal friction coefficients. Irregularities in the slope surface account for most of the variability observed among rockfall events originating from a single source location. These irregularities, referred to as **surface roughness** ( $S$ ) alter the angle at which a rock impacts the slope surface. CRSP models surface irregularities by randomly varying the slope angle at block impact between limits defined by the rock size and surface roughness. **Surface roughness** ( $S$ ) is defined as the perpendicular variation of the slope within a slope distance equal to the radius of the rock (**Figure 2-5**). It is a function of rock diameter and the irregularity of the surface used to estimate the possible variation of the slope angle relative to a given rock size. An increase in surface roughness has a larger effect on low angle slopes than on steep ones. As surface roughness increases, velocity generally decreases and bounce height increases (Jones et al., 2000). During rockfall simulation, the maximum allowable variation in slope angle ( $\theta_{max}$ ) is calculated for each cell.

$$\theta_{max} = \tan^{-1}\left(\frac{S}{R}\right)$$

where  $\theta_{max}$  is the maximal allowable variation in slope angle (deg),  $S$  is surface roughness (m) and  $R$  is rock radius (m).

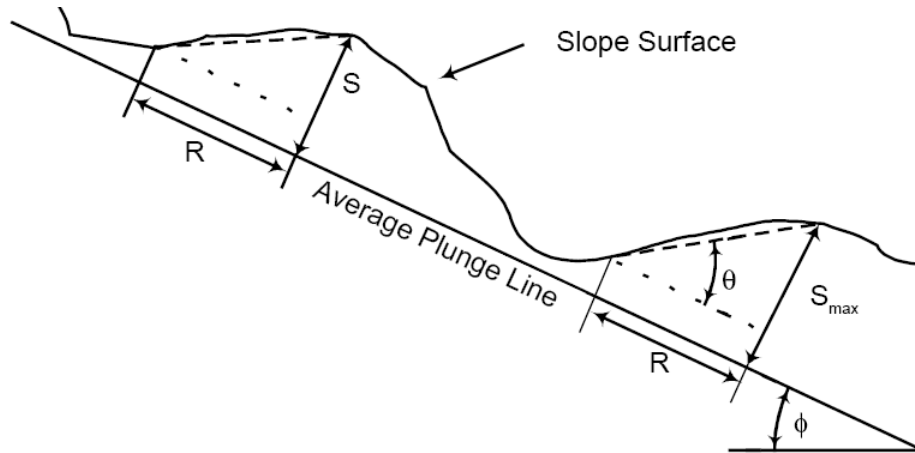


**Figure 2-5.** Surface roughness ( $S$ ) measured as the perpendicular variation from average plunge line ( $\Phi$  slope angle) over a distance of a rock radius ( $R$ ). Maximum slope variation ( $\theta_{max}$ ) is defined by  $S$  and  $R$ , Slope angle varies between  $0$  and  $\theta_{max}$  (after Jones et al., 2000).

### 2.3.2.2 Slope Material Properties

The mechanics of the impact of the rock with slope surface are simulated using two mechanical coefficients which affect the rebounding of the block. These are represented by numerical values referred as **normal coefficient** of restitution ( $R_n$ ) and **tangential coefficient** of frictional resistance ( $R_t$ ) where the normal direction is perpendicular to the slope surface, and the tangential direction is parallel to the slope surface (**Figure 2-6**). When a rock bounces on a slope, kinetic energy is lost due to inelastic components of the collision and friction.  $R_n$  is a measure of the degree of elasticity in a collision normal to the slope, and  $R_t$  is a measure of frictional resistance to movement parallel to the slope.

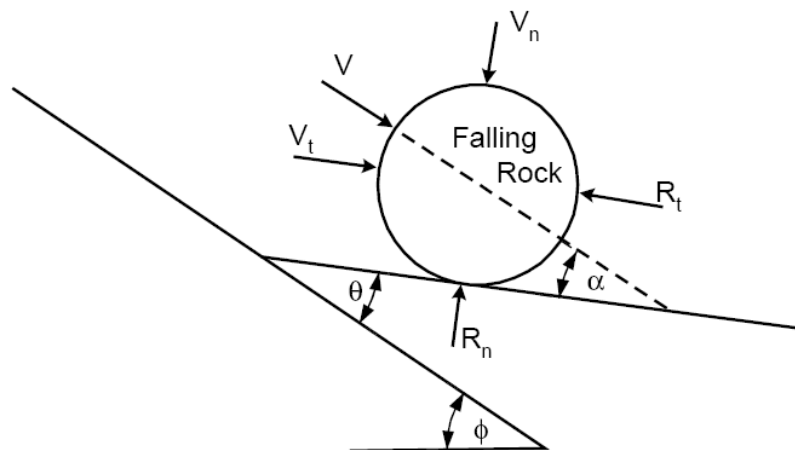


**Figure 2-6.** Impact angle ( $\alpha$ ) defined as a function of rock trajectory, slope angle ( $\Phi$ ), and slope variation ( $\theta$ ). Rock velocity ( $V$ ) is decomposed into normal ( $V_n$ ) and tangential ( $V_t$ ) components. The tangential coefficient of frictional resistance ( $R_t$ ) and the normal coefficient of restitution ( $R_n$ ) act to decrease the falling rock's velocity (after Jones et al., 2000).

For steep slopes where the number of impacts is low, the effect of the material coefficients will be negligible. For low angle slopes the effect of coefficients is the largest. Jones et al. (2000) suggest that changes in the coefficients within reasonable limits for a specific slope will not

produce significant changes in the results. The effect of slope angle and surface roughness is much greater than the effect of the coefficients. **Table 2-1** Lists the CRSP suggested tangential coefficient values for different slope materials (Jones et al., 2000).

TABLE 2-1 Suggested Tangential Coefficient Input Values (Jones et al., 2000)	
Slope Description	Tangential Coefficient ( $R_t$ )
Smooth Hard Surfaces and Paving	0.90 – 1.0
Most Bedrock and Boulder Fields	0.75 – 0.95
Talus and Firm Soil Slopes	0.65 – 0.95
Soft Soil Slopes*	0.50 – 0.80

\* Soft soil slopes values were extrapolated from other soil types due to lack of data.

Rockfall simulation output is less sensitive to changes in the tangential coefficient ( $R_t$ ) than to changes in the normal coefficient ( $R_n$ ). It also suggests that the changes in the tangential coefficient  $R_t$  are of more significance for hard or heavily vegetated slopes (Jones et al., 2000).

Another major influence on the loss of kinetic energy tangential to the slope is the velocity normal to the slope. An increase in velocity normal to the surface results in a greater normal force during impact. The energy lost during the bounce is determined, among other factors, from the velocity normal to the slope which is calculated based on the **normal coefficient** ( $R_n$ ). **Table 2-2** lists CRSP suggested normal coefficient values for different slope materials (Jones et al., 2000). Detailed equations regarding the influence of the material coefficients on the behavior of rockfall are presented in Jones et al. (2000).

TABLE 2-2 Suggested Normal Coefficient Input Values (Jones et al., 2000)	
Slope Description	Normal Coefficient ( $R_n$ )
Smooth Hard Surfaces and Paving	0.60 – 1.0
Most Bedrock and Boulder Fields	0.15 – 0.30
Talus and Firm Soil Slopes	0.12 – 0.20
Soft Soil Slopes*	0.10 – 0.20

\* Soft soil slopes values were extrapolated from other soil types due to lack of data.

### 2.3.2.3 Rock Geometry

Rock geometry is defined by rock size and rock shape. Since a larger rock has greater momentum and is less likely to lodge among irregularities, it will travel farther down a slope than a smaller rock (Ritchie, 1963). **Rock size** is thus critical in determining the degree to which surface roughness will affect rockfall behavior (the larger the rock the larger the surface irregularities required to affect it). Rock size is therefore another factor in determination of surface roughness. **Rock shape** contributes to randomness of rockfall and influences the portions of translational



and rotational energy through the moment of inertia; in CRSP it is restricted to three basic geometric shapes: sphere, cylinder or disc. Spherical rock shape represents worst-case since it holds the most mass for a given radius (Jones et al., 2000).

#### **2.3.2.4 Rock Material Properties**

Rock material properties are durability and rock mass. Durability determines whether a rock will break apart upon impact. Two factors act to reduce the influence of rock durability and rock mass on a rockfall: a. their consistency minimizes their effect on the variability of the rock's behavior; b. their variation among rocks is considerably less than among slopes or even within a given slope. Thus the influence of any variability of rock durability or rock mass is negligible compared to other parameters in the rockfall model.

**Rock density** varies with rock type. Hoek and Bray (1981) suggest typical rock densities for hard sedimentary rocks (limestone, dolomite, sandstone) to be 2340 to 2850 kg/m<sup>3</sup>. In this study, all blocks (limestone) were given density of 2500 kg/m<sup>3</sup>.

#### **2.3.2.5 Starting Zone and Starting Velocity**

The starting zone is the rockfall source zone and is defined as a range in the Y (elevation) coordinates from its top to its base. Starting velocity is comprised of initial horizontal and vertical components assigned to the rocks. These components are acted upon by gravitational acceleration until the rock's trajectory intersects the slope, where it is assigned a resultant velocity for its first impact with the slope.

#### **2.3.2.6 Analysis Points**

CRSP allows setting up to three analysis points along the studied slope profile. For each analysis point, CRSP provides analyses of the following details:

1. Number of rock-blocks passed through the analysis point.
2. The maximum, average, minimum, and standard deviation of rock velocities.
3. The maximum, average, geometric mean, and standard deviation of rock bounce heights (not used in this study since the authors of the program state that bounce height analysis is not very reliable (Jones et al., 2000)).
4. The maximum, average, and standard deviation of kinetic energies.
5. Cumulative probabilities of velocity, kinetic energy, and bounce height.
6. Graphs of the distribution of rock velocities and bounce heights.

### **2.3.3 CRSP Program Assumptions**

Using the CRSP model for rockfall, the assumptions and constraints stated by the authors of the program, are hereby brought as elaborated in the manual (Jones et al., 2000).

On a natural slope, the parameters will have a wide range of values and would be cumbersome to analyze as independent variables. CRSP reduces the number of variables by means of the following simplifying assumptions:

1. *The slope profile should follow the most probable rockfall path as established during field investigations. Therefore, all calculations may be in 2-D.*
2. *Because the rock type does not change during a rockfall and the range of slope material properties is much greater than that of rock material properties, coefficients assigned to the slope material ( $R_n$  and  $R_t$ ) can account for both the rock and slope properties.*
3. *The worst case scenario is generally that of the largest rock that remains intact while traveling down a slope. Therefore, it is assumed that the rock does not break apart in its fall.*
4. *Rock size and shape are assumed constant for analysis of rockfall from a given source. Values assigned to these parameters are determined by field study of the source area and slope materials.*
5. *For determination of a rock's volume and inertia, a sphere may be used because it yields a maximum volume for a given radius, which will tend toward a worst case scenario analysis.*

### 2.3.4 CRSP Algorithm for Rockfall Simulation

Rockfall simulation begins within a selected vertical zone representing the source location by assigning a rock initial horizontal and vertical velocity components. The velocity components are acted upon by gravitational acceleration until the rock's trajectory intersects the slope below at resultant velocity  $V_I$ , which is reduced to two components: velocity normal to the slope surface  $V_{nI}$  and velocity tangential to the slope surface  $V_{tI}$  (**Figure 2-6**). At the point of impact, the slope angle ( $\Phi$ ) is randomly varied up to the limit of the maximum probable variation in the slope ( $\Phi_{max}$ ). At each impact, the incoming velocity, impact angle, and rotational velocity are used along with the input parameters to calculate new velocity components and rate of rotation. After each bounce, CRSP performs an iteration to find the time elapsed until the next bounce. Elapsed time is calculated from X and Y velocity-components, gravitational acceleration, and the slope profile. After a new impact position is established, the next bounce is calculated. If the distance the rock travels between bounces is less than its radius, it is considered to be rolling and is given a new (X, Y) position equal to a distance of one radius from its previous position. This models a rolling rock as a series of short bounces (Jones et al., 2000). When the impact resultant velocity is reduced to zero the block stops.

The output of CRSP is a text file containing the simulation analysis. Data relevant to this study was extracted as follows: a. rock weight calculated from input rock dimensions; b. for each slope cell: maximal velocity and kinetic energy; c. for each of the 3 analysis points: cumulative probability statistics of velocity and kinetic energy; number of rocks passed through the analysis point; d. travel distances (number of blocks stopped per 10 m slope interval). ❖

## Chapter 3

### Results

#### 3.1 Source, Blocks and Triggering Mechanism Properties

**T**his section details the joint sets of the source of rockfalls and the results of the OSL age determination aimed to answer for the triggering mechanism of rockfalls from the Ein-El-Assad Formation.

##### 3.1.1 Source Rock Joint Sets

Joint sets were measured in the field (location coordinates: E252325/N789515 ITM) performing 3 scan lines at the top of Ein-El-Assad Formation (**Figure 3-1**), using a measuring tape and a *BRUNTON* compass for joint dip measurements.



**Figure 3-1.** Location of scan lines at top of the Ein-El-Assad Formation.

The analysis of scan lines yielded 3 joint sets excluding the bedding (which is referred to as *J1* and was not accounted for). *Joint set 2 (J2)*: 4 joints over 12.5 m with mean joint spacing of ~3.1 m measured along E–W striking scan line. *Joint set 3 (J3)* 7 joints over 7.3 m with mean joint spacing of ~1.1 m and 9 joints over 7.2 m with joint spacing of ~ 0.9 m along a N–S striking and NNW-striking scan lines, respectively. *Joint set 4 (J4)* consists of only one joint over 7 m along 305° striking scan line. Schematic representation of joint set orientations are plotted in **Figure 3-2** and detailed in **Table 3-1**.

TABLE 3-1 Scan-line Joint Spacing			
Joint Set	Joints/m	Mean Spacing	Spacing Range
J1 (bedding)*	-	-	-
J2	0.32	3.1 m	2.3 – 6.3 m
J3	0.93	1.0 m	0.3 – 2.9 m
J4 **	?	?	?

\* bedding joint spacing was not measured

\*\* J4: only 1 joint along scan-line – no spacing data available

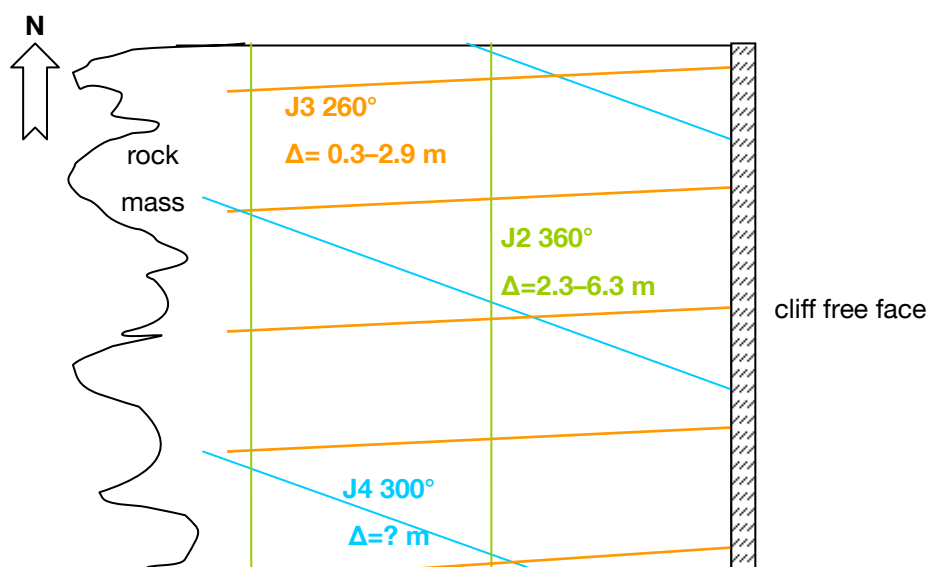


**Figure 3-2.** Schematic representation (map view) of joint sets of the Ein-El-Assad Formation measured at top of the outcrop. J1 is bedding and was not measured; J2 has a mean spacing of ~3.1 m, J3 has a mean of 1.0 m and J4 spacing data is unknown.

A rough estimation of the block sizes, which are defined by these joint sets, may be obtained under these assumptions and constraints: a. J4 has little effect on block size since it has larger spacing than J2 and J3. Therefore, blocks are constrained by the latter two joint sets and the bedding J1; b. Because quasi-rectangle fallen blocks were observed on the slope, J1 (bedding) may have a spacing range similar to those of J2 and J3, e.g. 0.3 – 6.3 m. the product  $J1 * J2 * J3$  is an estimation of block volume. Smallest values ( $J1 \approx J3$ ) yield  $2.3 * 0.3 * 0.3 = 0.2 \text{ m}^3$ , while largest values ( $J1 \approx J2$ ) yield  $6.3 * 2.9 * 6.3 = 115 \text{ m}^3$ . These values are in good agreement with direct field measurements, having blocks of volumes up to  $125 \text{ m}^3$ .

Further analysis of the source joint sets was dismissed due to the assumption that de-facto block volume distribution observations are already available from the rockfall talus and blocks further down-slope, where block volumes may be obtained directly from field rockfall evidence rather than theoretically calculated from potential rock mass jointing.

### 3.1.2 Rockfall Origin Locations

The large rockfall talus evident in the study area and the mapping area where block statistics data were collected are located just below a negative bottle shaped space ('ghost') in the Ein-El-Assad outcrop mass (**Figure 3-3**) which seems like a possible source for the rockfall talus. It is also in very close proximity to a normal fault traversing the outcrop striking west-southwest (all fault data after Sneh and Weinberger, 2003). This leads to suggest that where rockfall potential source mass is traversed by faults it is susceptible to long-term deformation and fracturing, which contribute to the development of mature rockfall conditions (intense fracturing, less consolidated rock mass). These locations are more susceptible to triggering of rockfalls. The map in **Figure 3-4** outlines such potential locations for rockfall trajectory origins.



**Figure 3-3.** Overview of the study area facing west towards the Ein-El-Assad outcrop. The rockfall talus in front. A normal fault at the rock mass can be observed on the top-right (yellow arrow): the overriding block on the right (north) is lower than the block to the left (south). A scar (yellow ellipse) in the outcrop, possibly the origin of rockfall mass, is clearly visible left (south) to the fault location. This location is marked in an orange arrow in the next figure.



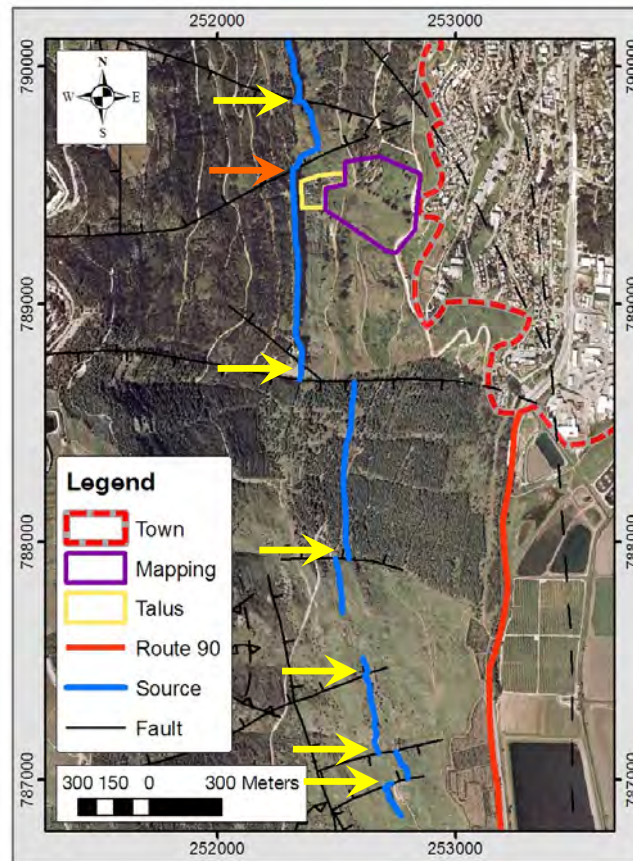


**Figure 3-4.** Location of traversing faults. Source rock mass is subject to fracturing and deformation where faults traverse it. These locations (yellow arrows) may be more subject to triggering of rockfall. Note that the studied talus (yellow) and mapping are (purple) where hundreds of fallen blocks are evident, are located just below a point at the source outcrop traversed by a fault (orange arrow; see previous figure). Faults detailed after Sneh and Weinberger (2003).

### 3.1.3 Block Volume Probability Density Function (PDF)

Block frequency–volume distributions for the observed blocks in the mapping area were based on the rockfall frequency–volume statistics presented in the literature review in **section 1.3.6**. Block volume statistics for the mapping area were performed using 76 blocks (out of 97 in the catalog) larger than 1 m<sup>3</sup>.

For practical reasons, block dimensions were measured in the field as box-shaped (L\*H\*W), yet the rockfall simulation program input is spherical blocks (**section 2.3.2.3**). Block diameter calculation is based on its volume, thus leaving this potential mis-fit on a geometrical shape level only, which is addressed later in **section 3.2.2.4**.

The fitted power-law for the probability density function (PDF; **Figure 3-5**) of the block volumes in the mapping area is

$$p = 0.4V_B^{-1.17}$$

where  $V_B$  is the block volume in m<sup>3</sup>, with  $R^2=0.72$ . Note that the power in that regression conforms to that of global inventories (**Figure 1-19**; **Figure 1-20**).

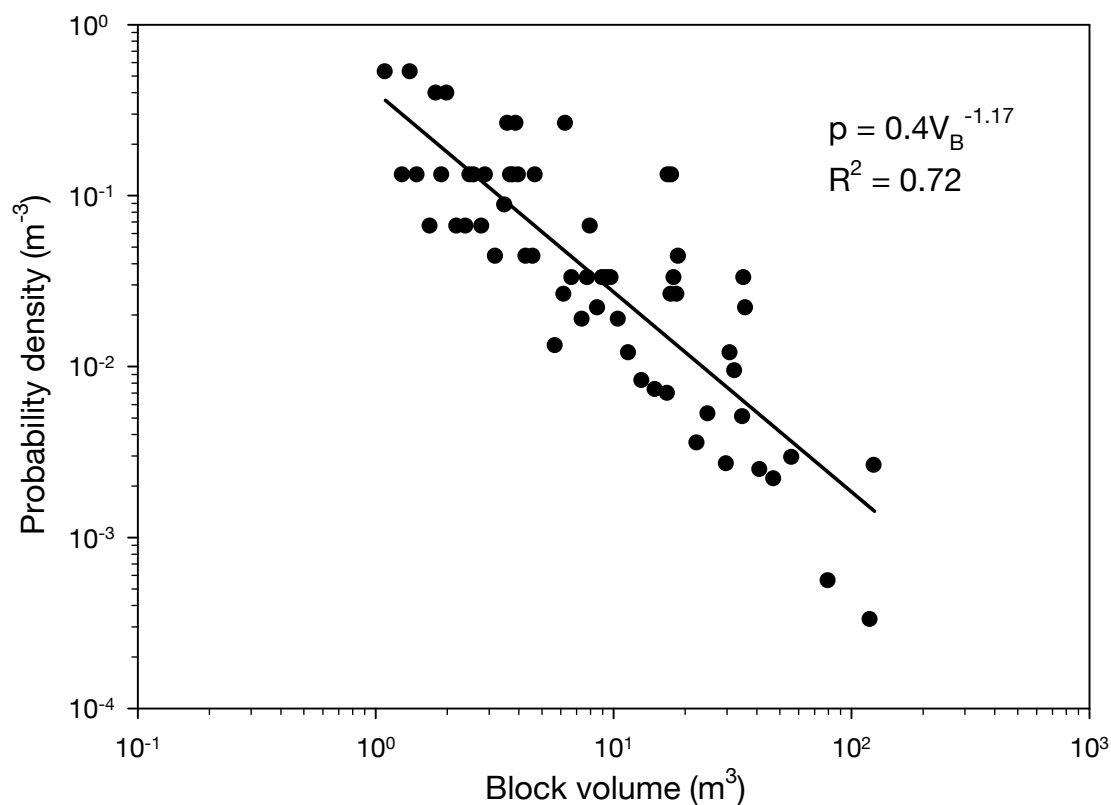


**Figure 3-5.** Probability density function (PDF) of mapped blocks.  $N=76$  blocks ( $D>1\text{ m}^3$ ) measured for volume in the field were given probability density values according to their frequency and volume bin size (section 2.1.3). Plot axes are logarithmic.

### 3.1.4 Block Volume Distribution

The frequencies of block volumes (or corresponding diameters) were calculated from a total of  $N=76$  documented blocks. Cumulative frequencies (i.e. the number of blocks at given volume or smaller) were used to calculate the cumulative probabilities for each block size (**Table 3-2**). Since no data was collected for blocks smaller than  $1\text{ m}^3$  ( $D=1.3\text{ m}$ ) there is neither frequency nor probability available for blocks of that size or smaller.

TABLE 3-2 Block Volume (Diameter) Distribution at Mapping Area			
Volume bin ( $\text{m}^3$ )	Diameter (m)*	Cumulative frequency*	Cumulative Probability**
1 ***	1.3	-	-
10	2.7	50	0.658
50	4.6	71	0.934
100	5.8	74	0.974
125	6.2	76	1

\* Total 76 mapped blocks of volumes 1–125  $\text{m}^3$ ; volumes correspond to given sphere diameters.

\*\* Cumulative frequency of given size or smaller divided by  $N$  (76)

\*\*\* No data collected for blocks smaller than  $1\text{ m}^3$

The probability values per block diameter (**Table 3-2**) were plotted and fitted a regression curve (**Figure 3-6**), from which probability for any given block size may be calculated, and vice-versa. The curve x axis is diameter since the rockfall simulation program (CRSP v4) uses diameter as block size input. Since no data is available for blocks smaller than  $D=1.3$  m, regression was performed on the cumulative frequencies of  $2.7 \leq D \leq 6.2$  m. According to field data, when rockfall occurs, the probability for a block of given diameter or smaller is

$$p = 0.412 \ln(D) + 0.262$$

where  $D$  is the given diameter (with  $R^2=0.97$ ). This may also be used to determine the maximal block diameter which may be encountered considering a given probability

$$D = \exp[(p - 0.262) / 0.412]$$

where  $p$  is the probability one wishes to prepare for. This correlation would come in handy at a later stage, when considering probable rockfall hazard. Since larger blocks pose larger hazard due to higher kinetic energy which increases potential damage, the probabilities for different block sizes may be required when planning rockfall mitigation solutions.

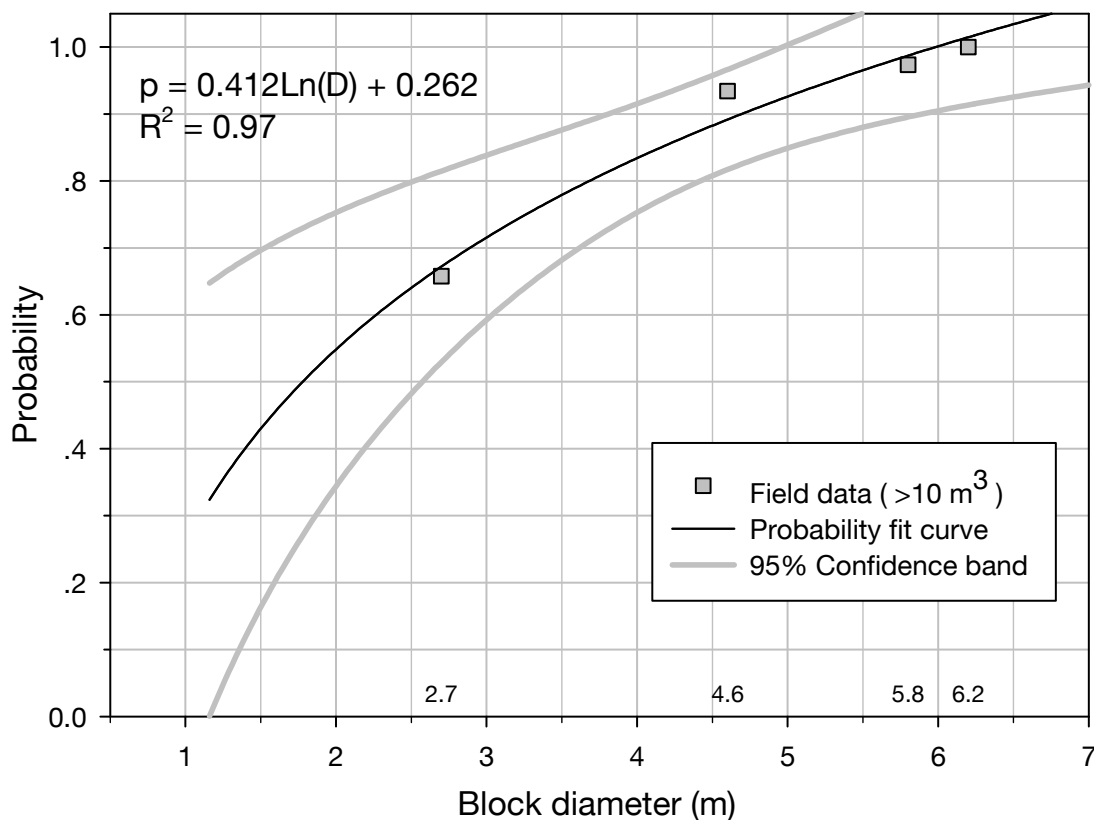


**Figure 3-6.** Cumulative probability for given block diameter. Probability curve is calculated from data of 76 blocks ( $V > 1 \text{ m}^3$ ) documented in the mapping area.

### 3.1.5 Block Estimated Diameters

Following the flow for estimating block diameters (**section 2.1.4**), maximal GIS dimension ( $x$ ) of block volume ( $V$ ) was fitted the power-law  $x = 1.28 * V^{0.35}$  with  $R^2 = 0.92$  (**Figure 3-7**).



Estimated spherical rock diameter ( $D$ ) from maximal GIS dimension ( $x$ ) was fitted a linear regression  $D=0.85x+0.26$  with  $R^2=1$  (Figure 3-8).

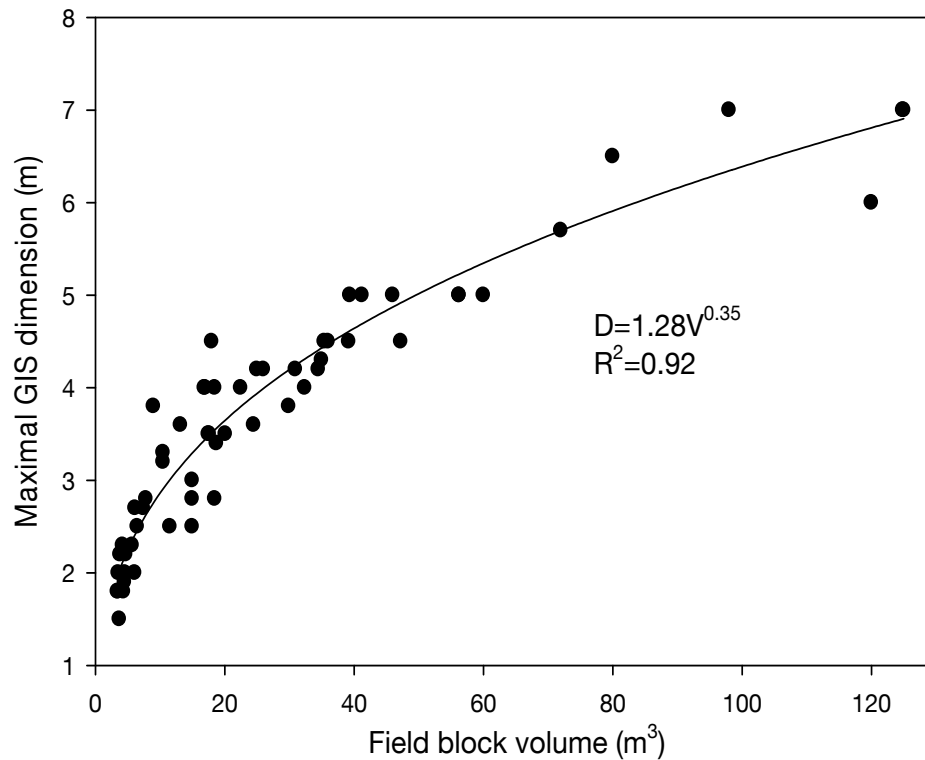


Figure 3-7. Maximal GIS dimension measured for mapped field block volumes.

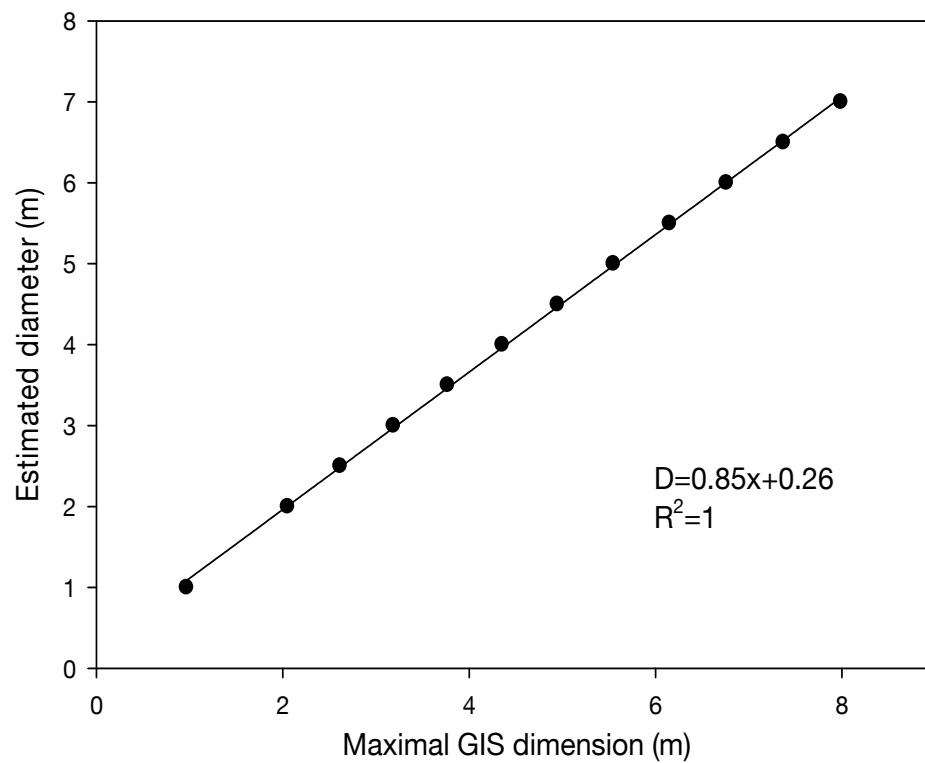
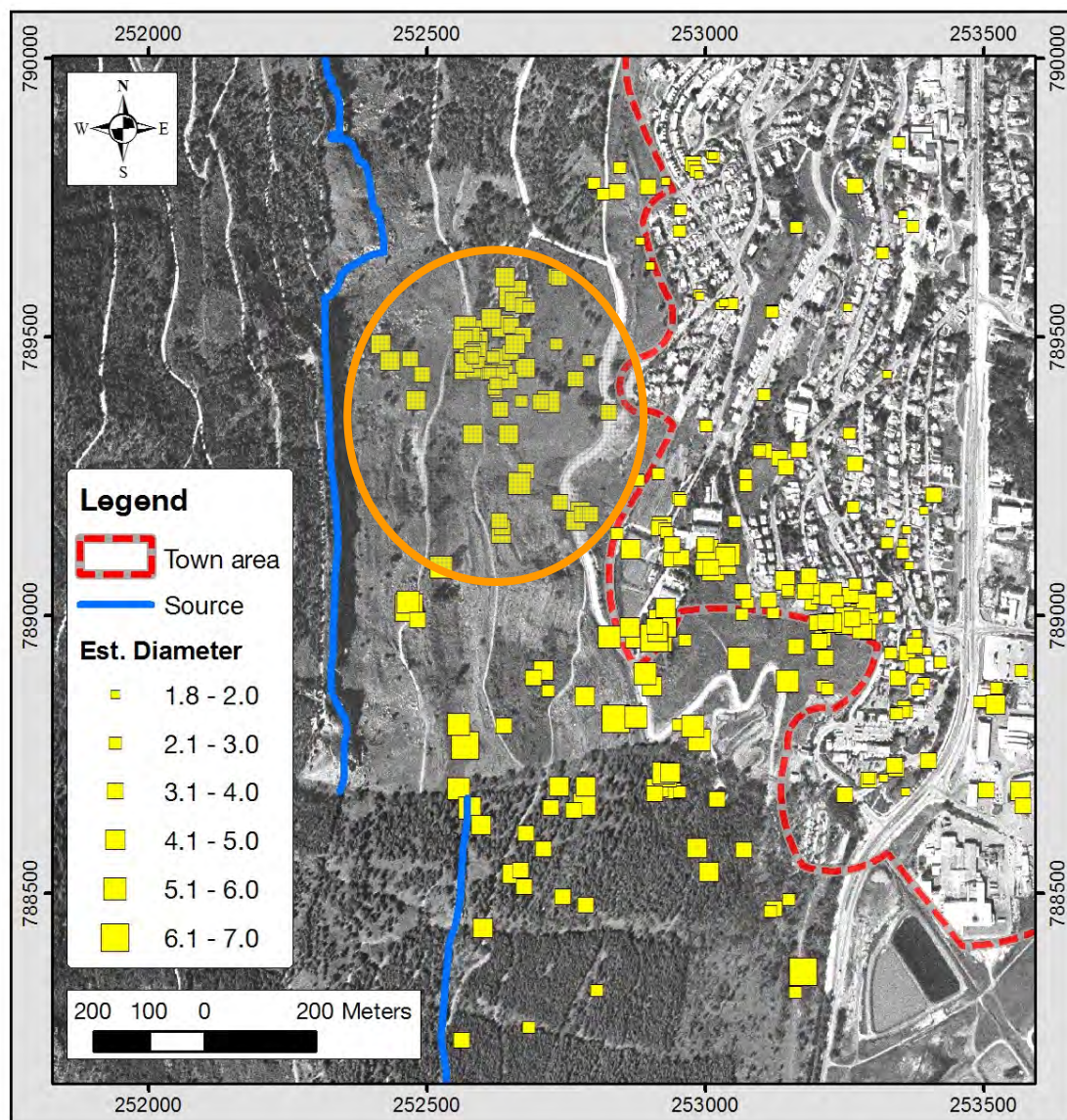


Figure 3-8. Correlating between the maximal GIS dimension of mapped blocks and the corresponding diameter of a spherical block of the same volume. Thus finding a way to estimate the diameters of non-mappable blocks on aerial photos using GIS (see above text for detail).

Estimated diameters assigned to some 200 blocks (**Figure 3-9**) were later used to determine observed maximal travel distances required for the back analysis calibration of CRSP v4. Note that this flow, although statistically and mathematically well-supported, yields an estimation of a *three-dimensional object* (a spherical rock) from *two-dimensional data* (or even one-dimensional, considering the measured entity is the *maximal distance dimension* of a 2-D shape). This leads to suggest that estimated diameters of past existent blocks should be taken with a grain of salt. However, it is required to make these assumptions in order to acquire an efficient local-site calibration of the rockfall simulation model, when aiming for valid rockfall hazard evaluation.



**Figure 3-9.** Estimated diameters of non-mappable blocks (located using 1946-51 aeriels). Blocks in orange ellipse used for the correlation between the sizes of field and non-mappable blocks.

### 3.1.6 Triggering Mechanism of Rockfalls

#### 3.1.6.1 Type of Failure

According to field observations, the possible types of failure of the rock-mass are toppling or failure along tension cracks, since sliding along discontinuities (along bedding dip) is not probable due to the fact that the bedding dips towards the cliff-mass (i.e. opposite to the slope direction; see **Figure 3-10**). Therefore, sliding cannot occur as the rock-mass is considered to have infinite stability against sliding.

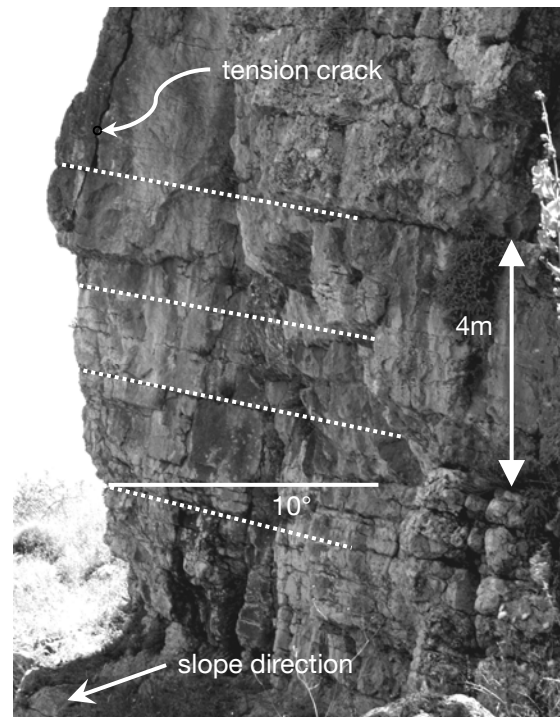


**Figure 3-10.** Anti-slope dips at the base of the source cliff. Bedding (dotted lines) dips toward the cliff mass, eliminating block sliding failure due to infinite stability against sliding in the slope direction.

#### 3.1.6.2 OSL Dating Results

Lab results of 13 samples include OSL ages of 10 samples taken from block–soil interface, one sample taken below block–soil interface and two pit samples (not directly under a block), as detailed in **Table 3-3**. The laboratory report details the following information: Grain size for all samples is 74–125  $\mu\text{m}$ , except for samples QS-1 and QS-2, for which grain size 88–125  $\mu\text{m}$  was used. Water moisture estimated at  $15 \pm 5\%$ . The quartz was etched by concentrated HF for 40 minutes.  $D_e$  was obtained using the single aliquot regeneration (SAR) dose protocol, with preheats of 10 s at 220–260°C and a cutheat 20° below preheat. “No. of discs” is the number from those measured that was used for calculating the  $D_e$  (only a small number of measurements was not used).

TABLE 3-3 Lab Results for OSL Ages of Qiryat-Shemona Samples

Sample ID	Depth (m)	$\gamma$ +cosm ( $\mu\text{Gy/a}$ )	K (%)	U (ppm)	Th (ppm)	Ext. a ( $\mu\text{Gy/a}$ )	Ext. b ( $\mu\text{Gy/a}$ )	Tot. dose ( $\mu\text{Gy/a}$ )	No. of discs	De (Gy)	Age (ka)
QS-1	1.2	945	0.8	1.3	6	7	745	1697 $\pm$ 102	8/10	12 $\pm$ 1.8	7.00 $\pm$ 1.10
QS-2*	1.9	836	0.88	1.9	8.5	10	911	1784 $\pm$ 100	8/9	99 $\pm$ 12	55.70 $\pm$ 7.60
QS-3	0.7	762	1	2	8.4	10	995	1767 $\pm$ 94	6/9	2.7 $\pm$ 0.2	1.50 $\pm$ 0.13
QS-4	0.6	577	1	1.6	6.6	8	910	1495 $\pm$ 77	10/13	1.5 $\pm$ 0.3	0.89 $\pm$ 0.16
QS-5	0.5	744	0.76	1.3	4	6	680	1429 $\pm$ 85	10/13	5.7 $\pm$ 0.9	4.00 $\pm$ 0.70
QS-6	0.4	554	0.46	1.3	4.9	6	520	1080 $\pm$ 64	12/13	2.3 $\pm$ 0.5	2.20 $\pm$ 0.50
QS-7**pit	0.03	536	0.73	1.5	6	7	726	1269 $\pm$ 69	10/13	0.34 $\pm$ 0.10	0.27 $\pm$ 0.08
QS-8**pit	0.3	536	0.73	1.5	6	7	726	1269 $\pm$ 69	9/13	0.89 $\pm$ 0.17	0.71 $\pm$ 0.14
QS-9	0.3	455	0.65	1.6	7.1	8	712	1175 $\pm$ 62	10/13	3.6 $\pm$ 1.4	3.00 $\pm$ 1.20
QS-10***	0.5	569	0.66	1.6	7.3	8	722	1299 $\pm$ 71	10/13	10.6 $\pm$ 2.9	8.20 $\pm$ 2.30
QS-11	0.3	536	0.58	1.7	6.3	8	665	1209 $\pm$ 67	10/12	2.7 $\pm$ 0.9	2.20 $\pm$ 0.70
QS-12	1.2	905	1.08	1.9	9	10	1041	1256 $\pm$ 108	10/13	8.0 $\pm$ 1.7	4.10 $\pm$ 0.90
QS-13	0.4	486	1.05	1.8	8.6	10	1003	1481 $\pm$ 73	12/13	6.8 $\pm$ 3.4	4.60 $\pm$ 2.30

\* Excluded from statistics because of age axis scaling and large absolute time uncertainty range

\*\* Sampled from pit (not under a block) for current near-surface soil OSL results

\*\*\* Excluded from plot and statistics: sampled lower than block-soil interface (30 cm below QS-9)

OSL ages by Naomi Porat, Luminescence dating lab, Geological Survey of Israel

## 3.2 Rockfall Trajectories and Affected Area

Rockfall simulation results are based on 125 simulation runs along 25 profiles, analyzed by CRSP v4 (*Colorado Rockfall Simulation Program*). One simulation run consists of 100 blocks simulated along the profile. Five simulation runs were held per profile – one per given diameter (1.3, 2.7, 4.6, 5.8 and 6.2 m; see **Table 3-4**). This section details the results and analysis of the distribution of travel distances (or stop distances) while relating to different aspects such as slope angle and block volume, velocity and kinetic energy. All are summarized for a rockfall hazard evaluation.

TABLE 3-4 <b>Simulation Block Sizes</b>	
<b>Simulated Diameter (m)</b>	<b>Equivalent Volume (m<sup>3</sup>)</b>
1.3	1
2.7	10
4.6	50
5.8	100
6.2	125

### 3.2.1 Data Collection for this Study

While data collection for most of the input parameters took place in the field, some parameters do not require field work. Yet these are still subject to considerations constrained by the field data. Following is a description of the different CRSP input data elements and how they were obtained in this study.

#### 3.2.1.1 Feasible Trajectories of Falling Rock-Blocks

Trajectories were selected according to simple assumptions detailed in **section 3.2.1.3**. In accordance with the conclusion regarding trajectory origin location (**section 3.1.2**), 10 out of the 25 rockfall simulation profiles used in CRSP had their origins located at close proximity to faults traversing the cliff mass (profiles 5, 6, 8, 9, 19, 21, 25, 26, 28 and 30; **Figure 3-11**). In order to obtain a good resolution for rockfall hazard evaluation to town premises, the spatial density of profiles is much higher (30–100 m intervals) where profiles traverse town border (the northern section of the study area) than at the open areas, where profiles traverse the Route 90 road (150–500 m intervals).



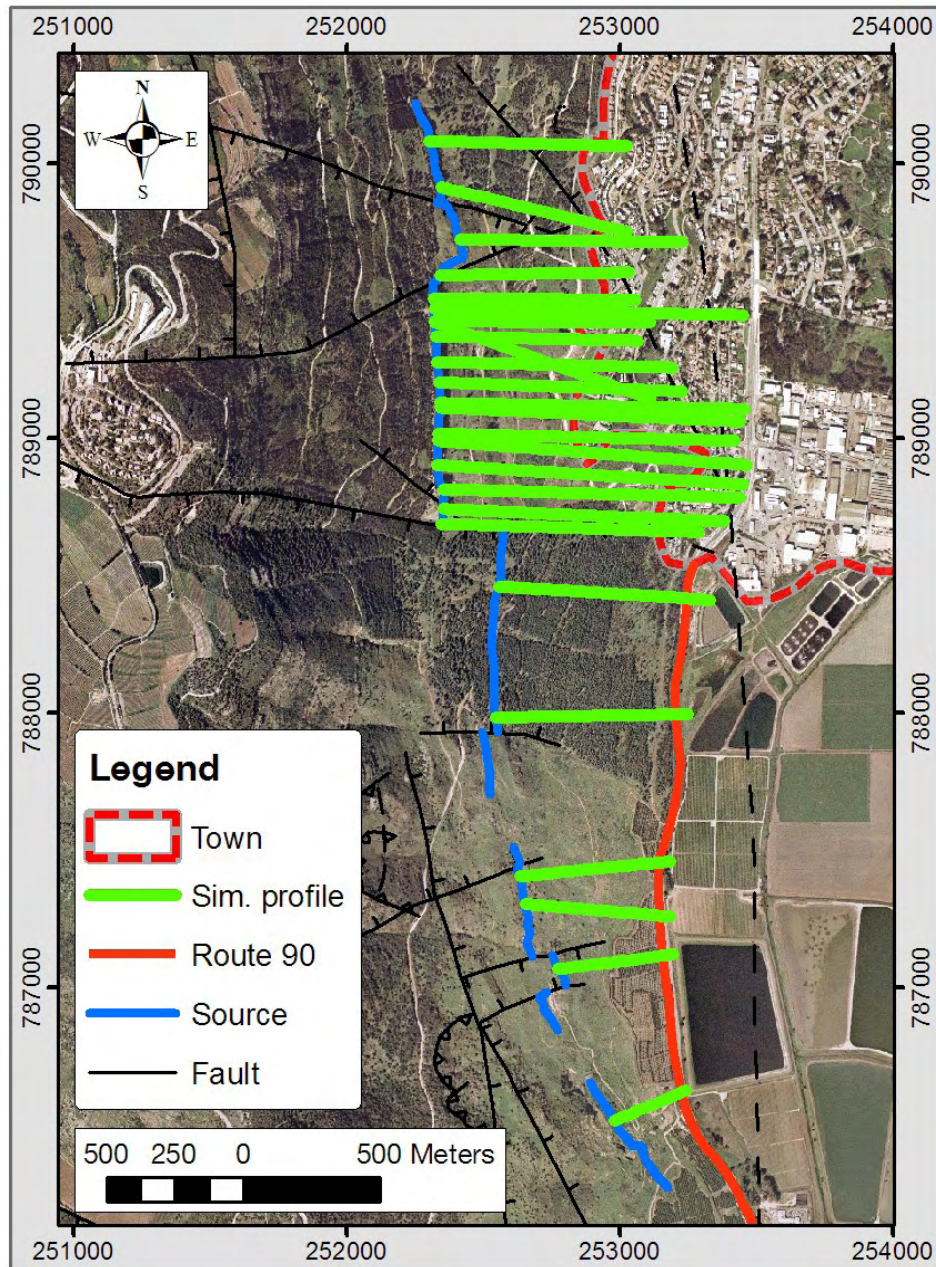


**Figure 3-11.** All 25 rockfall trajectory simulation profiles used with CRSP. 10 profiles originate where faults traverse source cliff. Profiles are denser (30–100 m intervals) where town premises are traversed by profile. Faults detailed after Sneh and Weinberger (2003).

### 3.2.1.2 Slope Profiles

Obtaining slope profile data was performed on GIS. A Field survey to verify the GIS generated section of one profile included dip measurements using a **BRUNTON** compass and a measuring tape in order to get the correct structure of the source escarpment ledge – the Ein-El-Assad Formation. Once validated, the rest of the slope profiles were extracted using a 5 m elevation contour map on the system.

### 3.2.1.3 Rockfall Trajectories for Calibration

Feasible rockfall trajectories were defined according to the following: field mapped rock-blocks found on the slope; mapped blocks from aerial photos dating 1946 and 1951, currently in urban area; surface data from an orthophoto and topographic maps, 3-D analysis of aerial photos using a stereoscope and 3-D GIS analysis.

A few assumptions were made in the selection of potential rockfall trajectories, in order to maintain simplicity and obey basic physics:

1. Trajectories are straight lines originating at the source.
2. Trajectories trend generally in the slope dip direction (deviations from slope dip may apply according to morphological settings which allow it).
3. Trajectories do not traverse stream paths since a falling block will not climb up from a stream (which is the lowest point in its vicinity) to higher grounds.
4. Trajectories pass through mapped concentrations of fallen rocks.

In order to follow these rules, a set of maps for the study area was prepared in GIS, including stream paths, topographic maps, an orthophoto, a DTM, rockfall debris as observed in the field or extracted from historic aerial photos. A 3-D presentation of the GIS data was also used to suggest possible rockfall trajectories.

### 3.2.1.4 Surface Roughness (S)

Surface roughness is measured in the field by stretching a measuring tape down the slope and measuring the perpendicular distance between the tape and the slope. Within each slope distance of one-rock radius  $R$ , the greatest measurement that occurs **several times** is the surface roughness  $S$  (Jones et al., 2000). The change in surface roughness for different rock size is illustrated in *Figure 3-12*.

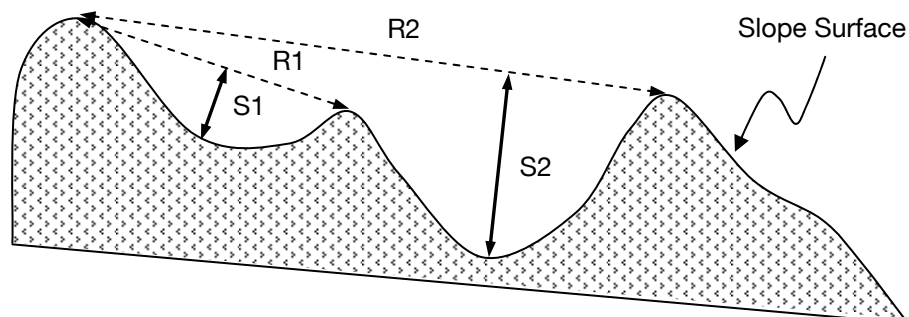


**Figure 3-12.** Measured surface roughness ( $S$ ). Rock radius  $R1$  (dashed line) yields surface roughness  $S1$ ; Greater rock radius  $R2$  (dashed line) yields greater surface roughness  $S2$ . For each rock size, the greatest measurement  $S_i$  which occurs several times along the slope is the surface roughness.

Surface roughness was measured for rock diameters between 1–8 m (the largest, very rare, diameter observed within the study area is about 7 m). Measurements for rock radii from 0.5–4.0 m are detailed in **Table 3-5**. A number of measurements ( $S_i$ ) were performed using a measuring tape for each rock radius on a few places along the slope. The maximal value of all given radius measurements ( $S_{max}$ ) is considered its surface roughness ( $S$ ).

TABLE 3-5 <b>Surface Roughness Field Measurements for Different Rock Radii</b>					
All Values are in Meters (m)					
<b>Radius (m)</b>	<b>S1</b>	<b>S2</b>	<b>S3</b>	<b>S4</b>	<b>S = S<sub>max</sub></b>
0.5	0.04	0.04	0.04	0.03	0.04
1.0	0.13	0.2	0.07	0.11	0.20
2.0	0.14	0.35	0.4	0.15	0.40
3.0	0.15	0.56	0.38	0.3	0.56
4.0	0.26	0.43	0.58	0.56	0.58

\* Each table value is observed with some frequency along the slope over a distance of a few rock radii. For each rock radius, the maximal value of all measurements ( $S_{max}$ ) is considered the surface roughness ( $S$ ).





*Figure 3-13. Slope with abundant blocks.*



*Figure 3-14. Slope with scarce blocks (talus seen at the far right-hand side).*

As surface roughness varies with block radius, determination of  $S$  for all simulated block diameters was performed by fitting a logarithmic regression curve to the surface roughness values measured in the field (*Figure 3-15*).

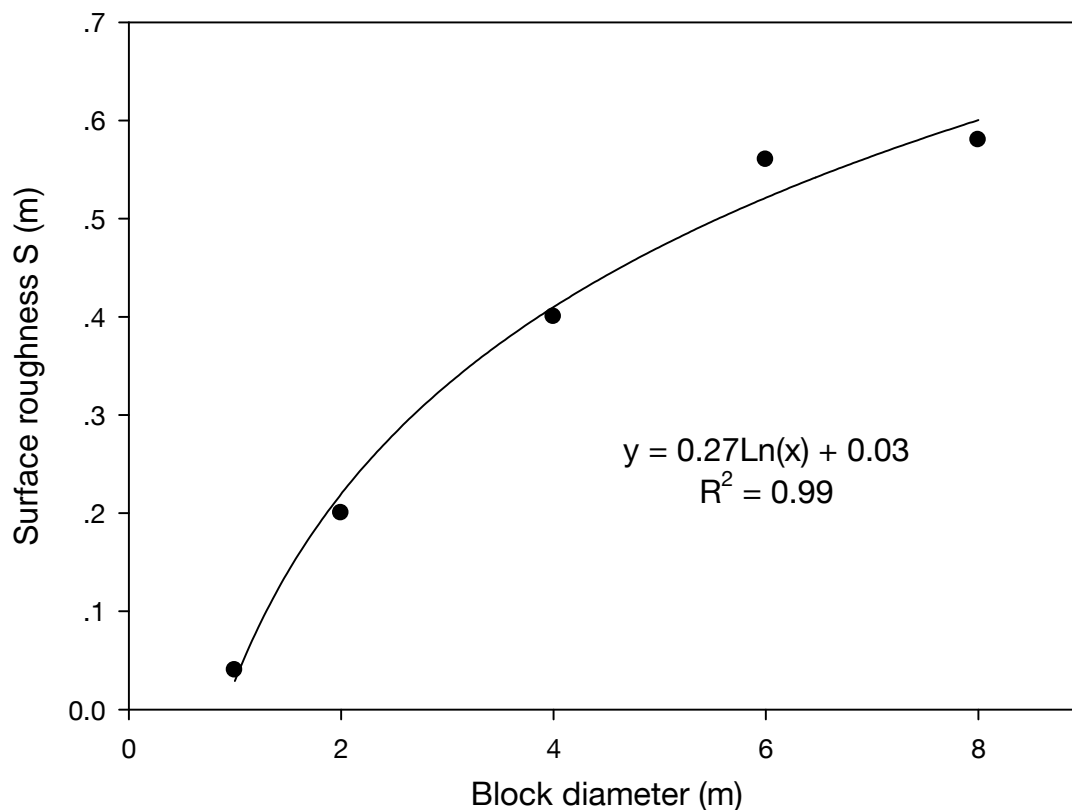


**Figure 3-15.** Dependence of surface roughness on the block diameter. Logarithmic regression is best-fit for all surface roughness values measured in the field ( $D=1-8$  m); regression equation used later to determine surface roughness for all simulated block diameters.

Surface roughness values depending on block size (based on a volume scale and converted to diameters since CRSP block size input is diameter), are detailed in **Table 3-6**. These values were later used for all rockfall simulation runs.

Block Volume (m <sup>3</sup> )	Block Diameter (m)	Calculated S
1	1.3	0.1
10	2.7	0.3
50	4.6	0.4
100	5.8	0.5
125	6.2	0.5

### 3.2.2 CRSP Calibration for this Study

As a first step in performing the hazard analysis, we used the computer program for a back analysis of known rockfall observations to estimate the input parameters of the analyzed area. In this study, calibration of the program was performed along 4 slope profiles (**Figure 3-16**). Each calibration run was held simulating 100 blocks.



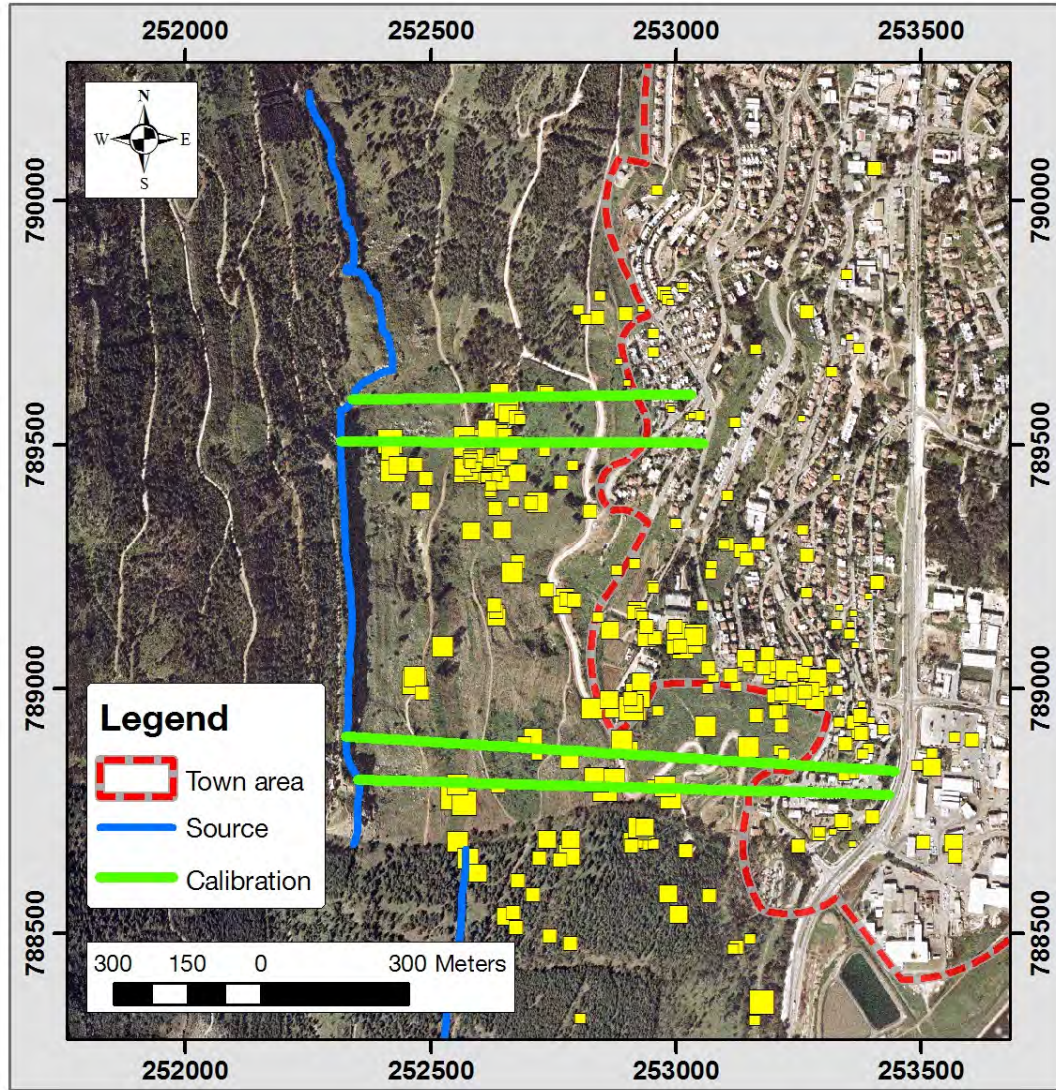


**Figure 3-16.** CRSP Calibration profiles. Town border in red; source in blue; profiles in green; mapped blocks from field and aerial photos in yellow rectangles (size proportioned to block diameter).

### 3.2.2.1 The Delta Max Distance Index

In order to validate the calibration of the model, an ‘index’ which defines the extent to which the modeled simulation is similar to the field and aerial photos observations was defined: the stopping location of the simulated blocks can be compared to the observed one (**Figure 3-17**). The index named *Delta Max Distance* ( $\Delta MD$ ) is the subtraction of the *field-observed* down-slope maximal travel distance from the *simulated* maximal travel distance (in meters)

$$\Delta MD = MD_{sim} - MD_{obs}$$

where  $\Delta MD$  is the delta max distance (m);  $MD_{sim}$  is the maximal simulated travel distance (where all 100 simulated blocks come to a stop);  $MD_{obs}$  is the maximal field observed travel distance (m).

When  $\Delta MD \approx 0$  the simulation model repeats the field-observations and the model parameters may be considered calibrated.  $\Delta MD$  is negative when the simulation undershoots and positive

when the simulation overshoots. The determination of the observed maximal distance ( $MD_{obs}$ ) was based on field block locations and aerial photos from 1946 and 1951, since some parts of the slope are on currently built town premises where no rockfalls are evident on site.

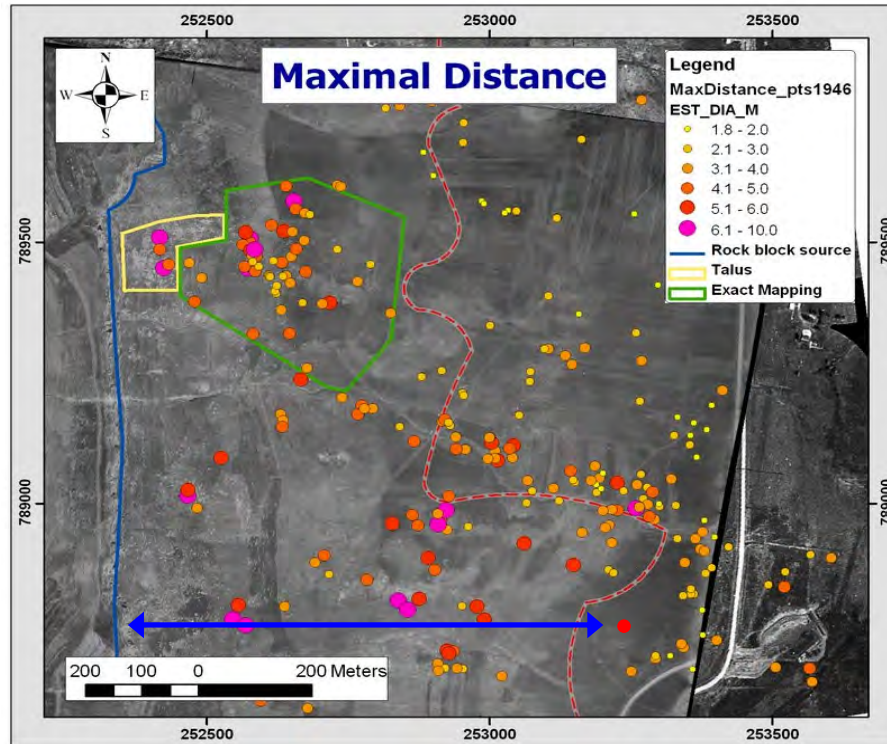


**Figure 3-17.** Measuring observed maximal distance ( $MD_{obs}$ ). Distance for the relevant rock diameter measured in GIS (blue arrow). Colored circles on right map indicate observed rockfall blocks of different diameters; blue line is the rock block source; red dashed line indicates the town border in 2008; talus in yellow; mapping area in green. Background image is the 1946 aerial photo.

### 3.2.2.2 Preliminary Calibration Stage

Eighty preliminary simulation runs (each with 100 analyzed rock blocks) along the four profiles were performed using: a. block diameters of 5–7 m; surface roughness ( $S$ ) of 0.5–0.6 (as measured from field according to block size); b. tangential coefficient ( $R_t$ ) of 0.7–0.9 (0.05 intervals); normal coefficient ( $R_n$ ) of 0.12–0.30 (0.01–0.02 intervals, since this coefficient has greater affect on simulation results). Target  $\Delta MD$  values were set to  $\pm 60$  m (about 10% of profile). These simulations resulted in the following coefficient value ranges:  $R_n=0.2$ –0.25;  $R_t=0.7$ –0.8. These values were later revised and refined following the initial velocity sensitivity analysis (detailed below) and a revision in the technique of slope profile extraction in GIS (yielding better accuracy of the slope topographic section).

### 3.2.2.3 Sensitivity Analysis to Initial Velocity

An earthquake induces ground acceleration on the blocks. The PGA (Peak Ground Acceleration according to the Israeli standard building code 413) value for Qiryat-Shemona Mountains is 0.26 g (**section 1.2.2**). Earthquakes introduce a range of wave frequencies  $\sim 1$ –10 Hz (Scholz, 2002). The higher frequencies attenuate on shorter distances from the source. The use of 1 Hz

frequency denotes a more distant epicenter, but it yields a higher initial velocity ( $v = a/f$ ), so it may be used for velocity sensitivity analysis. Hence, considering 0.3 g horizontal acceleration and assuming 1 Hz earthquake frequency (for highest velocities), the required initial horizontal velocity can be calculated

$$v = a / f$$

where  $a=0.3$  g ( $3 \text{ m/s}^2$ ) and  $f=1$  Hz, so we get  $v = 3 \text{ m/s}$ .

Sensitivity analysis was performed for two initial horizontal velocities ( $V_x$ ): 0 m/s and 3 m/s ( $D=6$  m sphere; same profile and input parameters:  $S=0.5$  m;  $R_t=0.70$ ;  $R_n=0.20$ ). Both yielded similar results for travel distance:  $\Delta MD=-30$  m. This test was repeated twice: a.  $R_n=0.12$  yielded  $\Delta MD=-90$  m for  $V_x=0$  m/s and  $-80$  m for  $V_x=3$  m/s; b.  $R_n=0.25$  yielded  $\Delta MD=+160$  m for  $V_x=0$  m and  $+150$  m for  $V_x=3$  m/s (**Figure 3-18**). An exponential regression curve was fit for  $\Delta MD$  depending on  $R_n$  values ( $V_x=0$  m/s), which yields  $\Delta MD=0$  at  $R_n=0.215$ . Consequently, two conclusions were drawn: a. initial velocity had no significant effect on travel distance; b. the revised (best-fit) normal coefficient is  $R_n=0.22$ .

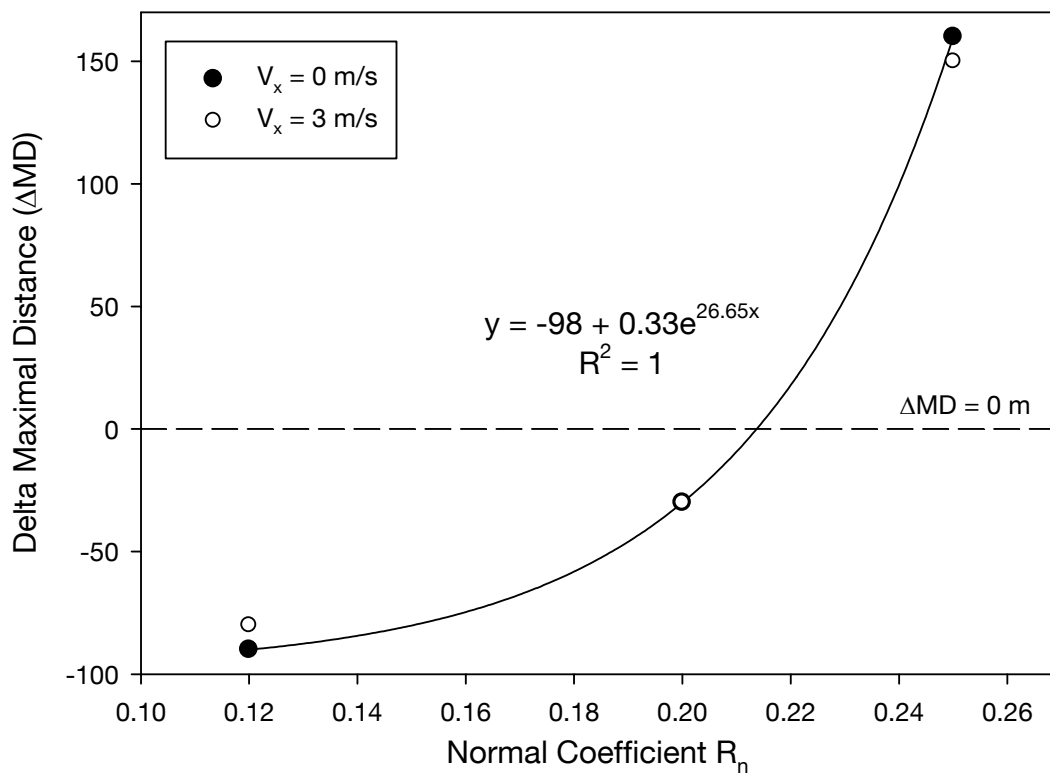


**Figure 3-18.** Sensitivity analysis for initial velocity ( $V_x$ ).  $\Delta MD$  (m) for three  $R_n$  values (0.12; 0.20; 0.25) is plotted per each of two initial velocities: a.  $V_x=0$  m/s (solid circles); b.  $V_x=3$  m/s (hollow circles); zero line ( $\Delta MD=0$  m) is dashed. All other parameters are equal:  $D=6$  m sphere, same profile,  $S=0.5$  m;  $R_t=0.70$ . Exponential regression curve ( $V_x=0$  m/s) fits  $\Delta MD=0$  with  $R_n=0.215$ .

### 3.2.2.4 Rock Shape Sensitivity Analysis

For hazard assessment, spherical rock shape represents the worst-case since it holds the most mass for a given radius and because it rolls more efficiently (Jones et al., 2000). However, this

was not revealed in a sensitivity analysis that was performed for three possible rock shapes of similar weight: a.  $D=6$  m sphere (282,750 kg); b.  $4.5 \times 7$  m cylinder (278,325 kg); c.  $6 \times 4$  m disc (282,750 kg). All were simulated on the same profile with the same input parameters ( $S=0.50$  m;  $R_t=0.7$ ;  $R_n=0.22$ ). Maximal distances were: sphere 590 m; cylinder 570 m; disc 570 m. This 20 m difference is about 3% of the travel distance, which is negligible. In any case, the spherical block shape yields worst-case results (farthest traveling blocks). Velocity profiles are plotted in *Figure 3-19*.

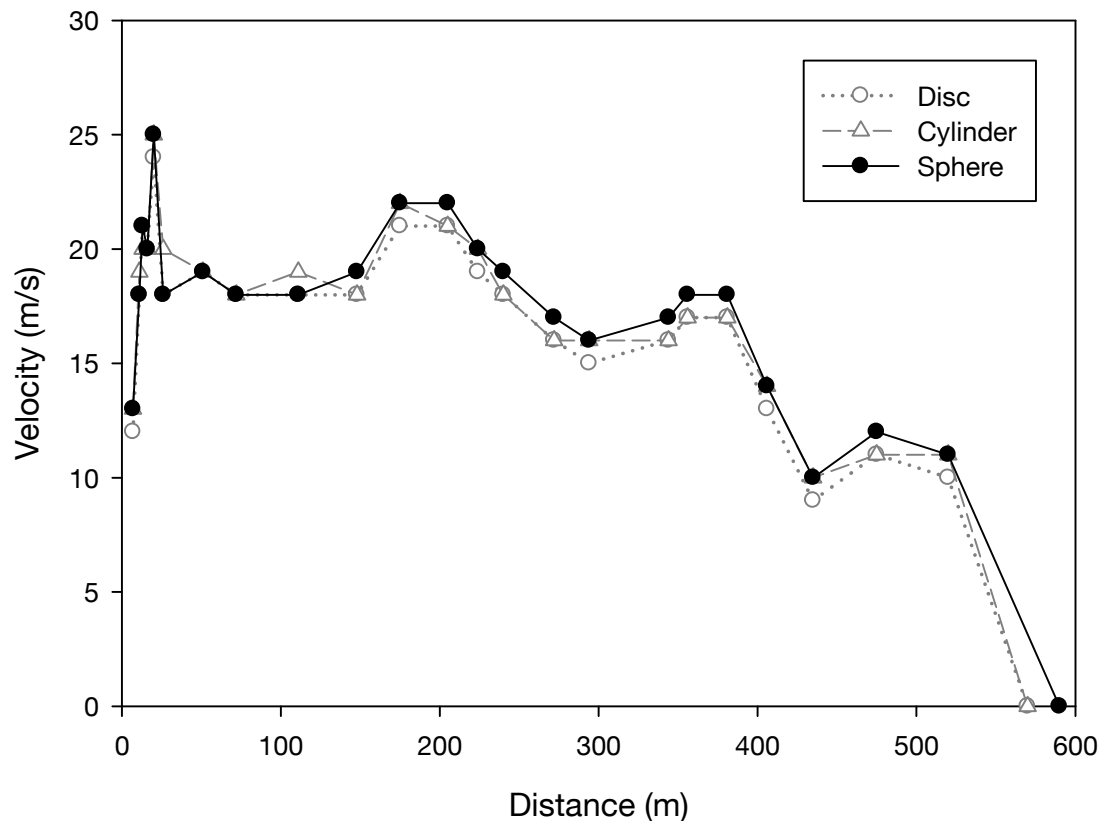


**Figure 3-19.** Sensitivity analysis for rock shape input. Maximal velocities (reported by CRSP) along each slope cell for each rock shape: a.  $D=6$  m sphere (282,750 kg, black circles); b.  $4.5 \times 7$  m cylinder (278,325 kg, gray triangles); c.  $6 \times 4$  m disc (282,750 kg, gray hollow circles). All simulated on same profile with  $S=0.50$  m;  $R_t=0.7$ ;  $R_n=0.22$ . Maximal travel distances: sphere 590 m; cylinder 570 m; disc 570 m.

Velocity profiles of all shapes demonstrate almost identical behavior, where maximal velocity differences among rock shapes are 2 m/s, and in most slope cells are 0-1 m/s. Except for 3 cells at the higher part of the slope, the spherical block demonstrated higher velocities (if any) along all profile.

Thus, it is concluded that considering rock shape, a sphere represents the worst-case in terms of block travel distance and velocity, if such a difference exists.

### 3.2.2.5 Calibration Results

Further simulations run along the four calibration profiles were now performed for all block sizes ( $D=1.3$ – $6.2$  m), using the best-fit coefficient values:  $S=0.1$ – $0.5$  m (according to block



diameter);  $R_t=0.22$ ;  $R_n=0.70$ . All slope cells were given the same values to maintain model simplicity. The fit between observation and simulation is plotted in **Figure 3-20**.

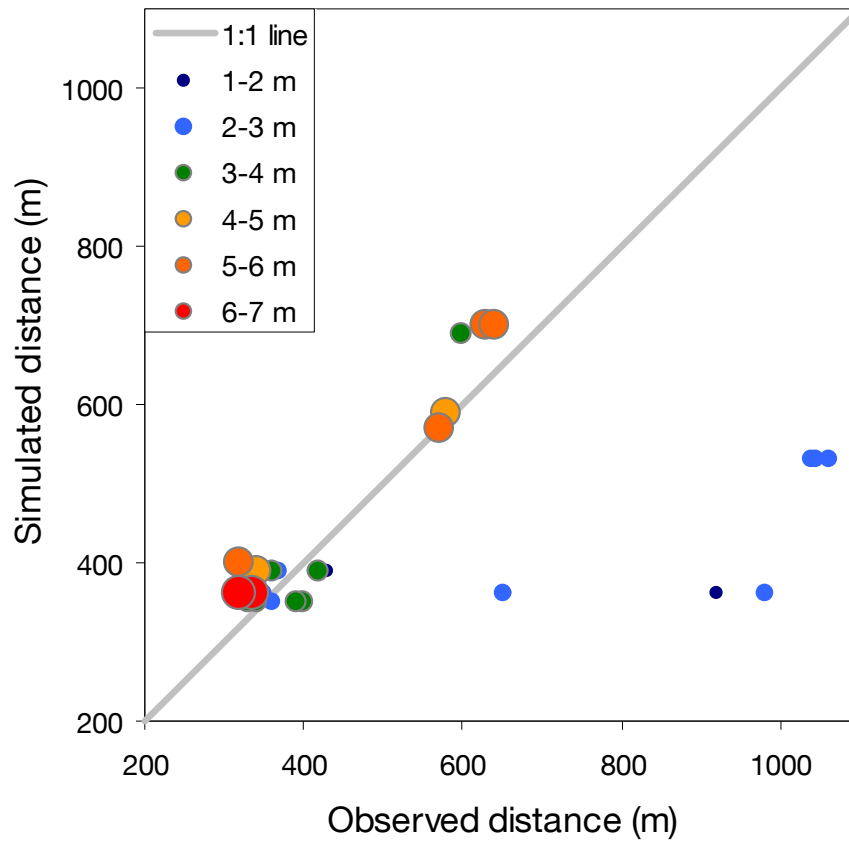


**Figure 3-20.** Simulated (4 calibration profiles) and observed (field and 1946-1951 aerial photos) maximal travel distances. Block diameters are color coded in legend. Middle and large blocks ( $D \geq 3$  m; green, orange, red) demonstrate similar observed and simulated travel distances (close to 1:1 ratio). Small blocks ( $D < 3$  m; blue, light-blue) demonstrate both 1:1 ratio and significantly longer observed travel distances.

Results can be divided into two behavior patterns: 1. *mid-size and large blocks* ( $D \geq 3$  m; green, orange and red circles): the observed and simulated results are close to the 1:1 ratio; for large blocks ( $D \geq 4$  m), simulated travel distance is a little longer, which yields a more conservative result and keeps simulation results on the safe side. 2. *small blocks* ( $D < 3$  m): some blocks are close to the 1:1 ratio, while others demonstrate significantly longer *observed* travel distances.

### 3.2.2.6 Calibration Conclusion

In light of the above discussed, the calibrated CRSP input parameter values were determined as described in **Table 3-7**. These calibrated values are considered the local site fine-tuning of CRSP input parameters required for analysis of rockfall hazard for Qiryat-Shemona.

TABLE 3-7 Calibration Results for CRSP Input Parameters	
Input Parameter	Calibrated Value Ranges
Surface Roughness $S$ (m)	0.1 – 0.5 m (block size dependant)
Tangential Coefficient $R_t$	0.70
Normal Coefficient $R_n$	0.22

An important conclusion from the initial velocity sensitivity analysis is that ground acceleration has no significant implication on the travel distance of the rockfall blocks. This may lead to suggest that the main effect of earthquakes in our case-study might be merely the triggering of the rockfalls.

### 3.2.3 CRSP Simulation Travel Distances

CRSP v4 simulations' block travel distances, detailed in *Table 3-9*, were analyzed to compile the rockfall hazard maps and other hazard properties as detailed below.

### 3.2.4 Rockfall Hazard Area Map

Rockfall hazard map for Qiryat-Shemona is presented in *Figure 3-21*. The map details the entire area subject to rockfall hazard, from source escarpment to the west (Ein-El-Assad Formation) to the stop-line of 100% of blocks. The hazard map was compiled from maximal travel distance (100% of blocks stop line) of the largest blocks ( $d=5.8\text{--}6.2$  m,  $V=100\text{--}125$  m<sup>3</sup>) from 25 rockfall simulation profiles performed using CRSP v4 (detailed in *Table 3-9*).



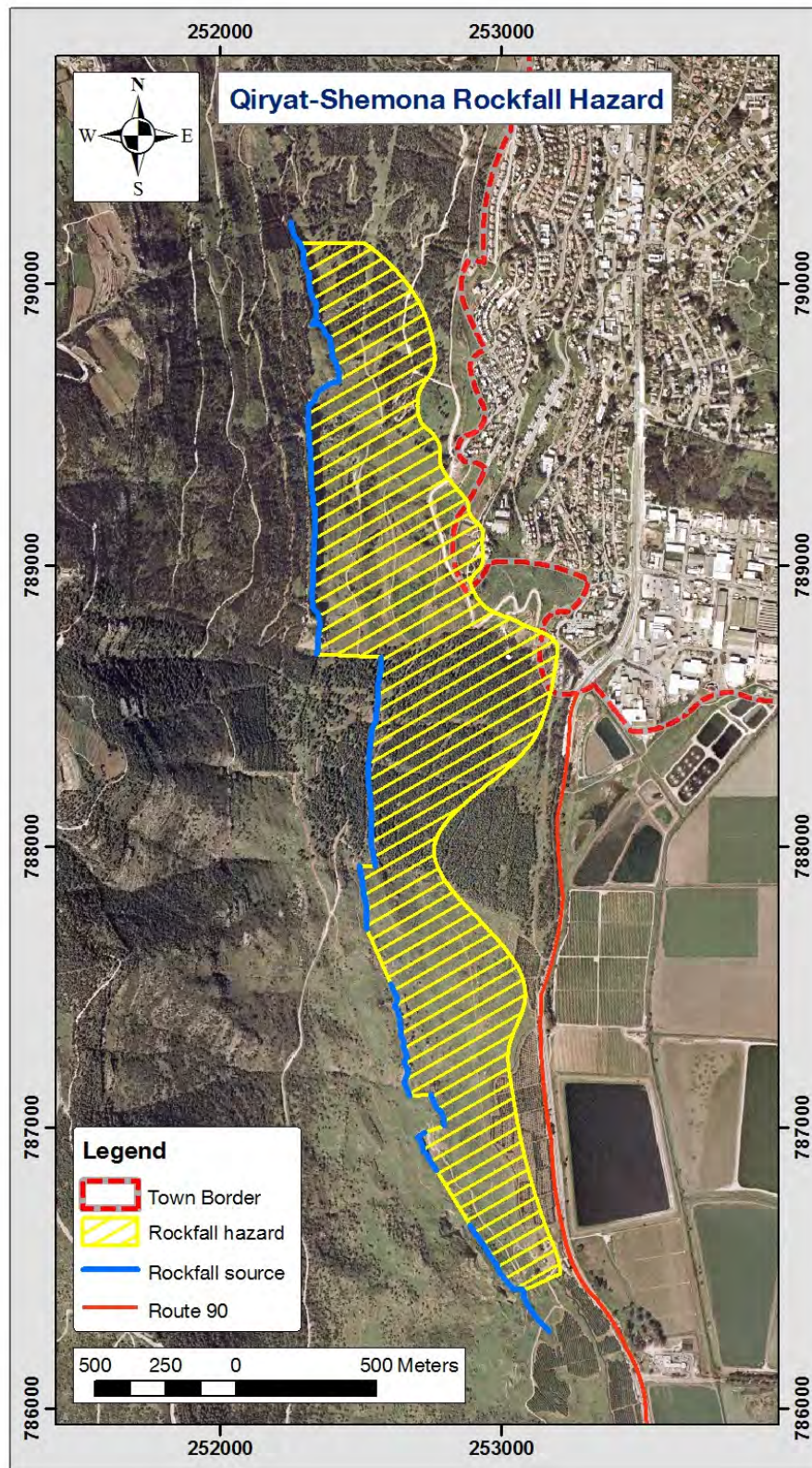


**Figure 3-21.** Rockfall hazard map of Qiryat-Shemona. Source of rockfall (Ein-El-Assad formation) marked in blue line; area subject to rockfall hazard (from source escarpment to 100% of blocks stop line) dashed in yellow; town border line in red dashed line; Route 90 in orange solid line. Map compiled from maximal travel distance (100% of blocks stop line) of 25 rockfall simulation profiles performed using CRSP v4 (detailed in Table 3-9).

### 3.2.4.1 Travel Distance vs. Block Volume

Block diameters simulated for all profiles are detailed in *Table 3-4*. Travel distances for all profile are plotted in *Figure 3-22* (sections separated for plot detail density).

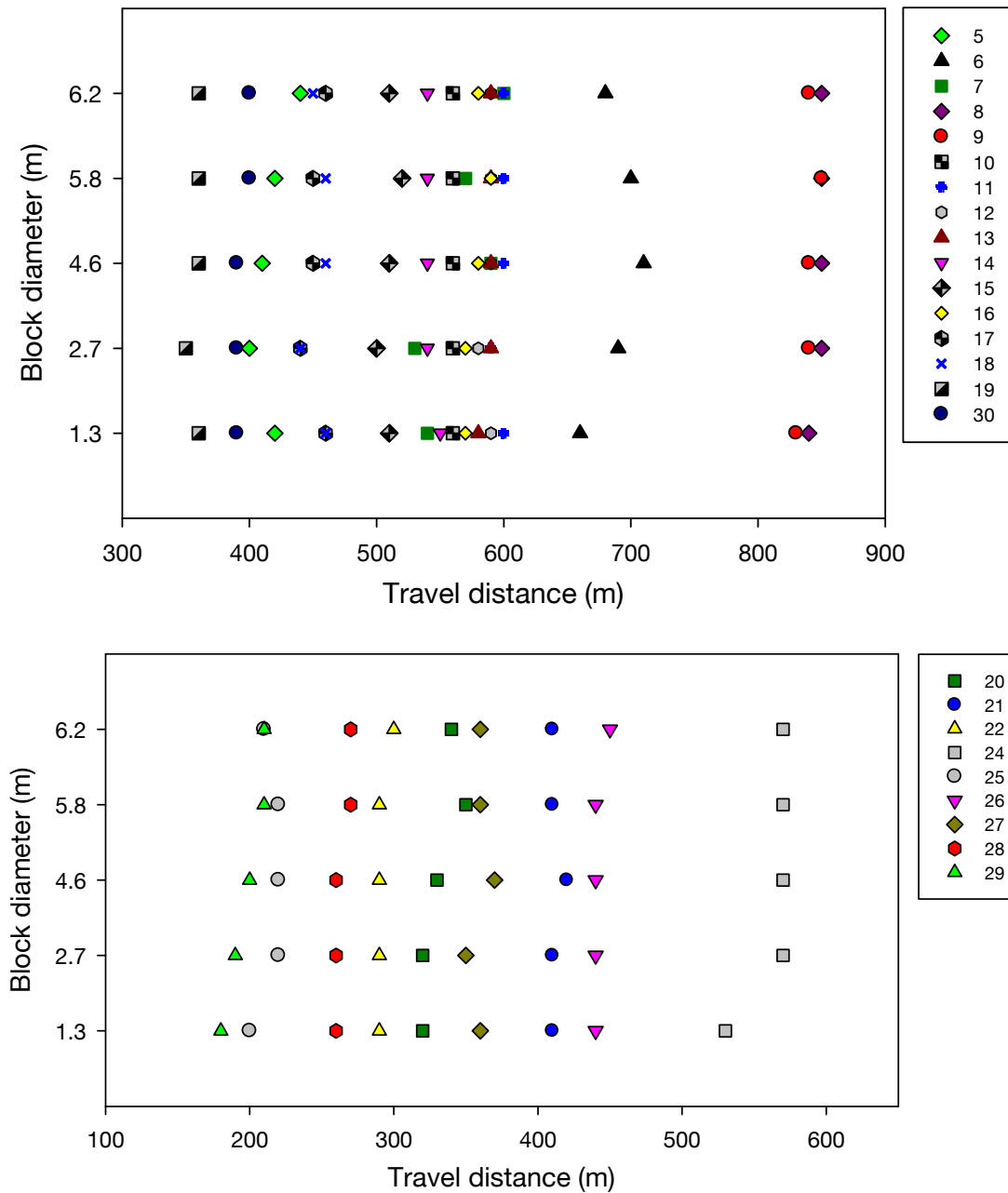


**Figure 3-22.** Maximal travel distances (100% of blocks stopped) of simulated block diameters for profiles 5-19 and 30 at the middle section of the study area (top); profiles 20-29 at the northern and southern sections of the study area (bottom). Profile numbers detailed in legend. For each profile, blocks of all volumes stop at similar distances from the source cliff.

Out of 125 simulation runs along the 25 profiles (*Figure 3-22*), an ‘overshoot’ in the relation of travel distance and block diameter was obtained in 16 cases (on 11 profiles: 6, 9, 14, 15, 16, 18, 20, 21, 25, 27 and 6) where smaller blocks (i.e.  $D=1.3$ – $5.8$  m) have traveled farther than the largest blocks ( $D=6.2$  m). This was resolved by addressing two parameters for each of these runs: a. the relative ‘overshoot’ travel distance (calculated by dividing the overshoot distance by

the travel distance, thus measuring percentage of overshoot); b. the number of blocks which demonstrate this behavior (which equals to percentage since all simulation runs were held using 100 blocks). A summary of overshoot distance and block numbers is detailed in **Table 3-8**.

Since the overshooting percentage of travel distance is very low (mean 2.7%; SD=1.1%) and the number of overshooting blocks is very small (mean 1.8%; SD=1.4%), it is concluded that overshooting of smaller blocks in relation to travel distance of the largest blocks (D=6.2 m) is insignificant and may be neglected.

TABLE 3-8 Travel Distance Overshoot*				
Property	Min	Max	Mean	SD
Overshoot (m)	10	30	12	5.4
Overshoot (%)	1.2%	4.5%	2.7%	1.1%
No. of blocks*	1.0%	5.0%	1.8%	1.4%

\* 16 cases from 11 profiles where D=1.3-5.8 m travel distance was longer than D=6.2 m.

\*\* No. of blocks overshooting beyond the d=6.2 m travel distance out of 100 simulated blocks.

In light of the above it is concluded that hazard analysis may be performed using large block sizes (diameters). It is trivial that larger blocks also represent worst case scenarios anyway in terms of mass and kinetic energy. Block sizes are relevant when considering *probabilities* for different block diameters, and these are detailed in **section 4.3.5**.

### 3.2.4.2 Hazard Map of the Distance Distribution of Block Travel

As concluded above, our hazard analysis is based on the largest blocks (5.8 m, 6.2 m diameter). The CRSP analysis report contains a frequency count of blocks (out of the 100 simulated blocks per run), which stop at each 10 m interval of the simulated profile. These frequencies were summarized (using a *MatLab* code) to cumulative frequencies of 50%, 68% (1 standard deviation), 95% (2 standard deviations) and 100% of all blocks, and the distances they were obtained at are detailed in **Table 3-9**. Maximal travel distance is determined from the 10 m interval where 100% of the blocks stopped. 5.8 m blocks simulated maximal travel distance was usually equal or longer than that of 6.2 m, so this diameter was used for the above calculations of cumulative frequency distance. In any case – the 100% was taken as the longest travel distance, whether it was for 5.8 m blocks or 6.2 m blocks. Cumulative frequency travel distances (detailed in **Table 3-9**) were plotted as map contours (**Figure 3-23** and **Figure 3-24**), which may serve as basis for statistical considerations of rockfall hazard, e.g. the 95% contour denotes the line where 95% of large blocks are expected to stop (meaning there is 5% probability for rockfall impact further beyond this line). Eight simulation profiles (8–14 and 16, marked by the sword ‘†’ in **Table 3-9**) at the south-western part of town demonstrate an intersection of maximal travel distance with town border line, which means that town premises at these profile trajectories are subject to rockfall impact hazard. Distances at which blocks impact town border line are also

detailed in **Table 3-9** to compare against distances covered by the cumulative frequencies of blocks and their travel distances.

TABLE 3-9 CRSP Simulation Travel Distances				
Profile*	50% stop (m)**	68% stop (m)**	95% stop (m)**	100% stop (m)**
22	280	280	290	300
21	380	390	400	420
20	300	310	320	350
19	350	350	360	360
30	370	380	390	400
5	390	390	400	440
18	420	430	450	460
17	430	440	450	460
15	490	490	500	520
16 † (590 m)	560	570	580	590
14 † (510 m)	530	530	540	550
13 † (490 m)	570	570	590	590
12 † (490 m)	570	570	590	590
11 † (500 m)	580	580	590	600
10 † (520 m)	540	550	560	560
7	500	510	520	600
6	460	650	680	710
8 † (780 m)	830	840	850	850
9 † (780 m)	810	830	840	850
24	150	500	550	570
25	10	180	210	220
26	410	420	430	450
27	330	340	360	370
28	240	250	260	270
29	50	180	190	210

\* Profiles are ordered according to their map location from north (top of table) to south;

\*\* Distance at which stated percentage (median, +1SD, +2SD, 100%) of simulated blocks stop; 100% data from simulating 5.8 m and 6.2 m diameter (longest travel distance per profile); all other data from simulating 5.8 m diameter (100 m<sup>3</sup>) blocks.

† Simulated travel distance intersects town border line, introducing rockfall impact hazard to town premises. Travel distances in brackets are where blocks impact town border line.



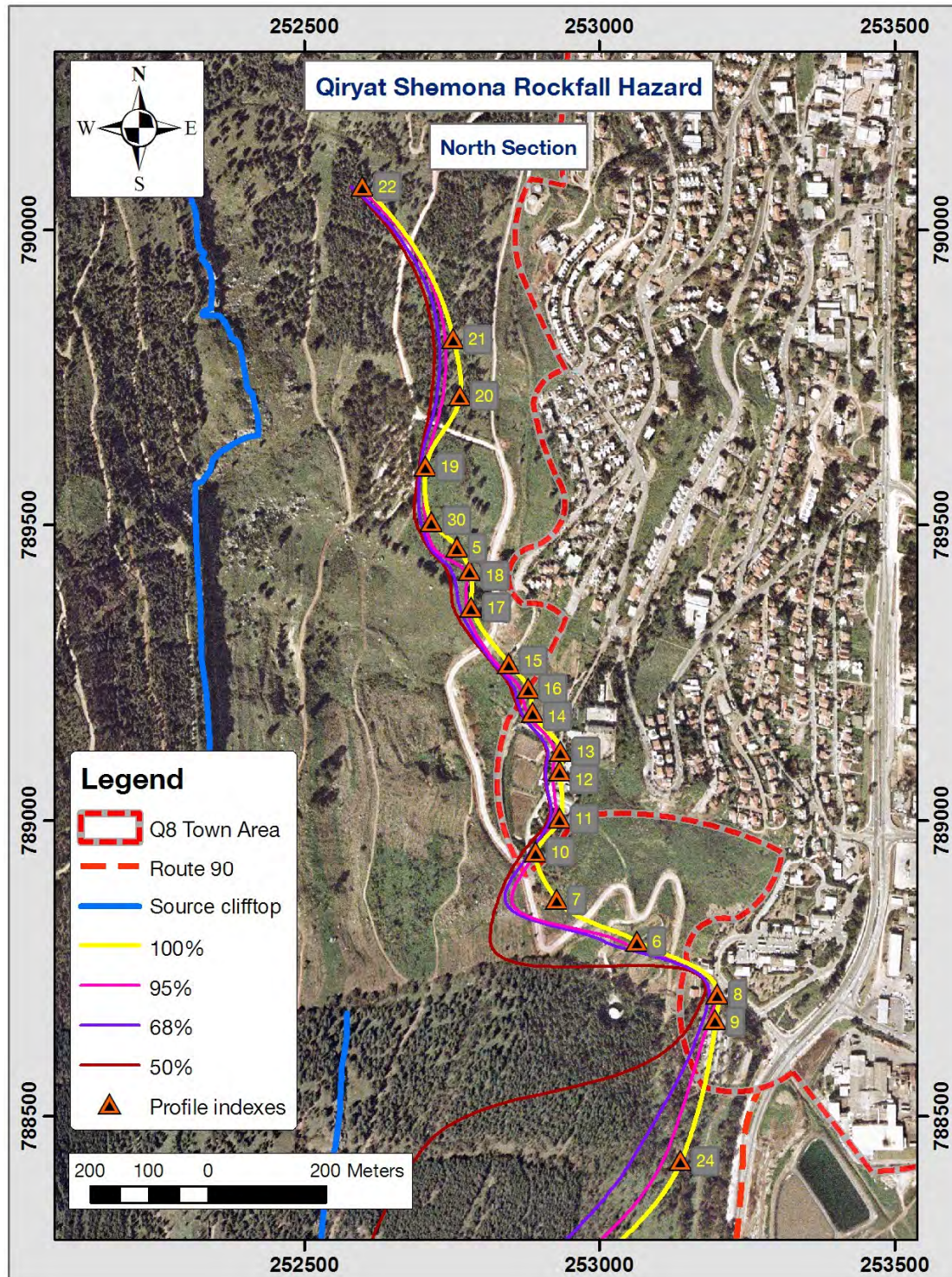


**Figure 3-23.** Cumulative frequency of block stop distances – northern section of study area. Contours denote where given percentage of large falling blocks is expected to stop. Lines are smoothed interpolations from all simulation profiles using 5.8 m block diameter (except 100% line which is comprised of the longest travel distance among 5.8 m or 6.2 m). Orange-hazard triangles are locations of maximal travel distances (100% of blocks) and are labeled per profile; Route 90 marked in dashed red line only outside town premises; see legend for other details.



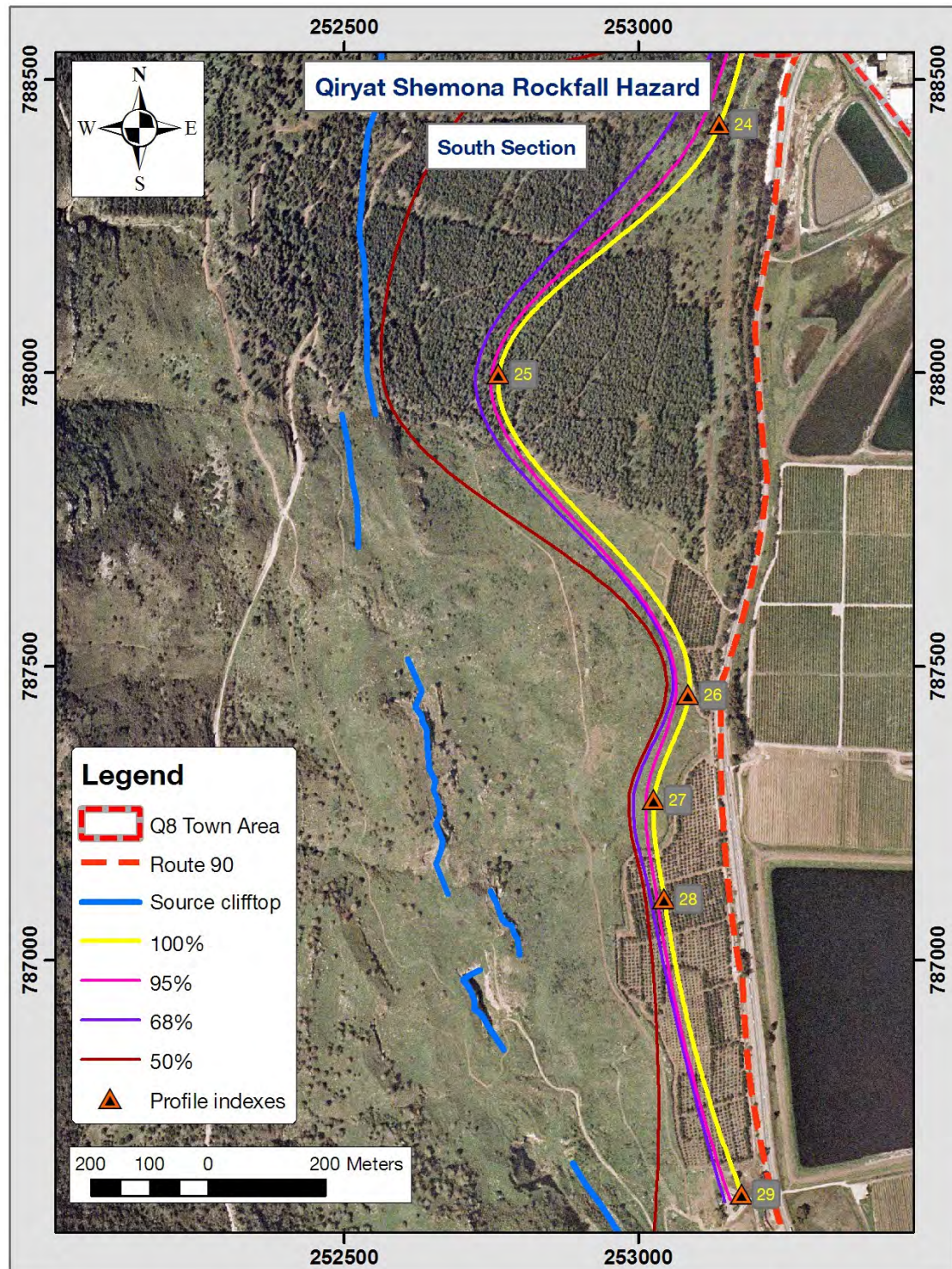


**Figure 3-24.** Cumulative frequency of block stop distances – southern section of study area. Contours denote where given percentage of large falling blocks is expected to stop. Lines are smoothed interpolations from all simulation profiles using 5.8 m block diameter (except 100% line which is comprised of the longest travel distance among 5.8 m or 6.2 m). Orange-hazard triangles are locations of maximal travel distances (100% of blocks) and are labeled per profile; see legend for other detail.

### 3.2.4.3 Stop Location and Slope Angle

Data regarding the angles of slope cells where all blocks stop (*100% stop angle*) and the distance blocks travel within this cell till all come to a stop (*stop swath*) were extracted from CRSP simulation analysis reports (*Table 3-10*).

Profile	Stop Slope Angle (deg.)	Stop Swath Distance (m)
5	10	13
6	10	87
7	9	33
8	6	42
9	5	49
10	4	8
11	8	40
12	5	11
13	5	11
14	7	38
15	9	23
16	9	51
17	8	22
18	10	48
19	3	65
20	12	34
21	9	41
22	7	36
24	8	10
25	7	28
26	11	105
27	8	14
28	7	61
29	7	41
30	8	33

\* Stop angle refers to simulation cell where 100% of blocks stop; stop swath refers to distance within that cell at which 100% of blocks stop. Mean stop angle is 7.7° (SD=2.3°); mean stop swath is 38 m (SD=24 m).



### 3.2.4.4 Minimum Shadow Angle

*Minimum shadow angle* is defined by the angle of a straight line between the highest point of a talus slope (just below the source cliff base) and the stopping point of the longest runout boulder. Typical minimum shadow angles lie between 22°–30° (see *section 1.3.4*). Minimum shadow angles calculated for CRSP simulations and for observed blocks from field and aerial photos (only for profiles traversing the talus located in the study area) are detailed in *Table 3-11*. The mean simulated shadow angle is 21.5° (SD=1.2°) and the mean observed shadow angle is 18.0° (SD=1.7°).

TABLE 3-11 Shadow Angle for Talus Profiles*		
Profile	Simulated Shadow Angle	Observed Shadow Angle
5	20°	16°
15	22°	17°
16	22°	17°
17	22°	20°
18	23°	20°
30	20°	18°

\*calculated minimum shadow angles for CRSP simulation results stop line and for farthest traveling blocks observed from 1946-1951 aerial photos (only for profiles traversing talus). Mean simulated shadow angle is 21.5° (SD=1.2°); mean observed from aerials is 18° (SD=1.7°)

## 3.3 Rockfall Impact Hazard

### 3.3.1 Velocity and Kinetic Energy Analysis

The CRSP analysis report details block velocity and kinetic energy, which can be used to plan defensive measures and design mitigation facilities against rockfall damage. Kinetic analyses provided by CRSP with 98% cumulative probability (i.e. the maximal velocity expected with 98% confidence level) were used in order to obtain worst-case hazard evaluation.

It is pointless to evaluate these kinetic properties at stop line, because the velocities at stop distances are null. Hence, an evaluation of the kinetic properties was performed by locating CRSP analysis points at 95% of the maximal travel distance (within 10 m distance or less from 95% travel point, since CRSP output distance resolution is 10 m). Where simulated blocks impact town border before stopping (profiles 8–14; stop line of profile 16 is located just at town border), stop line is not valid for analysis since there is no way to simulate the movement of blocks through town property (buildings, paving etc.) until they reach the theoretical simulated stop line. Hence, kinetic energy analysis for these profiles was performed at town border, while applying the same considerations stated above regarding 95% of maximal travel distance (considering inner coherence within kinetic analysis results). Predicted block velocity and kinetic energy

(largest block,  $d=6.2$  m; 98% cumulative probability) are detailed in **Table 3-12** and **Table 3-13**. 5% distances from stop line and analysis point distances from stop line are also detailed. Velocity and kinetic energy analyses at stop line or impact line are detailed per profile in the engineering appendix (**Appendix A**).

Profile	5% distance (m)**	Analysis pt dist. (m)**	Velocity (m/s)	Kin. Energy (kJ)
22	15.0	20	5.1	4,423
21	20.5	20	6.2	6,541
20	17.0	20	4.6	4,479
19	18.0	20	7.3	8,740
30	20.0	20	5.7	5,464
5	22.0	20	5.6	6,632
18	22.5	20	7.0	8,086
17	23.0	30	6.7	9,180
15	25.5	20	6.3	6,576
16	29.0	20	6.7	7,445
7	30.0	30	4.5	4,334
6	34.0	30	8.9	12,737
24	27.5	20	8.6	11,972
25	10.5	10	6.7	7,598
26	22.5	30	6.2	6,492
27	18.0	20	6.8	7,619
28	13.5	20	5.7	5,400
29	10.5	20	4.9	4,196

\* Predicted velocity and kinetic energy (98% confidence level) for profiles with no impact at town border.

\*\* Distance between 95% travel distance and stop line; CRSP analysis point located within 10 m distance or less from 95% travel point. See text for detail.

Mean values of 5% distances from stop line compared against analysis point distances from stop line (or impact line) are detailed in **Table 3-14**.

Mean velocity and kinetic energy predictions at the stop line and town border impact points (depending on profile) are detailed in **Table 3-15** and in the engineering appendix (**Appendix A**). At stop line, velocity varies between 4.5–9 m/s and kinetic energy between 4,200–12,800 kJ; at town impact points velocity varies between 10–15 m/s and kinetic energy between 18,000–45,000 kJ (design of energy dissipation systems is discussed in **section 4.4**).

TABLE 3-13 Predicted Velocity and Kinetic Energy at Town Impact Line\*

Profile	5% distance (m)**	Analysis pt dist. (m)**	Velocity (m/s)	Kin. Energy (kJ)
14	39	40	11.9	28,762
13	39	40	14.8	44,479
12	26	30	9.7	17,944
11	25	30	13.9	40,172
10	24.5	30	11.9	29,576
8	24.5	30	12.2	30,441
9	25.5	30	11.1	24,821

\* Predicted velocity and kinetic energy (with 98% confidence level) for profiles at impact with town border.

\*\* Distance between 95% travel distance and stop line; CRSP analysis point within 10 m distance or less from 95% travel point. See text for detail.

TABLE 3-14 Analysis Point Locations vs Stop Line and Impact Line\*

Property		Mean (m)	SD (m)
Stop line	5% of travel deviation	21.1	6.6
	Analysis point deviation	21.7	5.1
Impact line	5% of travel deviation	29.1	6.8
	Analysis point deviation	32.9	4.9

\* Analysis points located within 10 m distance from 95% of travel distance due to CRSP distance resolution.

5% of travel deviation is the distance between maximal travel distance and 95% of it. Analysis point deviation is the distance between analysis point and maximal travel distance (up to 10 m from the 5% travel deviation).

TABLE 3-15 Predicted Velocity and Kinetic Energy Means

Property		Mean	SD
Stop line	Velocity (m/s)	6.3	1.2
	Kinetic Energy (kJ)	7106	2437
Impact line	Velocity (m/s)	12.2	1.7
	Kinetic Energy (kJ)	30,885	8960

\* Predicted velocity and kinetic energy (with 98% confidence level) for profiles at impact with town border.

The above values may be used as general guidelines for rockfall damage mitigation for the entire study area, yet for specific locations it should be based on predicted velocity and kinetic energy at specific locations as in **Table 3-13**.

### 3.3.2 Town Border Impact Hazard Map

CRSP stop line (100% of blocks stop) and CRSP velocity and kinetic energy analysis points at town border (at south-western part of town, where simulations yield rockfall impact at town area) are plotted in *Figure 3-25*. For kinetic analysis detail (block velocity and kinetic energy), locations marked by profile indexes refer to *Table 3-12* and *Table 3-13*, and the engineering appendix tables.

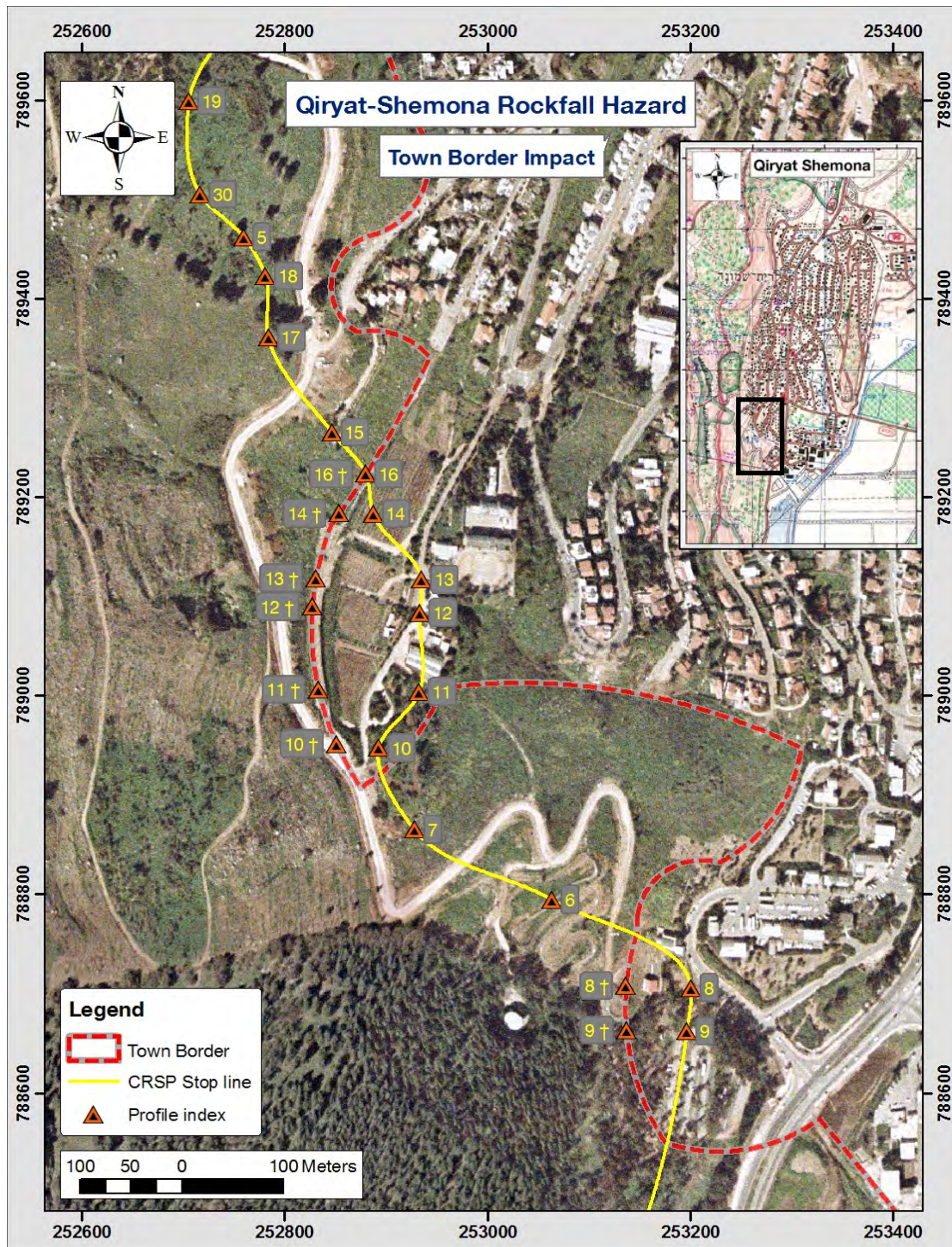


**Figure 3-25.** Rockfall impact hazard at town border line. CRSP stop line in yellow, constructed of a smoothed line of stop locations of largest blocks (5.8–6.2 m diameter) of all profiles; town border in red dashed line; orange-hazard triangles mark simulated stop line for each profile; profile indexes in yellow refer to profile numbers in the engineering appendix tables; indexes with sword label ‘+’ mark locations of rockfall impact at town border; inset: black rectangle outlines map area.



## Chapter 4

---

### Discussion

#### 4.1 Triggering Mechanism of Rockfalls

**T**his section discusses issues related to the source of the rockfall blocks and the triggering mechanism of rockfalls from the Ein-El-Assad Formation.

##### 4.1.1 Nature of the Rockfall Triggering Mechanism

Most rockfalls are associated with triggering events, such as earthquakes, rainstorms, or periods of warming producing a rapid melting of snow. The magnitude and proximity of the earthquake, intensity and duration of the rainfall, thickness of the snow-pack, and the warming pattern, all influence the triggering of rockfalls (Wieczorek and Jäger, 1996). However, some rockfalls occur without a direct correlation to an obvious triggering event; Wieczorek et al. (1995) suggest that such rockfalls occur in granite probably due to processes associated with gradual stress release and exfoliation.

Evidence for a catastrophic (sudden, as opposed to natural rock weathering resulting in toppling of blocks) nature of rockfalls is observed all over the talus area (*Figure 4-1* and *Figure 4-2*): Blocks of varying volumes, from the smallest pebbles to boulders of tens of cubic meters in volume, are grain-supported (i.e. leaning in direct contact against each other) and in many cases show impact deformations on their common faces. This indicates that these aggregations of blocks have traveled to their current location simultaneously. The presence of all block sizes also supports that these are outcrops of large-scale rock mass movements, which include fracturing and disintegration of the blocks into smaller fragments. A slow, natural erosion mechanism could not have resulted in such aggregations, but in large, matrix-supported blocks (i.e. detached from each other by slope soil or debris), with little or no evidence for fragmentation into the smallest fragments.

The above conclusion supports the possibility that the rockfalls were triggered by discrete events such as earthquakes or extreme precipitation events.





*Figure 4-1. Grain supported blocks of various sizes at the talus. Marked length is approx. 70 cm.*

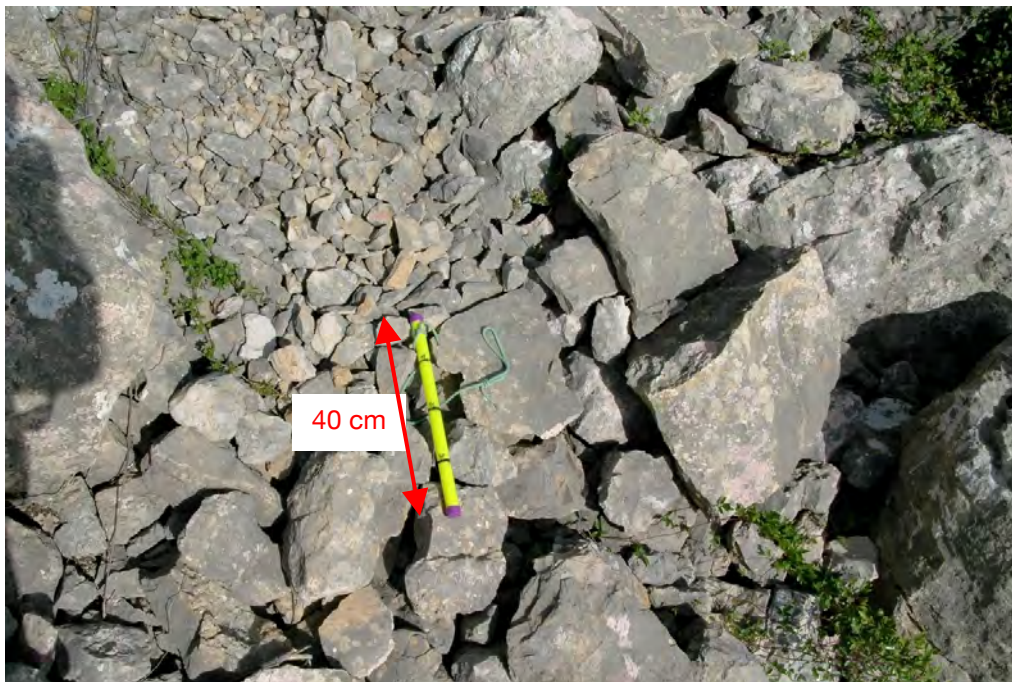


*Figure 4-2. Talus blocks vary in size from small fragments to large blocks. Yellow stick is 40 cm.*

#### **4.1.2 OSL Results and Past Earthquakes**

Rockfall triggering candidates of strong earthquakes for the past 3,000 years were listed using data from earthquake catalogs (Amiran et al., 1994; Guidoboni and Comastri, 2005; Guidoboni et al., 1994). The criteria for catalog earthquakes to qualify as rockfall triggering candidates are: a. their estimated maximum intensity is at least 'IX' on an EMS macroseismic local intensity scale (Amiran et al., 1994; Guidoboni and Comastri, 2005; Guidoboni et al., 1994); b. their calculated moment-magnitude is 6.5 or larger and the distance between the study area and affected



localities reported in the catalogs does not exceed 100 km. This condition satisfies Keefer's (1984) upper limit for disrupted slides or falls triggered by earthquakes based on data from 40 worldwide earthquakes (*section 1.3.3*). Earthquakes are detailed in *Table 4-1*. Two large earthquakes, 1759 AD and 1837 AD, are excluded from the table since no block was dated to later than 1300 AD (including uncertainty range).

Date	Age (ka)	Max Local Int.	Affected Localities
759 BC	2.77	-	Israel**
199 BC	2.21	X	Sidon
363 AD	1.64	IX	Banias, Caperaum, Tiberias, Hamat-Gader
502 AD	1.51	X	Beirut, Sidon, Ptolemais (Akko)
551 AD	1.46	VIII-IX	Sidon, Beirut, Jerusalem, Petra, Jarash
659 AD	1.35	IX	Palestine, Syria
749 AD	1.26	X	Capernaum, Susita, Bet She'an, Tiberias, Hamat Gader, Lod, Jerusalem
1033 AD	0.97	IX-X	Syria, Palestine, Tiberias, Galilee, Jericho
1202 AD	0.81	IX	Safed, Tiberias, Banias, Baal-bek (Lebanon), Bet She'an, Akko, Bet Jan

\* Earthquake data from historical earthquake catalogs (Amiran et al., 1994; Guidoboni and Comastri, 2005; Guidoboni et al., 1994)

\*\* Earthquake cited in the book of Amos; magnitude estimated to 7.3 by Migowski et al (2004)

Migowski et al. (2004) established a high resolution Holocene seismic history of the Dead Sea Transform based on intervals between deformed laminated sediments (seismites). The intervals between seismites were determined by varve-counting in laminated sedimentary cores and radiocarbon dating of seismites, thus correlating deformed sequences in Ein-Gedi (Dead Sea) to earthquakes and their magnitudes. Their profile of the Holocene indicates recurrence intervals of seismic activity varying between a few and 1,000 years, with a conspicuous minimum rate at 2100–31 BC and a noticeable maximum during the past six to eight centuries. They suggest that most of the epicenters of the correlated earthquakes are situated close to the Dead Sea (within 150 km) or up to 400 km north of it along the DST. They suggest an earthquake of magnitude 7.3 in 759 BC and two earthquakes of magnitude 8 (with uncertainty) and 6.8 in 2050 BC and 2100 BC respectively (Migowski et al., 2004) calculated from local intensities according to former studies (Amiran et al., 1994; Salamon et al., 2003). These two suggested events fit OSL ages of soil samples found in the current study, detailed later.

The data are summarized in *Figure 4-3*, which describes OSL ages for the sampled blocks of Qiryat-Shemona for the past 10,000 years.

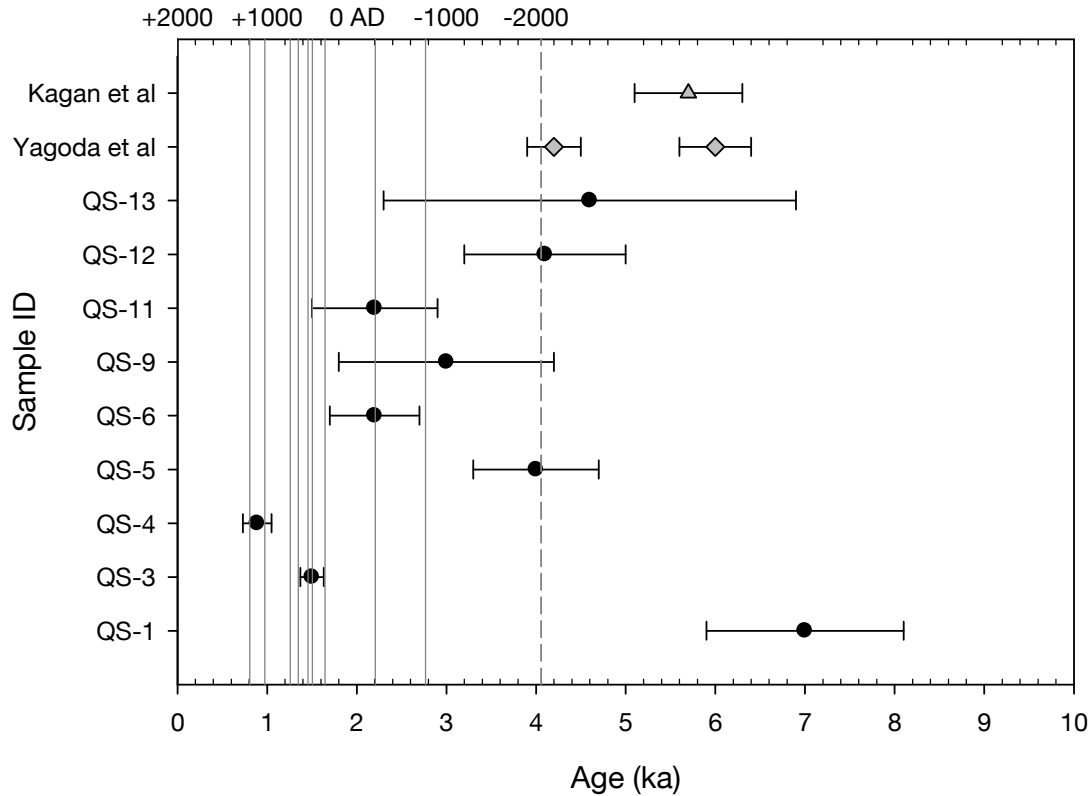


**Figure 4-3.** OSL age results for block samples and candidate triggering earthquakes for the past 4,000 years. Age lab results of 9 sampled blocks plotted as black circles with error bars; ages of earthquakes determined by Yagoda et al. (2007) in gray diamonds and by Kagan et al. (2005) in gray triangle; dates of candidate historic large-scale earthquakes in solid gray lines (**Table 4.1**); candidate earthquake from seismic record in dashed gray line; Christian calendar time scale at top axis (+ is AD, – is BC). Block samples QS-2 and QS-10 are excluded (see detail in text).

Two block samples were excluded from the plot: a. QS-2 which is dated to  $55.7 \pm 7.6$  ka (excluded for a very large uncertainty range); b. QS-10 which is dated to  $8.2 \pm 2.3$  ka, which was sampled at the same block as QS-9 but 30 cm below block–soil interface. Also not included in the plot are QS-7 and QS-8, sampled at a pit for control.

#### 4.1.3 Clustering of OSL Ages

There are three possible interpretations to the OSL results, brought here with supportive pros and possible cons:

- Each age represents a different rockfall event triggered by a different earthquake. **Pros:** a limited number of blocks were sampled (9 ages on which considerations are based) and there are several earthquakes serving as candidates for rockfall triggering. **Cons:** if rockfall events were as frequent as the earthquakes – a rough average of the 9 candidate earthquakes over 2000 years (759 BC–1202 AD) yields an earthquake every 220 years. Such frequent rockfall events do not seem to fit the large block sizes of blocks sampled – since joints defining these sizes probably have not been weakened so fast to re-define such large blocks in such short time spans (otherwise the entire cliff would already crumble down by now).

This is also stressed by the fact that we have no age younger than  $0.89 \pm 0.16$  ka, while large devastating earthquakes have occurred more than once in the region since (e.g. 1759 AD, 1857 AD). Considering that and the high earthquake rate epoch in the past six to eight centuries indicated by Migowski et al. (2004) leads to suggest that cracks may not be ‘ready’ for detachment. The fact that no block was dated as younger than 0.89 ka implies that rockfalls do not occur in such frequency, despite having candidate triggering earthquakes over the past 800 years. OSL dating lower limit is as low as a few years (Lian and Huntley, 2001) and pit samples age results are  $0.27 \pm 0.08$  ka (0.03 m depth) and  $0.71 \pm 0.14$  ka (0.30 m depth) meaning soil from the past 800 years had accumulated on the slope, yet no rockfall evidence was found in this study during that period. However, the latter interpretation is not singular – observations may also be explained by: a. the threshold magnitude for triggering rockfall is higher than the magnitudes of earthquakes in that period; b. a combination of a large earthquake event after (or during) an extremely wet period is required to trigger rockfall, a requirement which hasn’t been met over the past 800 years; c. a set of consecutive earthquakes is required to trigger rockfall.

- b. There are ages which cluster around a small number of certain earthquakes which triggered rockfall events. **Pros:** assuming that **there is** a correlation between earthquakes and rockfall triggering on the Ramim cliff – The ‘cons’ of the latter option are basically the ‘pros’ of this one: very frequent rockfall events (every 220 years) contradict two observations: very large block sizes (up to  $125 \text{ m}^3$ ; see ‘a’ above) and the lack of an OSL age younger than 0.89 ka, regardless of large earthquakes taking place since (e.g. 1759 AD, 1857 AD). On top of that, there is a fit between known historical earthquakes and OSL ages of soil beneath the fallen blocks — suggesting rockfalls might have been triggered by some of these earthquakes, yet rockfalls of such large block sizes are not as frequent, since the rock-mass has to go through a ‘maturation’ phase before it can fail and produce rockfalls.
- c. There is no correlation between earthquakes and rockfall triggering. **Pros:** rockfall may be triggered by precipitation related events (e.g. extremely rainy seasons or severe winter storms) or even occur spontaneously. **Cons:** blocks in the rockfall talus are grain (block) supported, implying catastrophic rockfall events rather than spontaneous, sporadic block detachment, hence there had been a triggering event for these rockfalls other than slow weathering. Precipitation related events may trigger slope movements (Wieczorek and Jäger, 1996) but when specifically discussing rockfalls – correlation is not trivial and pointing out precipitation as the sole triggering mechanism is not a robust enough argument. In any case, the present local climate is not of the kind that produces large rainstorms or thousands of millimeters of annual precipitation. **Figure 4-4** (Bar-Matthews and Ayalon, 2004) shows that at least for the past 4000 years – mean annual rainfall has been similar or less than the present day (except for a high around 4500 BP). Even the extremely rainy winters of 1968/69 and 1991/92, in which annual precipitation in northern

Israel was double than the annual mean, did not trigger any significant slope movements (including rockfalls) on the Ramim cliff.

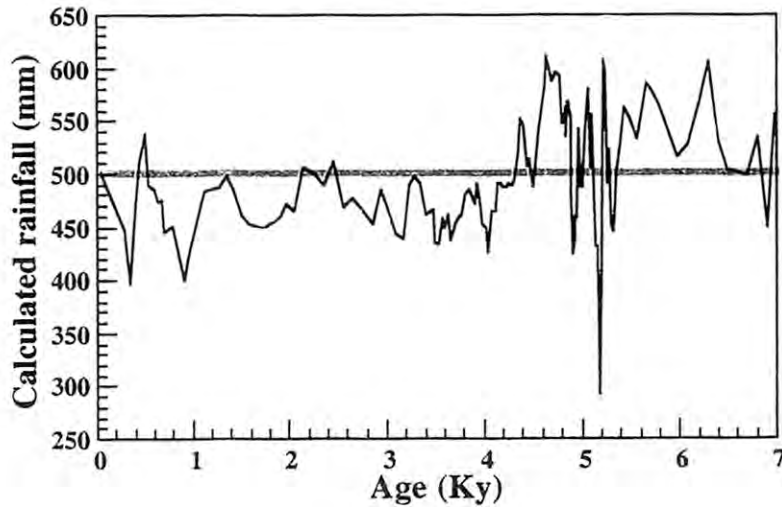


**Figure 4-4.** Calculated paleo-rainfall amount during the last 7000 years (derived from speleothems in the Soreq cave). Horizontal line (around 500 mm) marks present-day mean annual rainfall at the Soreq cave (after Bar-Matthews and Ayalon, 2004).

Concluding the above, the most probable option among the three seems to be option **b** – clusters of OSL ages around earthquakes, which triggered the rockfalls (these clusters are detailed later in **section 4.1.5**). To suggest clustering of ages, results must be tested to rule out the possibility that sampled ages are just a random series in time.

#### 4.1.4 Statistical Validation of OSL Age Clustering

The 9 OSL ages (**Figure 4-3**) span over the past 7000 years, with a mean of 1.3 ages per 1,000 years, but the degree to which only 9 observations are representative of hundreds of blocks on the referred talus is not clear. However, it serves to indicate a possible solution and suggests the need for further collection of field data. The validation of OSL age clustering was obtained performing a binomial distribution test, which gives the discrete probability distribution  $P(k, p, n)$  of obtaining exactly  $k$  successes out of  $n$  trials. The result of each trial is true (success) or false (failure), given the probability for success ( $p$ ) or failure ( $1-p$ ) in a single trial. The binomial distribution is therefore given by

$$P(k, p, n) = \binom{n}{k} p^k (1-p)^{n-k}, \text{ where } \binom{n}{k} = \frac{n!}{k!(n-k)!}$$

A ‘success’ was defined when the date of a given earthquake (out of the 9 candidates in **Table 4-1**) with a  $\pm 50$  years time window was fit with one of the OSL ages with the same error range ( $\pm 50$  years). Since a 50 year accuracy of earthquake dates was needed, the test was performed only for OSL ages with historical record (last 2,800 years). The OSL ages within this range are QS-3, QS-4, QS-6, QS-9 and QS-11. Nine earthquakes, each with a  $\pm 50$  year time window, span totally over 900 years out of the given 2,800 years period. Therefore, the probability  $p$  for a

single random earthquake to occur within this period is  $p=900/2800=0.32$ . The number of trials  $n$  is the number of earthquakes  $n=9$ . In five cases, a success (match between an earthquake and an OSL age, both within a  $\pm 50$  years time window) is obtained, therefore the number of successes is  $k=5$ . The fit between OSL ages and earthquakes is detailed in **Figure 4-5**.

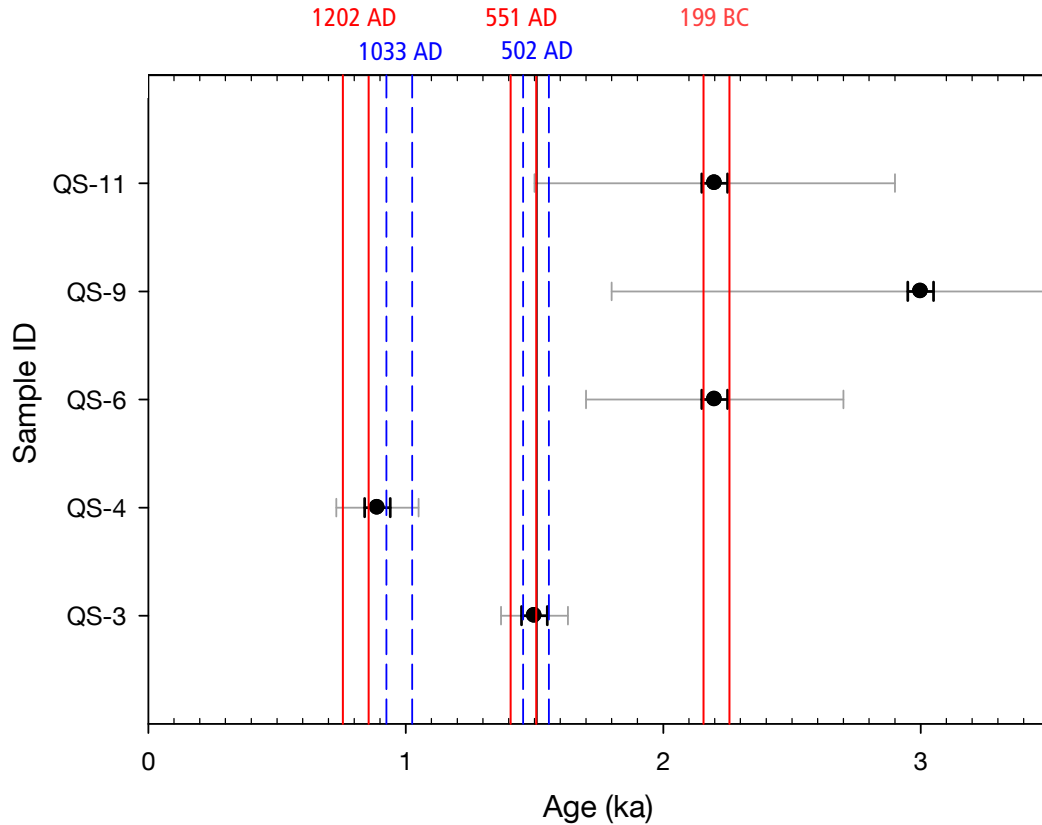


**Figure 4-5.** Clustering of OSL ages around historical earthquake dates. Five ‘successes’ for binomial distribution test were defined using a  $\pm 50$  years time window (see text for detail); vertical lines are  $\pm 50$  years time window around earthquake dates (red solid lines mark earthquakes selected later as rockfall triggers; blue dashed lines mark earthquakes later disqualified as triggers – see next section for detail); black circles are OSL ages with  $\pm 50$  years error bars (black) and their lab reported error range (gray). The binomial distribution is  $P(k, p, n) = P(5, 0.32, 9) = 0.09$ , i.e. there is a 9% probability to obtain such a distribution randomly. This leads to conclude that the OSL ages distribution is significantly clustered around historical earthquakes with 91% confidence level.

Following the above data, the binomial distribution is  $P(k, p, n) = P(5, 0.32, 9) = 0.09$ , i.e. there is a 9% probability to obtain such a distribution. Hence, it is suggested that the OSL ages distribution is significantly clustered around historical earthquakes (and not random), with 91% confidence level. Ruling out two out of the five successes as rockfall triggers (502 AD and 1033 AD, dashed blue lines in figure) is discussed in the next section.

It is concluded that the observed results are not a natural random series of ages – therefore it may be suggested that the ages cluster around specific dates – not just randomly adjacent.

Accepting this significance with 95% confidence may be achieved with further research involving the collection of 20–30 more block ages. It is proposed that currently obtained data exhibits clustering, but a robust validation for it requires enlarging the statistical inventory.

#### 4.1.5 Rockfall Triggering by Earthquakes

Once statistical significance of the clustering of OSL ages around earthquake dates was established, considerations for determination of specific earthquake dates out of the 9 candidates were made as follows:

- a. QS-3 and QS-4 (around 1.5 ka and 0.9 ka respectively) fit the historical earthquakes of 502 AD and 551 AD (or 659 AD with a lesser fit) and 1202 AD or 1033 AD respectively. The 551 AD earthquake is reported at more localities along the DST than 502 AD (reported on shoreline localities only). Since the 1202 AD earthquake accounts for severe damage in other places in northern Israel (Marco et al., 1997; Wechsler et al., 2006), it is a better candidate trigger than the 1033 AD.
- b. QS-6, QS-9 and QS-11 cluster around 2.2 ka, which fits the 199 BC earthquake.
- c. QS-5, QS-12 and maybe QS-13 (with its large error which makes it seem not enough to qualify for age validation). These fit 2050 BC and 2100 BC earthquakes suggested by Migowski et al. (2004). Yagoda et al. (2007), found evidence for earthquake induced slope failure east of the Sea of Galilee with OSL ages of  $4.2 \pm 0.3$  ka and  $6.0 \pm 0.4$  ka (and  $58 \pm 7$  ka) suggesting the area had experienced strong earthquakes (Mw 7).
- d. QS-9 fits the 199 BC earthquake and the 759 BC earthquake (considering error) related to the book of Amos and the earthquake referred by Migowski et al. (2004) as 759 BC.
- e. QS-1 and QS-13 (considering error) may cluster around 6.0–7.0 ka, but in light of the large error range of QS-13 it seems not enough to qualify for age validation. An earthquake event was dated by Kagan et al. (2005) to 5.1–6.3 ka (constrained only by post-seismic dates, i.e. may be older), using U–Th dating of cave speleothems in the Soreq cave near Jerusalem (**Figure 4-6**). This may fit QS-1 (5.9–8.1 ka) but uncertainty range is large. These ages might fit the slope movement evidence dated by Yagoda et al. (2007) to 6 ka at Lake Kinneret vicinity. All these data may point out an strong earthquake event around 6.0 ka.

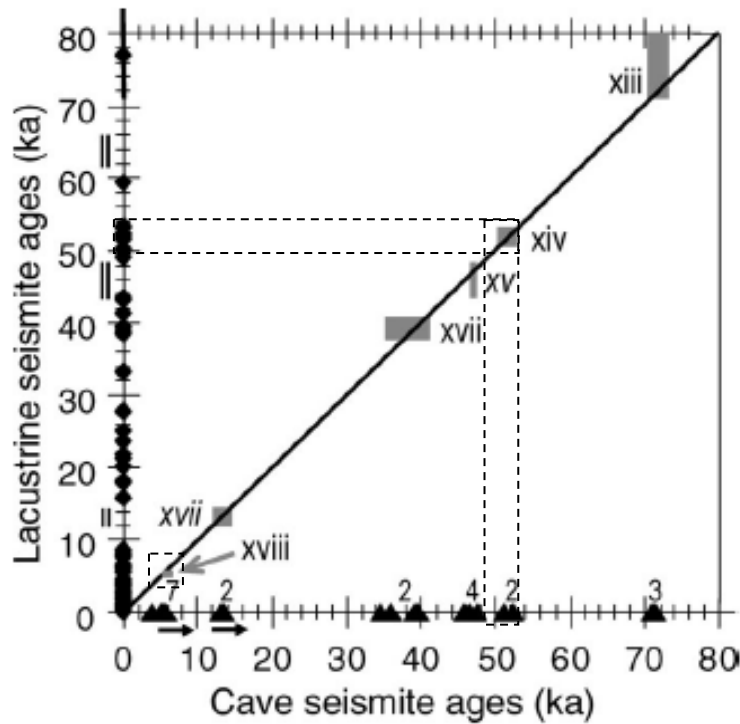


**Figure 4-6.** Correlation of cave seismite ages (triangles, x-axis) with lacustrine seismite ages (diamonds, y-axis) after Kagan et al. (2005). Diagonal line represents 1:1 correlation. Gray rectangles indicate intersection of ages of seismites from independent records; Roman numerals indicate event title; dashed lines denote the fit between two cave seismite ages: a. 51.0–52.0 ka of the earthquake numbered 'xiv' by Kagan et al (2005) fitting lacustrine seismite ages in other independent works (Haase-Schramm et al., 2004; Marco, 1996), which also fit the QS-2 OSL age ( $55.70 \pm 7.60$  ka); b. 5.1–6.3 ka of event 'xviii', which fits the QS-1 OSL age ( $7.0 \pm 1.1$  ka).

- f. QS-2 fits around 55.7 ka ( $\pm 7.60$ ) which might fit the slope movement evidence dated by Yagoda et al. (2007) to  $58 \pm 7$  ka at Lake Kinneret vicinity. Kagan et al. (2005) date an earthquake event to 51–52 ka. They noted that their results fit independent studies dating seismites in the Lisan lacustrine sediments to 52 ka (Begin et al., 2005; Haase-Schramm et al., 2004; Marco et al., 1996).

Kagan et al. (2007) later added that paleoseismic evidence for earthquake related to the  $52 \pm 2$  ka event were found in 3 different sites. They suggest that this seismic event, along with another event at  $39 \pm 1$  ka, are large earthquakes, sufficiently strong to cause cave collapses and lake bottom brecciation in numerous and distant sites in different kinds of sediments. They further suggest that these large events are representatives of the largest (Begin et al., 2005) magnitude earthquakes in the Dead Sea region.

The latter supports that in spite of the fact that the Lisan seismites and the Soreq cave speleothems are distant from the Qiryat-Shemona study area (both over 150 km away), that earthquake may be considered as a trigger for the studied rockfall, although according to Begin et al. (2005) the epicenter is at the Sead Sea. Thus, these  $52 \pm 2$  ka earthquakes may pose a possible fit to the QS-2  $55.7 \pm 7.60$  ka OSL age.



#### 4.1.6 Other Possible Triggering Mechanisms

Rapid snow melting and freeze–thaw cycles are effectively out of the question due to the mild climate of the study area, with mean minimal February (coldest month) temperature around 6°C (IMS, 2007).

Extreme precipitation might be considered a possible rockfall trigger, given the above considerations. However, there are several arguments that weaken this possibility: a. as stated earlier – even the extremely rainy winters of 1968/69 and 1991/92, in which annual precipitation in northern Israel was double than the annual mean, haven't triggered any significant slope movements (including rockfalls) in the study area; b. the case with evidence for possible heavy precipitation (50–55 ka; Bartov et al., 2003) matches a seismic evidence for an earthquake of the largest magnitude in the region around ~52 ka (Kagan et al., 2007). It is possible that a combination of an extremely wet period followed by a large earthquake has triggered the rockfall.

To conclude, extreme precipitation is not over-ruled as a possible rockfall trigger, perhaps in conjunction with earthquakes, but it is beyond the scope of this study to methodically put it to the test.

#### 4.1.7 Conclusion – Rockfall Triggering

OSL ages of soil sampled beneath fallen blocks cluster around a few dates, which are suggested to represent rockfall events triggered by earthquakes or, in one case by an unknown trigger. See summary in *Table 4-2* and *Figure 4-7*.

TABLE 4-2 Rockfall Triggering Candidate Events and Evidence Type*	
OSL Age Cluster	Candidate Triggering Event
0.9 ka ±0.05 ka (1 age)	1202 AD earthquake (his)
1.5 ka ±0.05 ka (1 age)	551 AD earthquake (his)
2.2 ka ±0.05 ka (2 ages)	199 BC earthquake (his)
2.7 ka ±0.05 ka (1 ages)**	759 BC earthquake (ps; his: book of Amos)
4.0 ka ±0.7 ka (4 ages)	2100 BC earthquakes (ps); no historic data; †; exp
6.0 ka ±1.0 ka (2 ages)	No ps data; †
56 ka ±7.6 ka (1 age)***	51–52 ka earthquake (ps); †; exp

\* Evidence types are known historic earthquakes (his), paleoseismic evidence (ps) or possible extreme precipitation (exp) events

\*\* Dashed line separates known historic earthquakes from unreported in history and prehistoric earthquakes

\*\*\* Excluded from graph below (very large uncertainty range)

† Other evidence correlated to large (Mw 7 or more) earthquakes (Kagan et al., 2007; Kagan et al., 2005; Yagoda et al., 2007)

The OSL age determination aided to conclude that earthquakes are the triggering mechanism of rockfalls originating from the Ein-El-Assad Formation and yields important results (discussed later in text) regarding the recurrence time of rockfalls, which may serve later in the evaluation of rockfall hazard to Qiryat-Shemona. However, not all historic earthquakes triggered rockfalls. This may indicate that:

- A combination of a large earthquake event after (or during) an extremely wet period is required to trigger rockfall.
- A set of consecutive earthquakes is required to trigger rockfall.

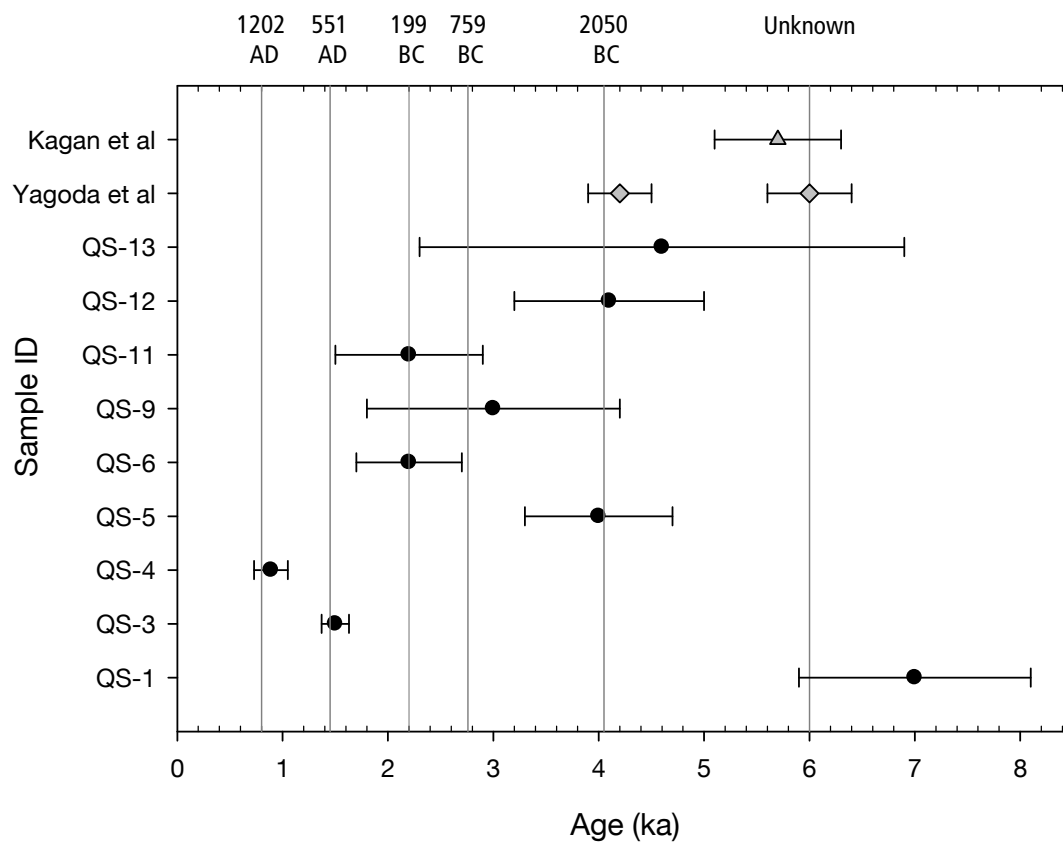


**Figure 4-7.** Qiryat-Shemona OSL ages and suggested rockfall triggers. OSL age results for the past 8000 years in black circles with error bars; ages of earthquakes determined by Yagoda et al. (2007) in gray diamonds and by Kagan et al. (2005) in gray triangle; corresponding dates of earthquakes suggested as rockfall triggers in gray lines and labeled at top axis (see **Table 4-2**). QS-2 ( $55.7 \pm 7.6$  ka) excluded from graph for very large uncertainty range.

#### 4.1.8 Suggestion for Further Study

Dating of 9 or 10 samples is not sufficient in order to detail the history of the hundreds of rock blocks scattered on the slopes of the Ramim cliff. A larger set of age observations is essential to determine the validity of the correlation, which is only suggested here based on what is known given the observations, regarding rockfall triggering by earthquakes for the Ramim cliff.

Considering the above, a suggestion for future work would be collecting a larger number of samples, some located at the upper (western) part of the slope (not reachable with a tractor, require manual excavation). Such work would help getting a clearer, more distinct picture of the age distribution of the Ramim cliff rockfall events.

#### **4.1.9 Seismic Topographic Amplification**

The effect of topography on surface ground motion was observed at many studied earthquakes (e.g. Celebi, 1987; Griffiths and Bollinger, 1979; Hartzell et al., 1994; Havenith et al., 2003; Zaslavsky and Shapira, 2000; Zaslavsky et al., 2000). Close links between site effects due to topography and damage of structures were reported by many investigators (e.g. Celebi, 1987). Characterizing the effect of topography is commonly performed using the spectral ratio technique at various points on a topographic feature (at the ridge top and valley bottom, and also along the slopes relative to a reference station).

The Manara strong motion station installed on the high plateau near the top escarpment of the Naftali Mountains ridge (some 400 m above the Ein-El-Assad Formation escarpment) was triggered by an earthquake in the Dead Sea that occurred on 11.02.2004 ( $M_L=5.2$ , epicentral distance 165 km). Zaslavsky (2008) found H/V ratios to clearly exhibit a resonance peak near 2.5 Hz with amplification up to 6.0. At the NS components, amplification at 3.0 Hz was observed with corresponding amplitude of about 4.0.

This topographic amplification of seismic shear waves supports the suggestion that earthquakes trigger rockfalls from the Ein-El-Assad Formation escarpment, located less than 1 km east to the Manara station. Surface ground motions induced by local earthquakes are amplified several times within the topographic high, increasing the probability for triggering of rockfalls from the Ein-El-Assad Formation.

Amplification is expected to be stronger at higher parts of the ridge – it is therefore expected to find rockfalls triggered by amplified ground motion at the escarpments located higher above the Ein-El-Assad Formation outcrop. This may suggest future study of rockfalls of the Naftali Mountains from these potential outcrops.

#### **4.1.10 Magnitude of Triggering Earthquakes**

A lower limit for earthquake magnitude required to trigger rockfall is not trivial, especially in light of the above discussed topographic amplification of ground motion. Smaller earthquake magnitudes occurring in the vicinity of the study area (situated on one of the Dead Sea Transform branches) induce ground motions which, once amplified by topography, may trigger rockfalls. A recent earthquake (15.2.2008;  $M_L=5.2$ ) occurred in Lebanon, some 18 km northwest from the study area. Field survey hasn't been carried out since that earthquake, but no evidence for rockfalls at the study area has been reported.

Nevertheless, it should be noted that this topographic setting has always been true regarding the Ein-El-Assad escarpment, and still rockfalls have not been very frequent as already stated earlier. Once again, it is suggested that strong ground acceleration is not the only term for triggering of rockfall, but a certain stage of maturity of fracture weakening (and/or deformation) of the rock-mass must be fulfilled in order to trigger the rockfalls. Suggested rockfall triggering earthquakes (*Table 4-2*) are of estimated magnitudes  $M_w$  6.8–7.5 (with maximal epicenter distances of 100–150 km respectively) according to the catalogs and paleoseismic data from which they were extracted, thus it is concluded that  $M_w \geq 7$  with maximal distance from epicenter of 100 km is a lower threshold for magnitudes of rockfall triggering earthquakes.

#### 4.1.11 Rockfall Recurrence Interval

Recurrence times of the suggested rockfall events (*Table 4-2*) can be estimated by dividing 6 events over a 5.2 ka time span (last known rockfall at 1202 AD; earliest rockfall at 6.0 ka), yielding a mean of about 850 years between consecutive rockfalls ( $SD=570$  yrs). The ~56 ka OSL age is excluded from these calculations since there were no OSL ages found between 6 ka and 56 ka, while for the past 6 ka there were 9 ages found. This 50 ky gap may be explained by: a. more OSL data must be obtained; b. a very long rockfall quiescence period – which does not fit the rockfall and earthquake recurrence intervals suggested here and is therefore less probable. Suggested triggering threshold  $M_w \geq 7$  falls in good agreement with Begin's (2005) recurrence intervals of earthquake magnitudes for the Kinneret-Dead Sea segment (*section 1.2.2*):  $M_w$  6.5–7.0 recurrence interval is between 800–3000 years.

## 4.2 Rockfall Trajectories and Affected Area

### 4.2.1 Characteristics of Block Stop Locations

Stop angles and swaths results (*section 3.2.4.3*) and all other cell slope angles per profile (calculated from cells' start and end coordinates) are plotted in *Figure 4-8*. 100% stop angles (where 100% of the blocks stop) of all profiles (red circles in figure) have a mean of  $7.7^\circ$  with  $SD=2.3^\circ$  (minimum of  $3^\circ$  and maximum of  $12^\circ$ ); 50% stop angles (where 50% of blocks stop; blue triangles) have a mean of  $10^\circ$  with  $SD=5.3^\circ$  (*Table 4-3*). All other cell slope angles (gray circles) vary widely between  $7^\circ$ – $88^\circ$ , among them very few are less than  $10^\circ$  (*Figure 4-8*). This leads to conclude that a. most blocks (50% at least) keep traveling down-slope until the slope angle decreases to  $10^\circ$ – $15^\circ$ ; b. all blocks stop where the slope angle decreases to  $5.5^\circ$ – $10.0^\circ$  (considering standard deviation). Stop swath distances (*Table 4-4*) vary between 8–105 m, having a mean of 38 m with  $SD=24$  m.

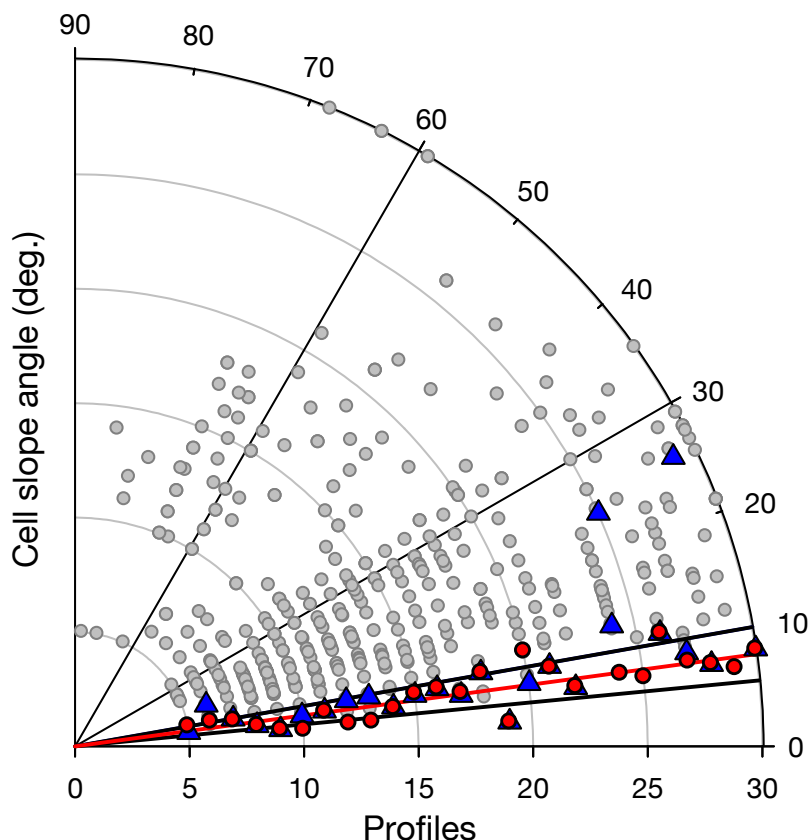


**Figure 4-8.** Slope angle at 50% and 100% of blocks stop. Cell slope angles of all CRSP simulation profile cells in gray circles; 50% stop angles in blue triangles; 100% stop angles in red circles. See Table 4-3 for means and standard deviations.

An attempt to correlate stop angle and stop swath distance using a linear regression yielded  $R^2 = 0.13$  ( $n=25$  profiles) and it is therefore suggested that there is no correlation found between the two. This leads to conclude that characterization of block stop locations should be based both on stop angle and stop swath distance – 100% block stop occurs when both conditions are met.

To conclude the characterization of rockfall stop line (regarding the discussed study area), two possible distinctions are considered: one based on statistic properties (means and standard deviations), the other based on extreme values (lowest slope angle and longest swath distance) and is therefore more conservative. These are referred to in Table 4-4 below as the ‘statistic’ and the ‘conservative’ approaches. Results may differ in other slopes, where the mechanical properties of the slope and rock blocks are different.

TABLE 4-3 Slope Angle Where 50% and 100% of Blocks Stop		
Percentage of blocks stop	Mean Slope Angle (deg.)	SD (deg.)
50%	10°	5.3°
100%	7.7°	2.3°

TABLE 4-4 Rockfall Block Stop Location Characterization

Approach	Stop Slope Angle (deg.)	Stop Swath Distance (m)
Statistic*	5° – 10°	14 m – 62 m
Conservative**	3°	105 m

\* Mean 7.7° stop angle with SD=2.3° and mean 38 m stop swath distance with SD=24 m.

\*\* Lowest stop angle and longest stop swath.

#### 4.2.1.1 Implications for Rockfall Hazard Mitigation Design

The above conclusion and angle/swath distance values may be related when considering rockfall mitigation design. The above values mean that falling blocks would stop after covering a distance of 14–62 m in a slope angle of 5°–10°, while the conservative values mean that blocks would stop after traveling 105 m in a 3° slope. The design of such a flat artificial topographic surface may stop traveling blocks, but it is also not recommended since it involves an expensive project with severe damage to the natural environment. Other mitigation acts, some better suited for the natural environment and easier to accomplish are suggested later in this chapter (*section 4.4.2*).

#### 4.2.1.2 Mis-fit of Small Blocks Simulated Travel Distances

The longer observed than simulated travel distance of smaller blocks (*section 3.2.2*) may be explained in a few ways: First, smaller blocks may be more subject to down slope creep – being more affected by water runoff and slope material movement due to their smaller size. Therefore they travel further down after the rockfall event took place. This is re-enforced by the minimum shadow angle results (*section 3.2.4.4*) which yield mean *simulated* shadow angle of 21.5° (SD=1.2°) and mean *observed* shadow angle is 18.0° (SD=1.7), while typical worldwide values are 22°–30° (Dorren, 2003), which leads to suggest that the longer observed than simulated distances (resulting in shallower shadow angles) are not typical for rockfall behavior — these blocks may have traveled to their current locations by creep mechanism. Second, some of the small blocks (<1 m) might have been misinterpreted as blocks during the analysis of 1946 and 1951 aerial photos. All blocks demonstrating such behavior were observed on aerial photos only, since they were situated where the town is built today. As for the larger blocks demonstrating longer observed than simulated travel distances – one interpretation suggestion is also related to the aerial photo interpretation at which 2-D block surface observations were extrapolated to 3-D block volumes based on field observations (*section 2.1.4*). It is possible that blocks which appear to have larger surface area in the aerial photos were actually discoidal (flat) and therefore had smaller volumes and so might have been moved by slope creep down slope along with other smaller blocks.

Another interpretation, which is suggested for all block sizes demonstrating longer observed than simulated travel distances is based on the fact that the construction of town has created a

different topographical setting than the slope on which the blocks had traveled during rockfall events at the past. This observation occurs (in most cases) for blocks on simulation profiles for which travel distances reach town border or very close to it (see profiles 6–13 in **Figure 4-9**). A built area involves surface leveling and the town itself has introduced a flat area where once a slope existed. Since the simulation profiles were created from current topography, which includes that ‘flattening’ of the slope, simulated (and future rockfall) blocks no longer travel to the distances at which they were observed before town was built. For example, the simulation travel distances of profiles 10–12 are close to town border (red dashed line), while observed blocks (yellow rectangles) have traveled up to 300–400 m further down slope. As detected from elevation contour density (white lines), town buildings and nearby fields have created a ‘flatter’ surface which would render potential falling blocks to a stop (see blue inset in **Figure 4-9**). This argument is reinforced by the conclusions about the relation between the stopping of blocks and slope angle discussed earlier in the text (**section 4.2.1**). The observed blocks extracted from the 1946 aerial appear to have come to a 100% stop at a slope portion with an angle of 6°. This suffices to meet the ‘*statistic*’ terms suggested in **Table 4-4**.

One should be aware of the possibility of a ‘*chicken and egg*’ case, according to which the town built premises developed into the already flatter topographic locations. No topographic data dating before the construction of Qiryat-Shemona is available at that resolution (e.g. 5 m elevation contours used in this study), but this possibility can be ruled-out by examining the few blocks that seem to lie on an undisturbed slope further away from stop line (see green inset in **Figure 4-9**). Before construction of town these blocks could travel to these locations, and after construction, topography west to that undisturbed slope (where profiles 7 and 10 are marked) is flatter and blocks are unable to reach it.



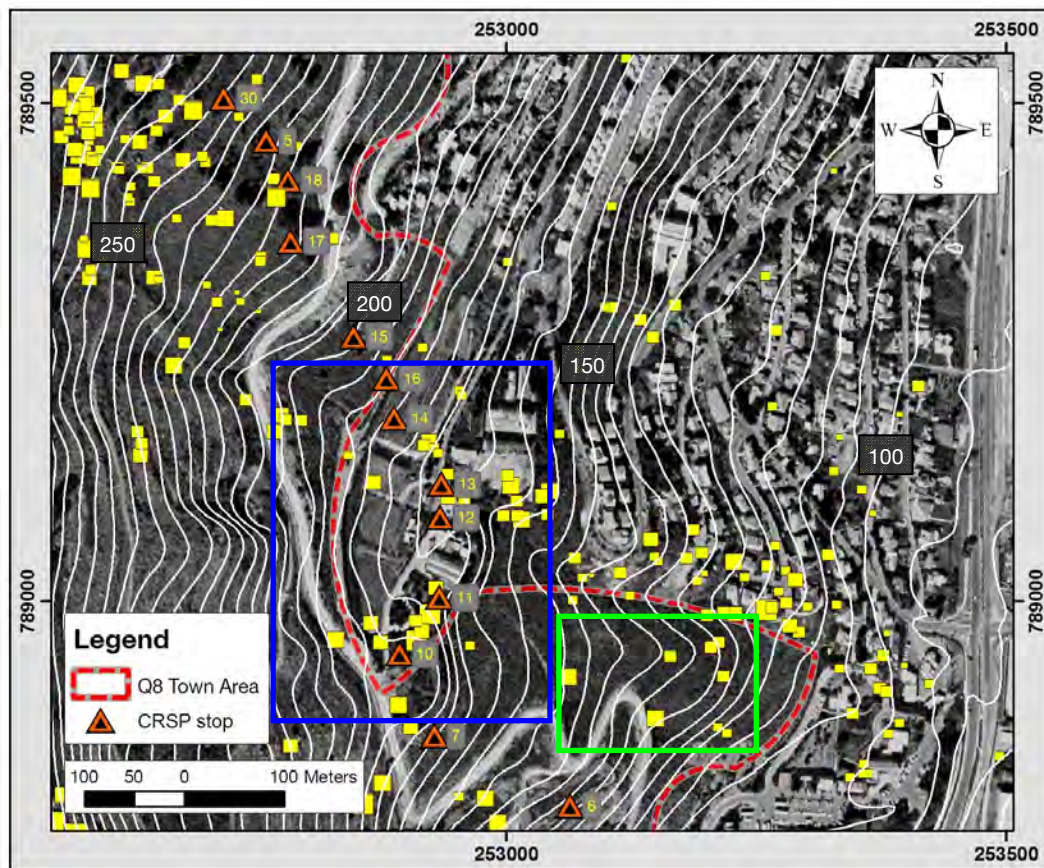


**Figure 4-9.** Observed blocks (from field and 1946–1951 aerial photos) vs. CRSP simulated travel distances. Observed blocks in yellow rectangles (larger marks are larger blocks); simulated maximal travel distances for each profile in orange-hazard triangles with profile numbers in yellow; town border in dashed red line; 5 m elevation contours in white (50 m contour labels); refer to discussion in text above for blue and green insets. Most of the observed blocks located at larger distances than simulated are on profiles 6–13 (southern part of town).

### 4.3 Hazard from Future Rockfalls

Maps detailing different aspects of rockfall hazard are presented in *sections 3.2 and section 3.3*. Following is a discussion regarding their significance.

#### 4.3.1 Rockfall Hazard Area Map (Fig. 3-21)

This map details the area subject to future rockfall hazard from the largest predicted blocks ( $D=6.2$  m,  $V=125$  m<sup>3</sup>).

This map may be used for several aims, such as:

- Locate existing specific points or areas of interest which are presently under rockfall hazard and may require mitigation actions.
- Check whether rockfall hazard exists for future planned areas of interest.
- Locate safe locations for any sort of future planning (e.g. buildings, parks, roads and infrastructure).

### 4.3.2 Town Border Impact Hazard Map (Fig. 3-25)

This map details the locations where future rockfalls are predicted to impact town premises. Since there is no simple way to simulate the moving blocks along town premises (e.g. buildings, parkways) it is assumed that the first line of buildings/town property would suffer the rockfall impact. Exact locations where each simulated profile impacts town premises are marked, referring to the analysis of predicted block velocity and kinetic energy at that point (detailed also in the engineering appendix).

This map may be used to:

- Identify locations of specific town premises currently subject to rockfall hazard.
- Use the specifically referred velocity and kinetic energy analysis to design mitigation actions for specific localities or for future planning.

### 4.3.3 Frequency of Stopping Blocks and Analysis Location Map (Fig. 3-23/24)

This map details the locations of cumulative frequency of block stop distances (50%, 68%, 95% and 100% of simulated blocks). This map demonstrates the width of the swath where most of the falling blocks stop (*section 4.2.1*). The map demonstrates that most of the falling blocks are predicted to reach similar distances as the farthest traveling blocks (except for the locations of profiles 24–25). It should be noted that for each simulation along a profile, 100 blocks were simulated and cumulative block number data was collected, but the simulation algorithm of CRSP v4 simulates each of these 100 blocks as a single block traveling down-slope (mutual interaction between falling blocks is not applied). It is probable that during rockfall, some of the blocks interact while traveling down-slope and their distribution along slope would be somewhat different (some of the energy is dissipated in block interactions and blocks may stop earlier). Using 100 simulated blocks contributed the ability to extract statistical aspects of the rockfall, under a worst-case scenario. This map also includes reference points to locations where the velocity and kinetic energy analysis was performed for each slope profile (which also refer to the engineering appendix).

This map may be used to:

- Refer to velocity and kinetic energy analysis at specific locations at the end of each profile (also available at the engineering appendix).
- Locate point or areas subject to larger probable hazard (where cumulative probability of block which have stopped is lower – predicted hazard is higher since a larger number of blocks are still in motion in that location).
- Locate areas or points of interest west to Route 90 at the southern part of the study area (beyond the southern border of town) and use local velocity and kinetic energy analysis for present mitigation design and future planning.

#### 4.3.4 Rockfall Hazard Evaluation for Qiryat-Shemona

Rockfall hazard evaluation is performed by multiplication of the probabilities of each term required to occur simultaneously, as hereby detailed.

#### 4.3.5 Rockfall Block Size Probability

Cumulative probabilities for selected block diameters, calculated from the  $p(D)$  regression curve (**Figure 3-6**), which correspond to blocks of given sizes or smaller ( $P_D$ ) are detailed along with the probabilities for blocks larger than same given size ( $1-P_D$ ) in **Table 4-5**. These may serve later as guidelines for engineering solutions in terms of kinetic energy. Cumulative probability for  $D=1.3$  m ( $V=1$  m<sup>3</sup>) is unavailable since no data was collected for  $D<1.3$  m. Note that the regression curve yields probability of 1.00 (100%) for blocks of diameter  $D\geq 6.0$  m ( $V\geq 113$  m<sup>3</sup>).

Block Diameter (m)**	Volume (m <sup>3</sup> )	$P_D$ ***	$1-P_D$ ***
2.7	10	0.671	0.329
4.6	50	0.891	0.109
5.8	100	0.986	0.014
$\geq 6.0$	113	1.000	0.000

\* Probability derived from fit-curve for block diameter cumulative probability  $p(D)$

\*\* Probability for  $D=1.3$  m ( $V=1$  m<sup>3</sup>) is not available (no data collected for blocks  $<1$  m<sup>3</sup>)

\*\*\*  $P_D$  is probability for given block size or smaller (worst-case);  $1-P_D$  is probability for larger than given size

#### 4.3.6 Rockfall Recurrence Time Probability

Rockfall occurrence probability  $P_R(\Delta t)$  is based on the OSL ages analysis, which yielded a mean recurrence interval of 850 yrs (**section 4.1.11**). A 50 year period is common when discussing engineering projects and the Israeli Building Code 413 is based on this period, therefore rockfall occurrence probability relates to a 50 year time period noted as  $P_{R50}$ .

Considering the youngest OSL age that was determined in this study (0.9 ka), the last known rockfall was assigned the date of the 1202 AD earthquake (**section 4.1.7**). This means that currently (2008) we are already in a rockfall quiescence period of 800 years. Since rockfall recurrence is time-dependant and not random (earthquake magnitude recurrence dependant; requires 'maturation' of rock-mass), conditional probability analysis – also used to calculate probability for strong earthquake occurrence (Begin, 2005) – should be used to account for the 800 years of rockfall quiescence period.

Assuming no event had occurred since the last rockfall until today ( $t$  time), conditional probability for a rockfall to occur during the next  $\Delta t$  time period is introduced by calculating the ratio between the area of the future time period ( $\Delta t$  wide) under the Gaussian density function

over the entire area under the Gaussian from  $t$  time onwards (Begin, 2005). For example, conditional probability for an event during the next 50 years, after  $t$  years elapsed since the last event is:

$$p \{ [\text{event within 50 years}] \mid [\text{event after } t \text{ years}] \} = [p(t+50) - p(t)] / [1-p(t)]$$

$p(t)$  and  $p(t+50)$  are calculated from the standard  $Z$  value

$$Z = (t - \tau) / \sigma$$

where  $\tau$  is the mean recurrence interval and  $\sigma$  is its standard deviation;  $t$  is the time past since the last event (Begin, 2005).

Introducing the recurrence interval and SD found in **section 4.1.11** above (to the best knowledge of this study) leads to suggest that rockfall recurrence probabilities  $P_R(\Delta t)$  for the next rockfall event are  $P_{R50}=0.065$  (6.5% during 2008–2058) and  $P_{R475}=0.575$  (57% during 2008–2483).

### 4.3.7 Rockfall Hazard Evaluation for Given Time Period and Block Size

Rockfall hazard  $H_R$  is calculated by multiplying the recurrence time probability  $P_R$  for given period  $\Delta t$  (years) by the required cumulative probability  $P_D$  for given block diameter  $D$  (m)

$$H_R(\Delta t, D) = P_R(\Delta t) * P_D(D)$$

The PGA value of the Israeli Standard building code 413 states minimal ground acceleration with 10% probability in a period of 50 years, which statistically equals the probability for the same ground acceleration (or higher) at least once in 475 years (Shapira, 2002). Following these time periods, the evaluation of rockfall hazard for 50 and 475 year periods ( $P_{R50}$ ,  $P_{R475}$ ) for selected block sizes is presented in **Table 4-6**. Hazard is evaluated per given block size or smaller.

TABLE 4-6 Rockfall Hazard Evaluation for 50 and 475 Years		
Block Diameter (Volume)	$H_{R50}$ Probability*	$H_{R475}$ Probability*
2.7 m (10 m <sup>3</sup> )	0.044 (4.4%)	0.38 (38%)
4.6 m (50 m <sup>3</sup> )	0.058 (5.8%)	0.51 (51%)
5.8 m (100 m <sup>3</sup> )	0.064 (6.4%)	0.56 (57%)
6.0 m (113 m <sup>3</sup> )	0.065 (6.5%)	0.57 (57%)
6.2 m (125 m <sup>3</sup> )	0.065 (6.5%)	0.57 (57%)

\* Probability for impact by given block size or smaller (worst-case estimation); calculated for 850 yr rockfall recurrence time conditional probability for an 800 year rockfall-quiescence period (since 1202 AD earthquake) derived from OSL ages.

## 4.4 Rockfall Impact Mitigation Design

### 4.4.1 Possible Design for Mitigation of Rockfall Damage

As stated above (*section 4.2.1*), design according to stop angles and swath distance may be efficient, but also expensive and harmful for the local environment. Following is a brief list of some common engineering solutions (after Berger, 2004).

- *Dynamic or static energy barriers* which are usually a system of cable nets 5–10 meters long and 3–4 meters high, fixed to the land by posts and cables, with some energy dissipater system introduced (Berger, 2004). Most are capable of dissipating a relatively low kinetic energy ( $E_{\max}=2,000\text{--}5,000$  kJ for the best dynamic barriers) which is unsatisfactory compared against the block energy at town impact points (up to 45,000 kJ) estimated in this study.
- *Roadside ditches* are built in width and depth depending on the height and degree of the slope, aimed at trapping falling blocks. Large blocks (as the ones in this case) require deep and wide ditches and this solution may be unsuitable for the study area.
- *Semi-tunnels or concrete walls* to trap falling blocks are made of concrete. Their cost is proportional to block size requiring retention, and therefore they may be very expensive under the constraints of the study area. Environmental impact should also be considered: These measures are not-aesthetic, form barriers for animals and alter the natural erosion pattern.

### 4.4.2 Mitigation by Forests

The final report (Berger, 2004) of the *ROCKFOR European Project (ROCKFALL – FOREST Interrelation: Efficiency of the Protective Function of Mountain Forest against Rockfall)* deals with many aspects of rockfall mitigation. **Figure 4-10** demonstrates how a single tree (in optimal location – where a falling block hits it head-on) may be of use to dissipate the block's kinetic energy, versus blocks that reach impact line with town border at estimated kinetic energy of 18,000–45,000 kJ for  $D=6.2$  m blocks. In order to answer for hundreds of falling blocks, design of a forest with appropriate tree species planted in appropriate density should be performed. From an environmental point of view, this is the best mitigation solution.

A thorough study is required in order to implement the mitigation measurements detailed in the above report, e.g. identifying the counterparts of the specified European tree species among the local north-Israeli species (if they exist), or locating the areas where such a forest is the most-effective (e.g. at the parts of the slope where block velocities are low).

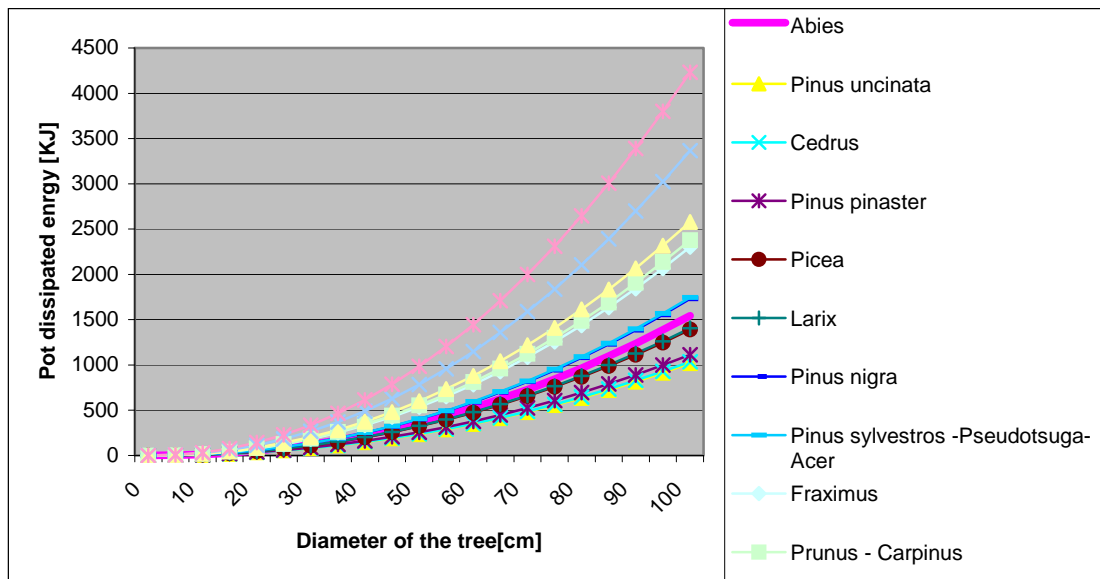


**Figure 4-10.** Maximum energy (kJ) that could be dissipated by different tree species with a certain diameter in cm. (after Berger, 2004).

To conclude, a stretch of wood as wide as required (depending on the results of the work needs to be done in the designing part of such project), located appropriately (again, after a thorough design stage) below the Ein-El-Assad Formation escarpment is the recommended mitigation solution for rockfall hazard for Qiryat-Shemona and its vicinity. The above mentioned ROCKFOR final report (Berger, 2004) contains a complete set of rules and tools required for such a project, including guidance for sustaining a forest for long periods. ❖

## Chapter 5

### Conclusion

**T**he purpose of this study is to evaluate rockfall hazard for the town of Qiryat-Shemona, which is situated on an active segment of the Dead Sea Transform fault. Hazard evaluation is based on modeling rockfall trajectories using the analysis provided by the *Colorado Rockfall Simulation Program v4*. Evaluation of rockfall hazard aims to locate areas subject to impact and provide relevant data to enable the design of mitigation measures to protect the town's people and property. A possible correlation to earthquakes as a triggering mechanism of rockfalls is analyzed using OSL dating of soil samples from beneath large fallen blocks, thus deducing the time of rockfalls.

Eight OSL ages of rockfalls for the past 3 ka cluster around dates of historical earthquakes. Earlier rockfalls were triggered by a prehistoric event at 6 ka and by a strong earthquake around 52 ka. It is concluded that earthquakes of large magnitudes ( $M_w \geq 7$ ) are the triggering mechanism of rockfalls. The mean rockfall recurrence time of 850 years is in accordance with DST earthquake recurrence interval for such magnitudes ( $>800$  and  $<3,000$  years). However, the fact that large destructive earthquakes at 1759 AD, 1857 AD that occurred in the vicinity did not trigger rockfall (none dated in this study) and despite of expected topographic amplification, suggests that not all large earthquakes trigger rockfalls. Apparently the rock-mass has to be weakened by joints and fractures to facilitate rockfalls. A larger dataset of OSL ages is required for a reliable temporal association of rockfalls and earthquakes.

Field block size distribution was found to fit worldwide rockfall size inventory catalogs, i.e. reflecting a complete rockfall block size distribution. It was used to calculate the probability of an impact by a block of given size ( $R^2=0.97$ ).

Using the rockfall simulation program and calibrating it to the studied area, rockfall hazard maps are compiled and analyzed. Results show that specific regions at the south-western part of town are subjected to rockfall hazard analysis of block velocity and kinetic energy indicates that town premises are in danger of rockfall impact, with block velocities of 10–15 m/s and kinetic energy of 18,000–45,000 kJ (98% confidence) for block volume of 125 m<sup>3</sup>.

Rockfall recurrence is used to calculate the probability for rockfall occurrence for a given time period. Rockfall hazard for Qiryat-Shemona for a given time and given block size (or smaller) is defined as the product of this and the probability of occurrence of a certain block size. OSL age analysis (850 years recurrence time and the last rockfall triggered by the 1202 AD earthquake) lead to a 6.5% probability for the next rockfall to occur within the next 50 years, and a 57%



probability within the next 475 years. Evaluated rockfall hazard probability for 50 years ( $H_{R50}$ ) is 0.044–0.065, and for 475 years ( $H_{R475}$ ) 0.385–0.575, for block sizes of 10–125 m<sup>3</sup> respectively.

In light of the evaluated hazard, mitigation design should be based on the location of rockfall susceptible points of interest. The estimated velocities and kinetic energies should be used as parameters in the design of mitigation measures. It seems that an efficient and environmentally friendly mitigation design is forestation of the slope.

Two aspects need to be further studied: a. augmentation of the set of rockfall ages; b. design of proper forestation for rockfall hazard mitigation. ✖

## References

---

- Agliardi, F. and Crosta, G.B., 2003. High resolution three-dimensional numerical modelling of rockfalls. *International Journal of Rock Mechanics and Mining Sciences*, 40(4): 455-471.
- Aitken, M.J., 1998. *An Introduction to Optical Dating*. Oxford University Press, Oxford.
- Amiran, D.H.K., Ariei, E. and Turcotte, T., 1994. Earthquakes in Israel and Adjacent Areas - Macroseismic Observations since 100 Bce. *Israel Exploration Journal*, 44(3-4): 260-305.
- Azzoni, A., La Barbera, G. and Zaninetti, A., 1995. Analysis and Prediction of Rockfalls Using a Mathematical Model. *International Journal of Rock Mechanics and Mining Sciences and Geomechanics Abstracts*, 32: 709-724.
- Bar-Matthews, M. and Ayalon, A., 2004. Speleothems as paleoclimate indicators, a case study from Soreq cave located in the Eastern Mediterranean region, Israel. In: R.W. Battarbee, F. Gasse and C.E. Stickley (Editors), *Past Climate variability through Europe and Africa*. Kluwer Academic Publishers, Dordrecht, The Netherlands, pp. 363-391.
- Bartov, Y., Goldstein, S.L., Stein, M. and Enzel, Y., 2003. Catastrophic arid episodes in the Eastern Mediterranean linked with the North Atlantic Heinrich events. *Geology*, 31(5): 439-442.
- Becker, A. and Davenport, C.A., 2003. Rockfalls triggered by the AD 1356 Basle Earthquake. *Terra Nova*, 15: 258-264.
- Begin, Z.B., 2005. Destructive earthquakes in the Jordan Valley and the Dead Sea — their reoccurrence interval and the probability of their occurrence, *Geol. Surv. Israel*, Report GSI/12/2005.
- Begin, Z.B., Steinberg, D.M., Ichinose, G.A. and Marco, S., 2005. A 40,000 year unchanging seismic regime in the Dead Sea rift. *Geology*, 33(4): 257-260.
- Berger, F., 2004. Forest interrelation efficiency of the protective function of mountain forest against rockfalls, final report, Cemagref, Grenoble.
- Boyle, R., 1664. Observations made this 27th of October, 1663, about Mr. Clayton's Diamond. In: R. Boyle (Editor), *Experiments and Considerations Touching Colours*. Henry Herringman, London, pp. 413-423.
- Bozzolo, D. and Pamini, R., 1986. Simulation of rock falls down a valley side. *Acta Mechanica*, 63(1): 113-130.
- Celebi, M., 1987. Topographical and geological amplifications determined from strong - motion and aftershock records of the 3 March 1985 Chile earthquake. *Bulletin of the Seismological Society of America*, 77(4): 1147-1167.
- Chang, W.R., 1998. The effect of surface roughness on dynamic friction between neolite and quarry tile. *Safety Science*, 29: 89-105.
- Crosta, G.B. and Agliardi, F., 2004. Parametric evaluation of 3D dispersion of rockfall trajectories. *Natural Hazards and Earth System Sciences*, 4: 583-598.

- Dorren, L.K.A., 2003. A review of rockfall mechanics and modelling approaches. *Progress in Physical Geography*, 27: 69-87.
- Dussauge-Peisser, C. et al., 2002. Probabilistic approach to rock fall hazard assessment: potential of historical data analysis. *Nat. Hazards Earth Syst. Sci.*, 2: 15-26.
- Dussauge, C., Grasso, J.R. and Helmstetter, A.S., 2003. Statistical analysis of rockfall volume distributions: Implications for rockfall dynamics. *Journal of Geophysical Research-Solid Earth*, 108(B6).
- Erismann, T., 1986. Flowing, rolling, bouncing, sliding: Synopsis of basic mechanisms. *Acta Mechanica*, 64(1): 101-110.
- Erismann, T.H. and Abele, G., 2001. *Dynamics of Rockslides and Rockfalls*. Springer, 316 pp.
- Evans, S.G. and Hungr, O., 1993. The assessment of rockfall hazard at the base of talus slopes. *Canadian Geotechnical Journal*, 30(4): 620-636.
- Freund, R. et al., 1970. Shear Along Dead-Sea Rift. *Philosophical Transactions of the Royal Society of London Series a-Mathematical and Physical Sciences*, 267(1181): 107-&.
- Garfunkel, Z., 1981. Internal structure of the dead-sea leaky transform (rift) in relation to plate kinematics. *Tectonophysics*, 80(1-4): 81-108.
- Gesner, C., 1555. *e raris et admirandis herbis quae sive quod noctu luceant, sive alias ob causas, Lunariae nominantur et obiter de alias etiam rebus, quae in tenebris lucent*, *Commentariolus* (A short commentary on rare and marvellous plants that are called lunar either because they shine at night or for other reasons, and also on other things that shine in darkness), Tiguri, Zürich.
- Giani, G.P., Giacomini, A., Migliazza, M. and Segalini, A., 2004. Experimental and Theoretical Studies to Improve Rock Fall Analysis and Protection Work Design. *Rock Mechanics and Rock Engineering*, 37(5): 369-389.
- Glikson, Y.A., 1966. The lacustrine Neogene in the Kefar Gil'adi area, northern Jordan Valley. *Isr. J. Earth Sci.*, 15: 85-100.
- Griffiths, D. and Bollinger, G., 1979. The effect of Appalachian Mountain topography on seismic waves. *Bulletin of the Seismological Society of America*, 69(4): 1081.
- Guidoboni, E. and Comastri, A., 2005. Catalogue of earthquakes and tsunamis in the Mediterranean area from the 11th to the 15th century. *Istituto Nazionale di Geofisica e Vulcanologia*, Rome, 1037 pp.
- Guidoboni, E., Comastri, A. and Traina, G., 1994. Catalogues of Ancient Earthquakes in the Mediterranean Area up to the 10th Century. *Istituto Nazionale di Geofisica*, Roma, 504 pp.
- Guzzetti, F., Crosta, G., Detti, R. and Agliardi, F., 2002. STONE: a computer program for the three-dimensional simulation of rock-falls. *Computers & Geosciences*, 28(9): 1079-1093.
- Guzzetti, F., Reichenbach, P. and Ghigi, S., 2004. Rockfall Hazard and Risk Assessment Along a Transportation Corridor in the Nera Valley, Central Italy. *Environmental Management*, 34(2): 191-208.
- Guzzetti, F., Reichenbach, P. and Wieczorek, G.F., 2003. Rockfall hazard and risk assessment in the Yosemite Valley, California, USA. *Natural Hazards and Earth System Sciences*, 3: 491-503.

- Haase-Schramm, A., Goldstein, S.L. and Stein, M., 2004. U-Th dating of Lake Lisan (late Pleistocene Dead Sea) aragonite and implications for glacial East Mediterranean climate change. *Geochimica Et Cosmochimica Acta*, 68(5): 985-1005.
- Hartzell, S.H., Carver, D.L. and King, K.W., 1994. Initial investigation of site and topographic effects at Robinwood Ridge , California. *Bulletin of the Seismological Society of America*, 84(5): 1336-1349.
- Havenith, H.B., Vanini, M., Jongmans, D. and Faccioli, E., 2003. Initiation of earthquake-induced slope failure: influence of topographical and other site specific amplification effects. *Journal of Seismology*, 7(3): 397-412.
- Heim, A., 1932. *Bergsturz und Menschenleben*. Fretz und Wasmuth, Zu"rich, Switzerland, 218 pp.
- Heimann, A. and Ron, H., 1987. Young faults in the Hula Pull-Apart Basin, central Dead Sea Transform. *Tectonophysics*, 141: 117-124.
- Hoek, E. and Bray, J.W., 1981. *Rock Slope Engineering*. E & FN SPON, London, 358 pp.
- Huntley, D.J., Godfrey-Smith, D.I. and Thewalt, M.L.W., 1985. Optical dating of sediments. *Nature*, 313(5998): 105-107.
- IMS, 2007. IMS website: Climate information - long term info Israel Meteorological Service.
- Jibson, R.W., 1996. Use of landslides for paleoseismic analysis. *Engineering Geology*, 43(4): 291-323.
- Jones, C.L., Higgins, J.D. and Andrew, R.D., 2000. Colorado Rockfall Simulation Program Version 4.0 Manual. CDOT-SYMB-CGS-99-1, Colorado Department of Transportation, Denver, CO 80222.
- Kafri, U., 1989. Facies changes and karst phenomenon in the Judea Group and their implications on the groundwater regime in the eastern Galilee, Isr. Geol. Soc. Ann. Meeting, Ramot, Field trip Guidebook, pp. 38-46.
- Kafri, U., 1991. Lithostratigraphy of Judea Group in eastern Galilee, emphasizing the Naftali mountains. GSI/24/91, Geological Survey of Israel, Jerusalem.
- Kagan, E., Stein, M., Bar-Matthews, M. and Agnon, A., 2007. A Tale of Two Cataclysmic Earthquakes: 39 and 52 kyr BP, Dead Sea Transform, Israel; a Multi-archive Study, *Eos Trans. AGU*, 88(52), Fall Meet. Suppl., Abstract T41E-04.
- Kagan, E.J., Agnon, A., Bar-Matthews, M. and Ayalon, A., 2005. Dating large infrequent earthquakes by damaged cave deposits. *Geology*, 33(4): 261-264.
- Katz, O. and Aharonov, E., 2006. Landslides in vibrating sand box: What controls types of slope failure and frequency magnitude relations? *Earth and Planetary Science Letters*, 247(3-4): 280-294.
- Keefer, D.K., 1984. Landslides caused by earthquakes. *Geol Soc Am Bull*, 95(4): 406-421.
- Keefer, D.K., 2002. Investigating Landslides Caused by Earthquakes – A Historical Review. *Surveys in Geophysics*, 23(6): 473-510.
- Keylock, C. and Domaas, U., 1999. Evaluation of topographic models of rockfall travel distance for use in hazard applications. *Arctic Antarctic and Alpine Research*, 31(3): 312-320.

- Kirkby, M.J. and Statham, I., 1975. Surface Stone Movement and Scree Formation. *Journal of Geology*, 83(3): 349-362.
- Kobayashi, Y., Harp, E.L. and Kagawa, T., 1990. Simulation of rockfalls triggered by earthquakes. *Rock Mechanics and Rock Engineering*, 23(1): 1-20.
- Lian, O.B. and Huntley, D.J., 2001. Luminescence dating. In: W.M. Last and J.P. Smol (Editors), *Tracking Environmental Change Using Lake Sediments: Basin Analysis, Coring, and Chronological Techniques*. Kluwer Academic Publishing, Dordrecht, pp. 261-282.
- Lian, O.B. and Roberts, R.G., 2006. Dating the Quaternary : progress in luminescence dating of sediments. *Quaternary Science Reviews*, 25(19-20): 2449-2468.
- Lied, K., 1977. Rockfall problems in Norway. ISMES Publication no. 90: 51-53.
- Malamud, B.D., Turcotte, D.L., Guzzetti, F. and Reichenbach, P., 2004. Landslide inventories and their statistical properties. *Earth Surface Processes and Landforms*, 29(6): 687-711.
- Marco, S., 1996. Paleomagnetism and paleoseismology in the late Pleistocene, Dead Sea graben. Ph.D. Thesis, Hebrew University of Jerusalem.
- Marco, S. et al., 1997. 817-year-old walls offset sinistrally 2.1 m by the Dead Sea Transform, Israel. *Journal of Geodynamics*, 24: 11-20.
- Marco, S., Stein, M., Agnon, A. and Ron, H., 1996. Long-term earthquake clustering: A 50,000-year paleoseismic record in the Dead Sea Graben. *Journal of Geophysical Research-Solid Earth*, 101(B3): 6179-6191.
- Matsuoka, N. and Sakai, H., 1999. Rockfall activity from an alpine cliff during thawing periods. *Geomorphology*, 28: 309-328.
- Migowski, C., Agnon, A., Bookman, R., Negendank, J.F.W. and Stein, M., 2004. Recurrence pattern of Holocene earthquakes along the Dead Sea transform revealed by varve-counting and radiocarbon dating of lacustrine sediments. *Earth and Planetary Science Letters*, 222(1): 301-314.
- Pfeiffer, T.J. and Bowen, T., 1989. Computer simulation of rockfalls. *Bulletin of the Association of Engineering Geologists*, 26: 135-146.
- Picard, L., 1952. The geology of Kefar-Giladi. *Bull. Israel Explor. Soc.*, "Lif" memorial(vol. B): 73-77.
- Ritchie, A.M., 1963. The evaluation of rock fall and its control. *Highway Research Record*(17): 13-28.
- Ron, H., Shamir, G. and Eyal, M., 1997. Deformation of Margalioth block between Roum and Margalioth faults, Isr. Geol. Soc. Ann. Meeting, Kefar Gil'adi, Field trip Guidebook, pp. 33-45.
- RTM, 1997. Inventaire des mouvements rocheux, Secteur de Grenoble. 38, Service de Restauration des terrains en Montagne Grenoble, France.
- Salamon, A., Hofstetter, A., Garfunkel, Z. and Ron, H., 2003. Seismotectonics of the Sinai subplate - the eastern Mediterranean region. *Geophysical Journal International*, 155(1): 149-173.
- Scholz, C.H., 2002. *The Mechanics of Earthquakes and Faulting*. Cambridge Univ. Press, New York, 471 pp.

- Shapira, A., 2002. An updated map of peak ground accelerations for Israeli Standard 413. In: [http://www.gii.co.il/heb/Teken/report\\_413.htm](http://www.gii.co.il/heb/Teken/report_413.htm) (Editor).
- Shtober-Zisu, N., 2006. Quaternary tectonic geomorphology along the Naftali Mountain front. PhD Thesis, Tel Aviv University, Tel Aviv.
- Sneh, A. and Weinberger, R., 2002. The Geology of Qiryat Shemona. GSI-36-2002, Geological Survey of Israel, Jerusalem.
- Sneh, A. and Weinberger, R., 2003. Geology of the Metulla quadrangle 1:50,000: Implications for the stratigraphic division and the fault system around the Hula Valley. GSI/7/2003, Geological Survey of Israel, Jerusalem.
- Varnes, D.J., 1978. Slope movement types and processes. In: R.L. Schuster and R.J. Krizek (Editors), Landslides, analysis and control. Transportation Research Board, National Research Council, Washington, D.C., pp. 11-33.
- Vidrih, R., Ribicic, M. and Suhadolc, P., 2001. Seismogeological effects on rocks during the 12 April 1998 upper Soca Territory earthquake (NW Slovenia). Tectonophysics, 330: 153-175.
- Wechsler, N., Marco, S. and Katz, O., 2006. Estimating historical earthquakes parameters using archeology and geology in Um-el-Kanatir, Dead Sea Transform. SSA annual meeting, Seismological Research Letters, 77(2): 247.
- Weinberger, R. and Sneh, A., 2004. The geology of Qiryat Shemona region, field trips guide, Israel Geological Society annual meeting, Hagoshrim.
- Wieczorek, G., Morrissey, M., Iovine, G. and Godt, J., 1998. Rock fall Hazards in the Yosemite Valley, US Geological Survey Open File Report.
- Wieczorek, G.F. and Jäger, S., 1996. Triggering mechanisms and depositional rates of postglacial slope-movement processes in the Yosemite Valley, California. Geomorphology, 15: 17-31.
- Wieczorek, G.F., Nishenko, S.P. and Varnes, D.J., 1995. Analysis of rock falls in the Yosemite Valley, California. In: J.J. Daemen and R.A. Schultz (Editors), Rock Mechanics Symposium, 35th, Reno: Nevada, University of Nevada. Balkema, Rotterdam, pp. 85-89.
- Yagoda, G., Katz, O., Amit, R. and Hatzor, Y.H., 2007. Estimation of PGA values from back analysis of a large landslide in the eastrens margins of the Kineret, Israel Geological Society Annual Meeting, Dead Sea.
- Zaslavsky, Y., 2008. Strong ground motion topographic amplification in the Manara station, Personal discussion.
- Zaslavsky, Y. and Shapira, A., 2000. Observation of topographic site effects in Israel. Israel Journal of Earth Sciences, 49: 111.
- Zaslavsky, Y., Shapira, A. and Arzi, A.A., 2000. Amplification effects from earthquakes and ambient noise in the Dead Sea rift (Israel). Soil Dynamics and Earthquake Engineering, 20(1-4): 187-207.



## Appendix A

# Engineering Appendix

## A.1 Block Properties

Simulated diameters were calculated from representative volume scales rounded to 1 decimal digit. Rock density is 2,500 kg/m<sup>3</sup> (Ein-El-Assad Formation limestone).

TABLE A-1 Simulation Block Properties			
Simulated Diameter (m)	Volume Scale (m <sup>3</sup> )*	Exact Volume (m <sup>3</sup> )**	Weight (kg)**
1.3	1	1.2	2,875
2.7	10	10.3	25,750
4.6	50	51.0	127,400
5.8	100	102.2	255,400
6.2	125	124.8	312,000

\* Representative block volume scales

\*\* Reported by CRSP v4 (calculated from simulated diameter).

## A.2 Block Travel Distances

### A.2.1 Characteristics of Block Stop Locations

See *section 4.2.1 - Characteristics of Block Stop Locations* for detail.

TABLE A-2 Rockfall Block Stop Location Characterization		
Approach	Stop Slope Angle (deg.)	Stop Swath Distance (m)
Statistic*	5° – 10°	14 m – 62 m
Conservative**	3°	105 m

\* Mean 7.7° stop angle with SD=2.3° and mean 38 m stop swath distance with SD=24 m.

\*\* Lowest stop angle and longest stop swath.



## A.3 Maps of Predicted Hazard from Future Rockfalls

### A.3.1 Rockfall Hazard Area Map

This map (*section 3.2.4*) details the area found as subject to future rockfall hazard. It may be used for these aims:

- Locate existing specific points or areas of interest which are presently under rockfall hazard and may require mitigation actions.
- Check whether rockfall hazard exists for future planned areas of interest (west of the current built area).
- Locate safe locations for any sort of future planning (e.g. buildings, parks, roads and infrastructure).

### A.3.2 Town Border Impact Hazard Map

This map (*section 3.3.2*) details the exact locations where future rockfalls are predicted to impact town premises. Simulated impact locations at town border are marked, referring to the analysis of predicted block velocity and kinetic energy at that point (*section A.4*). This map may be used to:

- Identify exact locations subject to rockfall.
- Refer to velocity and kinetic energy analysis for mitigation design.

### A.3.3 Frequency of Stopping Blocks and Analysis Location Map

This map (*section 3.2.4.2*) details the locations where specific cumulative frequencies of simulated blocks stop (50%, 68%, 95% and 100% of simulated blocks) and includes reference points to exact locations where the velocity and kinetic energy analysis for the entire study area (including west to Route 90) were performed.

This map may be used to:

- Refer to velocity and kinetic energy analysis for mitigation design.
- Refer to velocity and kinetic energy analysis for future planning.
- Locate areas subject to higher probable hazard (where cumulative probability of stopped blocks is lower – predicted hazard is higher since a larger number of blocks are still in motion in that location).

## A.4 Velocity and Kinetic Energy Analysis

### A.4.1 Velocity and Kinetic Energy at Town Border Impact Locations

Following are the calculated velocity and kinetic energy of a  $D=6.2$  m ( $V=125$  m<sup>3</sup>) block at impact point with the western town border. Cumulative probability for this block size or smaller is 100%. Referred profile numbers (locations of analysis points) are marked by orange-hazard triangles on the *Town Border Impact Hazard Map (section 3.3.2)*.

TABLE A-3 Velocity and Kinetic Energy at Town Border Impact Locations				
Profile	East ITM (X)	North ITM (Y)	Velocity (m/s)	Kin. Energy (kJ)
8	253137	788708	11.9	30,441
9	253137	788663	14.8	24,821
10	252851	788951	9.7	29,576
11	252833	789006	13.9	40,172
12	252827	789090	11.9	17,944
13	252831	789119	12.2	44,479
14	252854	789184	11.1	28,762

\* Mean velocity 12.2 m/s (SD=1.7 m/s); mean kinetic energy 30,885 kJ (SD=8,960 kJ)

### A.4.2 Velocity and Kinetic Energy at Block Stop Locations

Calculated velocity and kinetic energy of a  $D=6.2$  m ( $V=125$  m<sup>3</sup>) block at stop location (95% of total travel distance). Cumulative probability for this block size or smaller is 100%. Analysis point locations are marked by orange triangles on the *Block Travel Distance Hazard Map (section 3.2.4.2)*.

TABLE A-4 Velocity and Kinetic Energy at Stop Location				
Profile	East I <sub>TM</sub> (X)	North I <sub>TM</sub> (Y)	Velocity (m/s)	Kin. Energy (kJ)
5	252759	789462	5.6	6,632
6	253063	788794	8.9	12,737
7	252928	788865	4.5	4,334
8 †	253201	788705	10.4	17,407
9 †	253196	788662	11.5	21,690
10 †	252893	788947	8.4	11,188
11 †	252933	789004	7.4	10,893
12 †	252933	789084	7.5	11,336
13 †	252935	789117	7.7	11,779
14 †	252887	789183	6.9	9,623
15	252846	789266	6.3	6,576
16 †	252880	789224	6.7	7,445
17	252784	789361	6.7	9,180
18	252781	789423	7	8,086
19	252706	789599	7.3	8,740
20	252764	789719	4.6	4,479
21	252752	789815	6.2	6,541
22	252599	790074	5.1	4,423
24	253138	788424	8.6	11,972
25	252762	787997	6.7	7,598
26	253085	787451	6.2	6,492
27	253026	787273	6.8	7,619
28	253044	787104	5.7	5,400
29	253176	786601	4.9	4,196
30	252716	789505	5.7	5,464

\* Mean velocity 6.9 m/s (SD=1.7 m/s); mean kinetic energy 8,873 kJ (SD=4,177 kJ)

† Rockfall impact hazard to town premises

## A.5 Rockfall Hazard Evaluation for Qiryat-Shemona

### A.5.1 Rockfall Recurrence Time Probability

Recurrence time probability  $P_R$  is based on OSL ages analysis of one rockfall event every 850 years. Conditional probability is used to account for 800 years of rockfall quiescence. Calculation per given period  $\Delta t$  is detailed in *section 4.3.6*.

TABLE A-5 **Rockfall Recurrence Probability**

Time Period $\Delta t$	Rockfall Probability $PR(\Delta t)$
50 years	0.065 (6.5%)
100 years	0.130 (13%)
475 years	0.575 (57%)

### A.5.2 Rockfall Block Size Probability

The probability for a block of given diameter  $D$  or smaller is

$$p = 0.412 \ln(D) + 0.262$$

This may also be used to determine the maximal block diameter which may be encountered considering a given probability  $p$

$$D = \exp[(p - 0.262) / 0.412]$$

This correlation should be used when considering probable rockfall hazard. Since larger blocks pose larger hazard due to higher kinetic energy which increases potential damage, the probabilities for different block sizes may be required when planning rockfall mitigation solutions. Selected diameter values calculated per cumulative probabilities from the  $D(p)$  correlation above are presented in **Table A-6**.

Block size probabilities calculated according to the  $p(D)$  fit-curve correspond to blocks of given sizes or smaller ( $P_D$ ) and probabilities for larger blocks than that given size ( $1-P_D$ ).

TABLE A-6 **Cumulative Probabilities of Selected Block Diameters\***

Block Diameter (m)**	Volume (m <sup>3</sup> )	$P_D$ ***	$1-P_D$ ***
2.7	10	0.671	0.329
4.6	50	0.891	0.109
5.8	100	0.986	0.014
$\geq 6.0$	113	1.000	0.000

\* Probability derived from fit-curve for block diameter cumulative probability  $p(D)$

\*\* Probability for  $D=1.3$  m ( $V=1$  m<sup>3</sup>) is not available (no data collected for blocks  $<1$  m<sup>3</sup>)

\*\*\*  $P_D$  is probability for given block size or smaller;  $1-P_D$  is probability for larger than given size blocks

### A.5.3 Rockfall Hazard Evaluation for Given Time Period and Block Size

Rockfall hazard  $H_R$  is calculated by multiplying the recurrence time probability  $P_R$  for given period  $\Delta t$  (years) by the required cumulative probability  $P_D$  for given block diameter  $D$  (m)

$$H_R(\Delta t, D) = P_R(\Delta t) * P_D(D)$$

TABLE A-7 Rockfall Hazard Evaluation for 50 and 475 Years		
Block Diameter (Volume)	H <sub>R50</sub> Probability*	H <sub>R475</sub> Probability*
2.7 m (10 m <sup>3</sup> )	0.044 (4.4%)	0.38 (38%)
4.6 m (50 m <sup>3</sup> )	0.058 (5.8%)	0.51 (51%)
5.8 m (100 m <sup>3</sup> )	0.064 (6.4%)	0.56 (57%)
6.0 m (113 m <sup>3</sup> )	0.065 (6.5%)	0.57 (57%)
6.2 m (125 m <sup>3</sup> )	0.065 (6.5%)	0.57 (57%)

\* Probability for impact by given block size or smaller; calculated for 850 yr rockfall recurrence time conditional probability for an 800 year rockfall-quiescence period (since 1202 AD earthquake) derived from OSL ages.

## A.6 Rockfall Impact Mitigation Design

### A.6.1 Possible Design for Mitigation of Rockfall Damage

Reducing rock-fall hazard by engineering the slopes to suggested stop angles and swath distance may be efficient, but also pretty expensive and very harmful for the local environment (the study area is also part of a national park). It is recommended that mitigation design would base on forestation of the slope between the Ein-El-Assad Formation escarpment cliff and Qiryat-Shemona. A comprehensive reference for rockfall mitigation using forestation is the final report of the *ROCKFOR European Project* (Berger, 2004). The project website, where that report is also available on-line, can be found here: [rockfor.grenoble.cemagref.fr/texte/results.html](http://rockfor.grenoble.cemagref.fr/texte/results.html) ❖

## Appendix B

### Block Catalog

Details of the 76 blocks ( $V > 1 \text{ m}^3$ ) documented in the mapping area:

TABLE B-1 Block Catalog				
Block ID	Volume (m <sup>3</sup> )	East ITM (X)	North ITM (Y)	Photo #
001	17.5	252605	789538	4166 R
002	56.3	252603	789548	4166 L
003	35.0	252610	789544	4167
004	56.3	252548	789527	4171
005	120.0	252574	789518	4172
006	47.3	252557	789501	4175
007	80.0	252571	789492	4176
008	25.0	252551	789500	4178
009	9.0	252551	789505	4179
010	16.9	252533	789503	4183
011	22.5	252626	789504	4184
012	17.0	252607	789506	4186
013	10.5	252588	789478	4188 L
014	4.3	252581	789469	4188 R
015	18.0	252603	789478	4190
016	41.3	252611	789373	4193
017	36.0	252695	789425	4206
018	5.7	252537	789523	4208
019	6.2	252537	789517	4210 L
020	15.0	252548	789534	4211
021	18.8	252529	789542	4216
036	13.2	252682	789425	10384
037	3.7	252696	789446	10385
038	9.4	252687	789492	10386
039	18.5	252738	789492	10387

TABLE B-1 <b>Block Catalog</b>				
<b>Block ID</b>	<b>Volume (m<sup>3</sup>)</b>	<b>East ITM (X)</b>	<b>North ITM (Y)</b>	<b>Photo #</b>
040	3.8	252750	789524	10389
041	6.7	252690	789572	10390
042	3.9	252699	789441	10393
043	6.3	252770	789405	10394
046	1.1	252764	789322	10397
048	3.6	252755	789346	10399
049	3.5	252753	789341	10400
051	2.0	252751	789291	10410
052	1.4	252749	789288	10411
054	1.4	252736	789309	10413
055	2.8	252734	789300	10414
056	1.9	252730	789309	10415
058	2.4	252700	789317	10417
059	11.6	252687	789301	10418
060	4.0	252711	789300	10419
061	1.8	252713	789273	10425
062	29.9	252554	789509	10427
063	32.4	252542	789467	10428
064	7.8	252531	789460	10430
065	1.8	252537	789455	10431
066	2.0	252536	789449	10432
067	4.6	252554	789466	10434
069	1.3	252560	789486	10435
070	2.2	252562	789483	10436
071	3.9	252562	789473	10437
074	7.4	252565	789426	10441 R



TABLE B-1 <b>Block Catalog</b>				
<b>Block ID</b>	<b>Volume (m<sup>3</sup>)</b>	<b>East ITM (X)</b>	<b>North ITM (Y)</b>	<b>Photo #</b>
075	1.1	252563	789436	10441 L
076	1.7	252572	789427	10442
077	6.3	252584	789414	10443
080	1.3	252621	789479	10448
081	3.2	252587	789441	10449
083	2.6	252577	789364	10451
084	2.9	252597	789343	10452
085	2.5	252652	789323	10453
086	1.5	252672	789311	10454
088	3.6	252584	789332	10460
092	8.6	252580	789353	10464
093	1.1	252586	789391	10465
095	31.0	252511	789336	10467
096	1.8	252516	789389	10468
098	1.4	252542	789538	10470
115	9.8	252372	789430	10487
118	4.7	252389	789466	10490
119	8.0	252402	789472	10494
120	3.5	252425	789433	10495
122	1.1	252418	789436	10497
123	1.4	252427	789515	10499 L
141	125.0	252761	789571	16286
142	35.4	252649	789600	16290
143	17.6	252668	789561	16292
144	2.0	253085	789025	16295



מוצע בזאת כי רעידות אדמה ממגניטודה גבוהה ( $M_w \geq 7$ ) הן המנגנון המעורר (triggering mechanism) של נפילות הסלעים. שילובן של מפות שבהן ניתוח מרחקי התנועה המקסימליים של בלוקים עם ניתוח מורפולוגי של המדרון, מניבים מסלולי תנועה אפשריים של נפילות סלעים שהתרחשו בעבר, לאורכם מכוילים הפרמטרים השונים של תוכנת ההדמיה. פרמטרים אלו משמשים לעריכת הדמיות של מסלולי תנועה אפשריים של בלוקים לכיוון שטח העיר (איור 3-11). תוצאות ההדמיות הללו משמשות להפקתן של מפות הסיכון לנפילת סלעים. תוצאות הניתוח מלמדות כי בחלקה הדרום-מערבי של העיר נתונים חיי-אדם ומתקנים בסיכון באזורים מסוימים המפורטים במפה (איור 3-25). זמן החזרה הממוצע של נפילות סלעים וההסתברות לפגיעה מבלוקים בגדלים שונים (המחושבת מהתפלגות הגדלים) מניבים את הערכת הסיכון לנפילת סלעים לאזור קריית-שמונה. ניתוח גילי OSL של ארועי נפילת סלעים (זמן חזרה ממוצע של 850 שנה וייחוס נפילת הסלעים האחרונה לפי ממצאי עבודה זו לרעידת האדמה של 1202 לספירה) מניבים הסתברות של 6.5% להתרחשות נפילת סלעים ב-50 השנים הקרובות, ושל 57% להתרחשות נפילת סלעים ב-475 השנים הקרובות. הערכת הסתברות הסיכון לנפילת סלעים ב-50 השנים הקרובות היא 0.044–0.065 וב-475 השנים הקרובות ההסתברות היא 0.385–0.575 עבור גדלי בלוק נתונים (או קטנים יותר) של 10–125 מטרים מעוקבים בהתאמה. תוצאות ההדמיה בנקודות פגיעה מסוימות, שסומנו בגבול המדרון עם שטח העיר, מניבות מהירויות בלוקים של 10–15 מ'שנייה ואנרגיה קינטית של 18,000–45,000 קילוג'אול (ברמת בטחון של 98%) עבור בלוקים בנפח 125 מטרים מעוקבים.

אמצעי מיגון ידידותי לסביבה, המומלץ לעצירת הגלגול במדרון בזמן נפילת סלעים מהמצוק, הוא ייעור המדרון. היער יספק הגנה לתושבי קריית-שמונה תוך שמירה על הסביבה הטבעית. ❖

מטרתה של עבודה זו היא הערכה של הסיכון לנפילת סלעים לעבר העיר קריית-שמונה. העיר ממוקמת על אחד מסעיפיו הפעילים טקטוני של טרנספורם ים-המלח, למרגלות רכס הרי נפתלי המתנשא ממערב לה לגובה של כ-800 מטרים מעל העיר (איור 2-1). במתלול רמים, כ-400 מטרים מעל העיר, חשופה תצורת עין-אל-אסד שהרכבה גיר ועוביה כ-40 מטר היוצרת מצוק המשכי ובולט. תצורה זו היא המקור של גושי-הסלע הנעים במדרון (נפילת סלעים). בתצלומי אוויר מ-1946 ומ-1951 נראים מאות בלוקים בגדלים של 0.1–150.0 מטרים מעוקבים פזורים למרגלות המצוק, גם באזורים שכיום נמצאים בשטחה הבנוי של העיר (איור 10-1). מודגש בזאת כי עבודה זו אינה כוללת פתרון מקיף להערכת סיכונים טבעיים לקריית-שמונה, אלא עוסקת בסיכונים הנשקפים לעיר ותושביה מנפילת סלעים, ובהקשר האפשרי לרעידות אדמה.

לצורך הערכת הסיכון לנפילת סלעים לעבר קריית-שמונה, נבחנו בעבודה זו השאלות הבאות: א. מה מקור הסלעים ומהו המנגנון המעורר את נפילת הסלעים? ב. מהם מסלולי התנועה של הבלוקים במורד המדרון ומה גבול השטח המצוי בסיכון? ג. מהו הסיכון הנשקף לעיר ולתושביה מנפילת סלעים, ואילו אמצעי-מיגון אפשריים ניתן ליישם כמענה לסיכון?

בכדי לענות על השאלות לעיל, נערך מיפוי של מאות בלוקים במדרון שמעל לעיר (בשדה ובעזרת תצלומי אוויר מ-1946 ומ-1951) ונעשה ניתוח של תפרושת הבלוקים המרחבית ושל התפלגות הגדלים שלהם (איור 5-3); הגילים של ארועי נפילת הסלעים נקבעים על ידי תיארוך בשיטת OSL של דגימות קרקע, שנאספות מתחת לבלוקים גדולים אשר נפלו מן המצוק; נערכות הדמיות של מסלולי תנועת הבלוקים במורד המדרון באמצעות תוכנה מסחרית (CRSP v4); מפות שמתארות את הערכת הסיכון לנפילת סלעים לקריית-שמונה מופקות מתוצאות ההדמיות ומאותרים בהן האזורים הנתונים בסכנה (איור 21-3); ניתוח ההדמיות כולל אומדן מהירות הבלוקים והאנרגיה הקינטית שלהם במקומות הפגיעה הצפויים בגבול העיר (טבלה 13-3 ואיור 25-3), נתונים המשמשים לתכנון אמצעי-מיגון שתפקידם לשמור על שלומם של תושבי העיר ומתקניה (נספח A). הערכת הסיכון נגזרת משני גורמים: א. זמן החזרה המשוער של נפילות סלעים (מחושב מתוצאות גילי OSL); ב. ההסתברות לפגיעה על ידי גודל בלוק מסוים (מניתוח סטטיסטי של התפלגות גדלי הבלוקים).

התוצאות מראות כי התפלגות גדלי הבלוקים של נפילת הסלעים מתאימה לכלל-חזקה מהצורה  $ax^b$ , כאשר ערכו של מעריך החזקה  $b$  הוא 1.17– (איור 5-3), בהתאמה להתפלגויות גדלי בלוקים של נפילת סלעים שנמצאו במחקרים אחרים ברחבי העולם. שמונה גילי OSL של דגימות קרקע מתקבצים סביב תאריכים ידועים של רעידות אדמה המופיעות בקטלוגים היסטוריים וסיסמיים (איור 7-4).



משרד התשתיות הלאומיות  
המכון הגיאולוגי

## **הערכת הסיכון לנפילת סלעים לעבר קריית-שמונה והקשר האפשרי לרעידות אדמה**

**מור כנרי**

עבודה זו הוגשה כחיבור לקבלת תואר 'מוסמך אוניברסיטה' בחוג לגיאופיזיקה ומדעים פלנטריים,  
אוניברסיטת תל אביב

העבודה נעשתה בהדרכתם של:

ד"ר שמוליק מרקו, החוג לגיאופיזיקה ומדעים פלנטריים, אוניברסיטת תל אביב

ד"ר עודד כץ, המכון הגיאולוגי, ירושלים

ד"ר רמי ויינברגר, המכון הגיאולוגי, ירושלים